Thèse n° 7425

Monitoring of Cardiovascular and Neurological Diseases Using Wearable Devices

Présentée le 18 décembre 2020

à la Faculté des sciences et techniques de l’ingénieur
Laboratoire des systèmes embarqués
Programme doctoral en génie électrique

pour l’obtention du grade de Docteur ès Sciences

par

Dionisije ŠOPIĆ

Acceptée sur proposition du jury

Prof. S. Carrara, président du jury
Prof. D. Atienza Alonso, directeur de thèse
Prof. P. Laguna, rapporteur
Prof. Ph. Ryvlin, rapporteur
Prof. J.-M. Vesin, rapporteur

École
polytechnique
fédérale
de Lausanne

2020

Per aspera ad astra

To my family…

Acknowledgements

I will be eternally indebted to Prof. David Atienza for providing me with the wonderful opportunity to embark on my PhD journey and allowing me to be a part of his lab. It has been an honor and an absolute privilege working under his supervision and learning from him. Apart from trying to get the best out of his students, Prof. Atienza has great empathy for his students which is paramount to building a positive working environment and making people feel at ease.

I wish to express my most sincere gratitude and appreciation to Prof. Sandro Carrara, Prof. Pablo Laguna, Prof. Jean-Marc Vesin, and Prof. Philippe Ryvlin for being my jury members as well as for their insightful feedback.

A special note of thanks to Dr. Amir Aminifar for his guidance, encouragement, patience, and constructive feedback over the entire course of my doctoral dissertation. Without his valuable input, assistance and expertise, this thesis would not have been completed.

Asimismo, me gustaría agradecer especialmente al Dr. Tomás Teijeiro por su inmensa ayuda, consideración, apoyo y sobre todo por el tiempo que me ha dedicado durante mi doctorado. Trabajar con él ha sido muy enriquecedor tanto en mi vida profesional como en la personal.

Since friends are the family we choose for ourselves, I would also like to thank my friends who have made my life happier during my doctoral studies.

Prima di tutto, mi sento in dovere di ringraziare la mia anima gemella Giulia Simoni per essere stata una parte importante della mia vita durante il mio dottorato. Ringrazio anche il destino per averla messa nel mio treno della vita, perché lei è una persona di quelle che si incontrano quando la vita decide di farci un regalo.

Ensuite, je tiens à adresser particulièrement mes remerciements à Yasmina Garchi pour son amitié, sa belle énergie et son inconditionnel soutien. Je la remercie pour m'avoir fait voir la lumière au bout du tunnel quand j'étais plongé dans un profond désarroi et déchirement. Sa présence m'a permit de revenir à la surface et je lui en serai éternellement reconnaissant.

Seguidamente, me gustaría mencionar a mis compañeros hispanohablantes: Adriana Arda Valdés, Miguel Peón Quirós e Ignacio Penas Fernández por haber compartido conmigo tantos buenos momentos dentro y fuera del trabajo.

A special thanks goes to my teammate Renato Zanetti who worked with me on many different projects. I thank him for his ideas, enthusiasm, patience, commitment, knowledge as well as for his brilliant personality at work and outside of work.

I am very grateful to Arman Iranfar for making my PhD journey as well as the conference in Florence we attended together memorable and pleasant.

Un immense merci à Benoît Walter Denkinger d'avoir corrigé le résumé de ma thèse en français. Je le remercie également pour toutes les courses à pied que l'on a partagées ensemble ainsi que pour tous les beaux moments passés au travail et ailleurs.

Et comme la vie est pleine de surprises et de hasard, une des plus belles surprises sur ma route de la vie fut la connaissance de Halima Najibi. Je voudrais la remercier pour son amitié inestimable ainsi que pour le bonheur qu'elle m'a apporté depuis que nos chemins se sont croisés.

I wish to thank Lara Orlandić from the bottom of my heart for her invaluable help and support that go beyond words. From the streets of Madrid and Paris to the late nights we spent together at work, Lara became my second family leaving footprints in my heart.

As a token of my gratitude, I would like to dedicate this thesis to my family members, as they have played an important role in the development of my identity and shaping the individual that I am today. I am extremely fortunate to have been born in a family that has shown me unconditional love and untiring support. I thank them for believing in me and supporting me, even though this meant that I had to live far away from them over the last 7 years.

Velika zahvalnica mojim roditeljima Jovanki i Dragomiru, mojim sestrama Maji i Mladeni, mojoj baki Mariji, mojoj tetka Tanji i tetka Radi na bezgraničnoj ljubavi i podršci koju su mi pružili tokom školovanja. Bez moje porodice, nikad ne bih uspeo da ostvarim svoj san.

Lausanne, November 30, 2020 D. Š.

Abstract

PATIENT monitoring plays a major role in clinical scenarios where the extent and progression of suspected cardiovascular or neurological disorders are undetermined. Early detection of the presumed disorder allows healthcare professionals to provide necessary care to patients in the early stages of the disease and increases the chances for successful treatment. Furthermore, prompt disease management prevents further patient state deterioration, while significantly reducing the health-care costs associated with the patient care and treatment, which tend to rise as the disease progresses. Therefore, there is a need to identify patients at risk by monitoring them on a daily basis.

In the medical community, the most commonly used procedures for patient monitoring require prolonged hospitalizations and involve the use of cumbersome devices. The lack of portability of these devices makes them unsuitable for patient monitoring in an ambulatory setting. Luckily, new technological advancements have the potential to shape the future of healthcare by opening up new opportunities for patient monitoring through the use of wearable devices. These devices acquire and process biosignals such as Electrocardiogram (ECG) and Electroencephalogram (EEG), allowing the assessment of cardiac and brain functions.

In this thesis, I focus on monitoring of patients suffering from cardiovascular and neurological diseases through the use of wearable devices. The main diseases considered in this thesis are Atrial Fibrillation (AF), Myocardial Infarction (MI), and epilepsy. The proposed methods for the detection of the considered cardiovascular diseases use ECG as the main biosignal, whereas the main biosignal used for detecting epileptic seizures is EEG.

Firstly, I propose a hierarchical heart-rhythm classification method for AF detection from a single lead ECG recording. The proposed method is based on the features that capture the morphology of important ECG signal segments, along with heart-rate oscillations and time and frequency domain features of the ECG signal. Furthermore, the classification scheme used in this method incorporates two different classifiers: a multiclass classifier and a random forest classifier, resulting in an F_1 score of 78.95% for AF detection.

Secondly, I address the problem of early detection and prevention of MI by introducing a real-time event-driven classification technique that uses a hierarchical classifier with multiple levels. The main goal of this technique is to maintain a high classification accuracy while reducing the complexity of the classification algorithm. The reduction in computational complexity, in turn, results in a longer battery life, which is an important factor for wearable devices. The proposed technique is validated on a public database and ported on a real-life wearable device. The experimental evaluation of the proposed technique on MI data shows that this scheme reduces the energy consumption by a factor of 2.60, with no significant loss in classification performance.

The third chapter of this thesis is split into two parts and it focuses on epilepsy. In the first part, I present a real-time method for personalized epileptic seizure detection that uses EEG signals acquired from two electrode pairs: F_7T_3, and F_8T_4. The proposed method reaches a sensitivity of 90.98% and specificity of 92.10% on the database used in this study. Furthermore, this method is ported on a pair of eyeglasses in which the used electrodes are embedded and hidden in the temples, allowing for 2.71 days of operation on a single battery charge. This method overcomes the lack of portability and the effect of social stigma of EEG caps, which are used as a gold standard technique for epilepsy detection.

Since the main pitfall of epilepsy detection algorithms is the unacceptably high number of false alarms, in the last part of my thesis, I propose an interpretable patient-specific approach to false alarm reduction for epilepsy detection. This approach is based on similarly occurring morphological EEG signal patterns (seizure signature) that occur frequently during seizures. The proposed approach has been experimentally validated on more than 5500 hours of long-term EEG recordings, resulting in a high classification performance with no false positive alarms. The high degree of interpretability of this method can help physicians discover seizures faster, as well as it can be used to improve data labeling quality in publicly available databases, which confirms its applicability for long-term seizure monitoring.

Keywords: patient monitoring, wearable devices, atrial fibrillation, myocardial infarction, epileptic seizures, hierarchical classifier, event-driven classification technique, seizure signature, seizure patterns, misdetection of seizures, false positive alarms reduction.

Résumé

La surveillance continue des patients est un point essentiel dans les scénarios cliniques où des troubles cardiovasculaires ou neurologiques sont suspectés et que leur étendue et leur progression sont indéterminées. La détection précoce du trouble présumé permet aux professionnels de la santé d'apporter les soins nécessaires dès les premiers stades de la maladie, augmentant ainsi les chances de succès du traitement. En outre, une prise en charge au plus tôt de la pathologie empêche une détérioration de l'état de santé du patient tout en réduisant considérablement les coûts de la santé associés aux soins et au traitement du patient, ceux-ci ayant tendance à augmenter à mesure que la maladie progresse. Par conséquent, il est nécessaire d'identifier les personnes à risques et de les surveiller quotidiennement.

Dans le domaine médical, les démarches usuelles pour une surveillance continue des patients nécessitent une hospitalisation prolongée et l'utilisation d'appareils encombrants. Le manque de portabilité de ces dispositifs les rend inappropriés à la surveillance des patients en milieu ambulatoire. Heureusement, les dernières innovations technologiques ont le potentiel de façonner l'avenir des services de santé en offrant de nouvelles opportunités pour une surveillance des patients grâce à des appareils portatifs. Ces appareils récoltent et traitent des signaux biomédicaux tels que l'électrocardiogramme (ECG) et l'électroencéphalogramme (EEG), qui permettent l'évaluation des fonctions cardiaques et cérébrales.

Dans cette thèse, je me focalise sur la surveillance des patients atteints de maladies cardiovasculaires et neurologiques grâce à l'utilisation d'appareils portatifs. Les principales maladies considérées dans cette thèse sont la fibrillation auriculaire (FA), l'infarctus du myocarde (IM) et l'épilepsie. Les méthodes proposées pour la détection des maladies cardiovasculaires et la détection des crises d'épilepsie utilisent l'ECG et l'EEG, respectivement, comme signaux biomédicaux.

Tout d'abord, je propose une méthode de classification hiérarchique du rythme cardiaque qui permet de détecter la FA à partir d'un enregistrement ECG à une seule dérivation. La technique proposée est basée sur les caractéristiques qui définissent la morphologie des segments importants d'un signal ECG, ainsi que les oscillations de fréquence cardiaque et les caractéristiques temporelles et fréquentielles de l'ECG. En outre, le schéma de classification utilisé dans cette méthode est décomposé de deux parties : un classificateur à classes multiples et un classificateur basé sur les forêts d'arbres décisionnels. Cette méthode donne un score F1 de 78,95% pour la détection de la FA.

Deuxièmement, j'aborde le problème de la détection précoce et la prévention de l'IM en introduisant une technique de classification événementielle en temps réel basée sur une classification hiérarchique à plusieurs niveaux. L'objectif principal de cette méthode est de maintenir une précision de classification élevée tout en réduisant la complexité de l'algorithme de classification. Cela se traduit par une durée de vie de la batterie plus longue, ce qui est un facteur important pour les appareils portatifs. La technique proposée est validée sur une base de données publique et testée sur un appareil portatif réel. Cette évaluation expérimentale montre que la technique proposée réduit la consommation d'énergie d'un facteur 2.6, sans perte significative des performances de classification.

Le troisième chapitre de cette thèse est divisé en deux parties et se concentre sur l'épilepsie. Dans la première partie, je présente une méthode en temps réel pour la détection personnalisée des crises d'épilepsie qui utilise des signaux EEG acquis à partir de deux paires d'électrodes : F7T3 et F8T4. La méthode proposée obtient une sensibilité de 90,98% et une spécificité de 92,10% sur la base de données utilisée dans cette étude. Cette technique est implémentée sur un système combinant une paire de lunettes et des électrodes intégrées. Les résultats montre une autonomie de 2.7 jours en fonctionnement continu. Ce dispositif apporte une solution aux problèmes de portabilité et aux stigmatisations des bouchons EEG, qui représentent aujourd'hui le système de référence pour la détection de l'épilepsie.

Le principal problème des algorithmes de détection de l'épilepsie est le taux élevé de faux positifs. Je consacre donc la dernière partie de ma thèse à proposer une approche interprétable et propre au patient pour la réduction des fausses alarmes. Cette approche est basée sur des motifs de signaux EEG morphologiquement similaires (signature de crise) qui se produisent fréquemment pendant les crises. La méthode proposée a été validée expérimentalement sur plus de 5500 heures d'enregistrements EEG à long terme, résultant en une performance de classification élevée sans faux positif. Le degré élevé d'interprétation de cette méthode pourrait aider les médecins à découvrir les crises d'épilepsie plus rapidement. De plus, cette technique pourrait être utilisée pour améliorer la qualité de l'annotation des enregistrements dans les bases de données publiquement accessibles, ce qui confirme son utilité pour un suivi des crises épileptiques à long terme.

Mots-clés : surveillance des patients, appareils portatifs, fibrillation auriculaire, infarctus du myocarde, crise d'épilepsie, classification hiérarchique, méthode de classification événementielle, signature de crise, motifs de crises, détection erronée des crises, réduction des faux positifs

Contents

Acknowledgements **i**

Abstract (English/Français) **v**

List of Figures **xv**

List of Tables **xix**

Acronyms **xxi**

1 Introduction **1**

1.1 Cardiovascular Diseases 2
1.2 Neurological Diseases 4
1.3 Wearable Devices 5
1.4 Contributions 7
1.4.1 Contributions to Cardiovascular Diseases 7
1.4.2 Contributions to Neurological Diseases 8

2 Monitoring of Cardiovascular Diseases **9**

2.1 Human Heart Anatomy and Physiology 9
2.2 Electrocardiogram - ECG 11
2.3 2017 PhysioNet/CinC Challenge 15
2.4 Hierarchical Heart-Rhythm Classification Method 17
2.4.1 Pre-Processing 17
2.4.2 Feature Extraction 18
2.4.3 Hierarchical Classifier 21
2.4.4 Experimental Setup and Results 25
2.5 Myocardial Infarction 27
2.6 Previous Work on Detection of Myocardial Infarction 29
2.7 Motivational Example 31
2.8 Real-Time Event-Driven Classification Technique 33

2.8.1 Offline Phase of Our Real-Time Event-Driven Classification Technique 34
2.8.2 Online Phase of Our Real-Time Event-Driven Classification Technique 37
2.9 Analysis of the Proposed Real-Time Event-Driven Classification Technique 38
2.9.1 Complexity of the Proposed Real-Time Event-Driven Classification Technique 38
2.9.2 Energy Consumption of our Real-Time Event-Driven Technique 41
2.10 Experimental Setup 42
2.10.1 Classification Performance Metrics 42
2.10.2 PTB Diagnostic ECG Database 43
2.10.3 Target Platform 44
2.11 Experimental Results 45
2.11.1 Classification Quality Evaluation 45
2.11.2 Energy Consumption and System Battery Life Analysis 47

3 Monitoring of Neurological Diseases 51
3.1 Neuronal Activity 51
3.1.1 History of EEG 53
3.1.2 EEG Recording 53
3.1.3 EEG Rhythms 56
3.2 Epilepsy 57
3.3 Real-Time Method for Epileptic Seizure Detection 59
3.3.1 Feature Extraction 60
3.4 Experimental Setup and Results 62
3.4.1 CHB-MIT Database 62
3.4.2 Target Platform 62
3.4.3 Performance Evaluation 63
3.5 False Alarm Reduction for Long-Term Seizure Detection 67
3.5.1 Datasets 69
3.5.2 Personalized Seizure Signature 69
3.5.3 Real-Time Flow for the Detection of Epileptic Seizures 71
3.5.4 Evaluation Metrics 73
3.6 Results 73
3.6.1 Limitations of the proposed approach 76
3.6.2 Unlabelled seizures 76

4 Conclusions and Future Work 85
4.1 Atrial Fibrillation 86

4.2 Myocardial Infarction 87
4.3 Real-Time Method for Epilepsy Detection 89
4.4 False Alarm Reduction in Epilepsy 90

A Appendix **93**

Bibliography **95**

Curriculum Vitae **107**

List of Figures

1.1 Projected total costs of atrial fibrillation, coronary heart disease, and all Cardiovascular diseases (CVDs) in the USA 3
1.2 Global prevalence of neurological disorders 4
1.3 WBSN 6

2.1 Structure of the heart 10
2.2 The intrinsic conduction system of the heart 11
2.3 Depolarization and repolarization phase of heart muscle cells 12
2.4 ECG signal morphology 13
2.5 RR interval 14
2.6 Anomalies identified as examples of the other rhythm (OthR) class in the 2017 PhysioNet/CinC Challenge 15
2.7 Hierarchical cardiac-rhythm classification technique 17
2.8 The use of two median filter for ECG baseline wander removal 18
2.9 ECG beat morphology of a person with atrial fibrillation 19
2.10 ECG beat morphology from a person with myocardial infarction 28
2.11 Motivational example of the event-driven classification technique . . . 30
2.12 Diagram of the proposed event-driven classification technique for early detection and prevention of myocardial infarction 34
2.13 Flowchart of the online phase of the proposed event-driven classification technique for early detection and prevention of myocardial infarction 37
2.14 The prototype of the SmartCardia INYU device used to evaluate the energy consumption of the proposed event-driven classification technique for early detection and prevention of myocardial infarction 44
2.15 Classification performance of the proposed real-time event-driven classification technique versus the number of classification levels for different values of decision-making thresholds 46
2.16 Expected complexity of the proposed real-time event-driven classification technique versus the value of decision-making threshold for different number of classification levels 47

2.17 Expected complexity of the proposed real-time event-driven classification technique for early detection and prevention of myocardial infarction versus the number of classification levels for different values of decision-making thresholds 48
2.18 The energy consumption of different classification levels of the proposed event-driven classification technique for early detection and prevention of myocardial infarction. 49

3.1 Morphology of a neuron 52
3.2 The international 10-20 EEG electrode placement 55
3.3 The overall flow of the proposed method for detection of epileptic seizures 59
3.4 e-Glass: a wearable system used for evaluating the performance of the proposed method for real-time epileptic seizure detection 63
3.5 Sensitivity of the proposed method for real-time epileptic seizure detection for personalized versus generic approach using four electrodes . . 64
3.6 Specificity of the proposed method for real-time epileptic seizure detection for personalized versus generic approach using four electrodes . . 64
3.7 Geometrical mean of sensitivity and specificity of the proposed method for real-time epileptic seizure detection for personalized versus generic approach using four electrodes. 65
3.8 Sensitivity of the proposed method for real-time epileptic seizure detection for personalized approach using EEG caps versus e-Glass 66
3.9 Specificity of the proposed method for real-time epileptic seizure for personalized approach using EEG caps versus e-Glass 66
3.10 Geometric mean of the proposed method for real-time epileptic seizure for personalized approach using EEG caps versus e-Glass 67
3.11 Seizure signature for two ictal EEG recordings taken from CHB-MIT Scalp EEG database 70
3.12 Distribution of detected seizures using a seizure signature that consists of two different patterns 71
3.13 The similarity metric used for seizure detection 73
3.14 False-alarm free sensitivity of the proposed approach for seizure detection based on the personalized seizure signature 74
3.15 The measured detection latency of the proposed approach for seizure detection based on the personalized seizure signature 75
3.16 The selected seizure signature for subject chb24 from CHB-MIT database 78
3.17 The similarity metric obtained for subject chb24 from CHB-MIT database 79
3.18 Unlabelled seizures 1 for subject chb24 from CHB-MIT database 80
3.19 Unlabelled seizures 2 for subject chb24 from CHB-MIT database 81
3.20 Unlabelled seizures 3 for subject chb24 from CHB-MIT database 82

3.21 Unlabelled seizures 4 for subject chb24 from CHB-MIT database 83

List of Tables

2.1 The definition of parameters for performance scoring of the heart rhythm detection algorithms in the 2017 PhysioNet/CinC Challenge 16
2.2 List of features used for multiclass classifier for heart-rhythm classification 23
2.3 List of features used for random forest classifier for heart-rhythm classification 24
2.4 Cross-validation results obtained in the 2017 PhysioNet/CinC Challenge 25
2.5 Current used for MI detection on the target device 49

A.1 Personalized signature - CHB-MIT Database 93
A.2 Personalized signature - EPILEPSIA Database 94

Acronyms

AF	Atrial Fibrillation. v, vi, 3, 6, 7, 9, 13–19, 22, 25, 85–87
AV node	atrioventricular node. 10, 11, 13
BCG	Ballistocardiogram. 5
BSCH	basic statistical characteristics. 19, 20, 23, 24
CVDs	Cardiovascular diseases. xv, 2, 3, 7
DTW	Dynamic time warping. 71, 72
DWT	discrete wavelet transform. 43, 60
ECG	Electrocardiogram. v, xv, 1, 3, 5–9, 12–21, 23–29, 38, 42–45, 49, 58, 85–87
ECOC	error-correcting output codes. 17, 22, 23, 26, 86
EEG	Electroencephalogram. v, vi, xii, xvi, 1, 2, 4, 5, 7, 8, 51, 53–62, 65–73, 76–78, 85, 89–91
GTCS	generalized tonic-clonic seizures. 68
HR	heart rate. 5, 6, 18, 19, 21, 23, 24, 86
IoT	Internet of Things. 2
IVC	inferior vena cava. 9
LMICs	low- and middle-income countries. 2
MI	Myocardial Infarction. v, vi, xix, 3, 6–9, 27–31, 33, 38, 42, 43, 49, 85, 87
NSR	normal sinus rhythm. 14–20, 25, 86
OthR	other rhythm. xv, 15–20, 25
PPG	Plethysmograph. 5
SA node	sinuatrial node. 10, 11, 18

SVC	superior vena cava. 9, 10
v-EEG	video-EEG. 4, 5, 58
WBSN	Wireless Body Sensor Network. 5, 6

1 Introduction

THE tremendous global shift in demographics with the ageing of populations accompanied by the development of unhealthy lifestyles and irregular medical check-ups has led to a significant increase in the population prevalence of different cardiovascular and neurological diseases. Annual costs for treating people suffering from these diseases, especially those that require hospitalization, are extremely high showing a rising tendency toward the progression of these diseases. Rates of mortality are higher in lower socioeconomic groups due to their limited access to medical care and treatment. Apart from possible premature death, people suffering from these diseases, particularly neurological ones such as epilepsy, are prone to experiencing different accidents and injuries.

In order to halt disease progression and possible disease-related accidents, as well as to reduce treatment costs, there is a need to identify patients at risk by estimating a set of relevant and reliable parameters. This set of parameters will allow physicians to detect the early onset of these diseases, which is a particularly important time when these diseases can still be prevented by administering prompt emergency medication. One of the possible ways to tackle this problem is through the acquisition of biosignals.

Biosignals are signals that are acquired from a living being by measuring the difference in electrical potential between two electrodes. Depending on the electrode position, biosignal recordings can be classified into invasive and noninvasive ones. Invasive recordings are performed with electrodes placed under the skin, whereas the noninvasive ones require electrodes to be placed on the surface of the skin. In this thesis, the main signals used for monitoring of patients suffering from cardiovascular and neurological diseases are Electrocardiogram (ECG) and Electroencephalogram (EEG), respectively. These two biosignals can be used for the estimation of relevant prediction markers that provide a valuable insight into the heart and brain structures and functions. Long-term monitoring of these markers can be used for early disease detection and prevention.

Gold standard techniques used for estimating the aforementioned prediction markers are invasive and entail many risks associated with the implantation of electrodes in the human body such as infections and possible lesions (Wellmer et al., 2012). More precisely, in the case of cardiovascular and neurological diseases, these techniques are usually based on medical procedures involving a catheter insertion into the circulatory system and the use of electrodes implanted in the deep structures of the brain. Some studies have supported concerns regarding the appropriateness of catheters and implanted intracranial electrodes due to their correlation with increased morbidity and mortality (Sokolski et al., 2011; Tanriverdi et al., 2009).

On the other hand, there are also noninvasive techniques that can be used for these purposes. Several medically approved devices used in hospitals are using these noninvasive techniques for getting an insight into the patients' health status. In particular, the Holter monitor can be used for the assessment of cardiac functions, whereas the monitoring of the brain activity relies on the use of cumbersome EEG head caps. The major challenges of these devices are their high power consumption, bulkiness, lack of portability, and social stigma associated with their use, which make them inconvenient to be used for ambulatory and home-based monitoring.

The revolutionizing era of the Internet of Things (IoT) offers the possibility for long-term patient monitoring through the use of wearable devices. The portable and non-intrusive characteristic of these devices enables monitoring of patients on a daily basis outside of clinical environments, reducing patient discomfort during everyday activities.

1.1 Cardiovascular Diseases

Cardiovascular diseases (CVDs) represent the leading global cause of death and disability nowadays, taking an estimated 17.9 million lives every year (WHO, 2020). These diseases include different conditions affecting the structures of the heart and blood vessels. CVDs make the largest contribution to mortality especially in low- and middle-income countries (LMICs) due to lack of benefits of health-care services for early detection and treatment of people. More precisely, more than 75% of deaths related to CVDs occur in LMICs, leading to growing inequalities in the occurrence and outcome of CVDs between countries and populations (WHO, 2020).

Apart from a negative effect on people's health, the economic burden of these diseases is enormous. Costs attributable to CVDs can be split into direct and indirect ones.

Direct costs include money spent on medical services via a physician or healthcare system, along with the corresponding costs, such as prescription medication and home healthcare. On the other side, indirect costs are related to lost productivity. Total costs (direct+indirect) of CVDs in the USA were estimated at $555 billion in 2015 and are expected to rise over $1.1 trillion (Association, 2017), which is shown in Fig. 1.1. Unless addressed, the mortality and disease burden from CVDs will continue to increase.

Some CVDs can still be prevented by addressing behavioral risk factors, mainly tobacco use, harmful use of alcohol, physical inactivity, and unhealthy diet. These risk factors significantly contribute to the development of Atrial Fibrillation (AF) (Brandes et al., 2018) and Myocardial Infarction (MI) (Greenlund et al., 2005). The development of these diseases is accompanied by changes in the heart functions and structures that are directly reflected in the morphology of the recorded ECG. In the medical community, the criterion standard for detecting these ECG changes involves the use of 12 different leads. Apart from a long setup needed for signal acquisition, the main disadvantages of the 12-lead ECG are its lack of portability and high energy consumption.

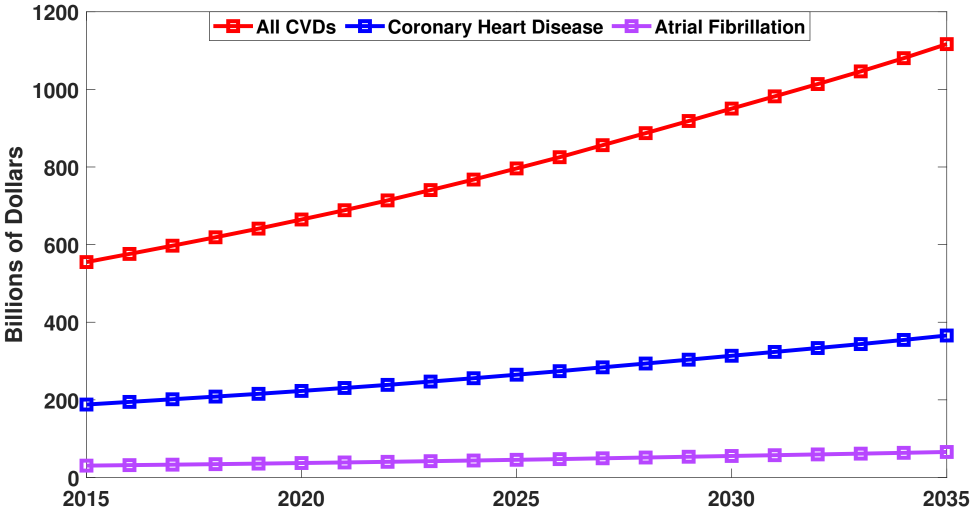

Figure 1.1: Projected total costs of atrial fibrillation, coronary heart disease and all CVDs in the USA (Khavjou et al., 2016).

1.2 Neurological Diseases

Neurological diseases are medically defined as disorders that affect the brain as well as the nerves found throughout the human body and the spinal cord (WHO, 2016). These disorders include epilepsy, Alzheimer's disease and other dementias, Parkinson's disease, multiple sclerosis, migraine, cerebrovascular diseases including stroke, and different neuroinfections (WHO, 2016).

As it is shown in Fig.1.2, epilepsy is among the most prevalent neurological diseases worldwide affecting people of all ages. People with epilepsy face considerable difficulties in their daily lives associated with their independence, education, employment, driving licence status, as well as social integration (de Boer et al., 2008). Additionally, they experience profound psychological consequences contributing to the development of anxiety disorders, depression, and low self-esteem (de Boer et al., 2008). The fear of having a seizure has a detrimental impact on patient's quality of life and psychosocial functioning. Furthermore, the unforeseeable nature of epileptic seizures may sometimes lead to different accidents such as: soft tissue injuries, fractures, as well as serious head injuries (Nguyen and Zenteno, 2009). The most severe seizures that involve profound unresponsiveness may have a lethal outcome (Ryvlin et al., 2009). To reduce the incidence of seizure-related accidents, long-term seizure monitoring is of utmost importance for alerting caregivers and health-care professionals to help a person during a seizure.

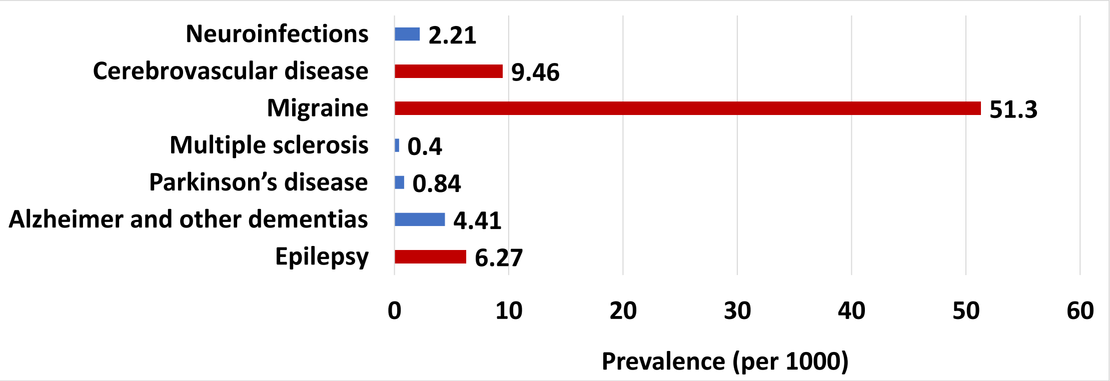

Figure 1.2: Global prevalence (per 1000) of neurological disorders in 2015 (WHO, 2015).

One of the standard methods for monitoring of epileptic patients entails the use of video-EEG (v-EEG) along with the simultaneous recording of electrical brain activity extracted from the scalp EEG (Cascino, 2002). This procedure is commonly performed in hospitals by neurologists who look for abnormal brain activities reflected onto EEG signals. Particularly, neurologists inspect the EEG signal morphology trying to find specific wave patterns that indicate the presence of seizures. In case of their absence, v-EEG along with other complementary neuroimaging techniques is used to confirm the presence of seizures. Nevertheless, v-EEG monitoring is more complicated than EEG requiring hospital admission over several days. Furthermore, the scalp EEG is acquired through the use of cumbersome EEG head caps that use from 23 to 256 wired electrodes requiring the subject to be seated. The lack of portability of EEG caps and associated stigma make them inconvenient to be used for ambulatory and home-based monitoring.

1.3 Wearable Devices

The latest technological developments have caused a massive spread of wearable devices. These devices feature different sensors such as ECG, Ballistocardiogram (BCG), Plethysmograph (PPG), accelerometer, gyroscope, etc, as well as a user interface that communicates various data to the user in real-time. Thanks to these sensors, wearables allow the continuous monitoring of different vital body parameters such as heart rate (HR), blood pressure, body temperature, blood oxygen saturation, posture, etc.

One of the main design challenges of wearables include battery life, compactness, comfort, and device safety. As these devices rely on batteries as the primary energy source, their energy consumption should be as low as possible to allow them to monitor and measure different body parameters continuously. Furthermore, they should be miniaturized without affecting the degree of comfort the wearer experiences while wearing them. Moreover, their usage should not harm the user, hence safety mechanisms should be integrated into these devices.

Wearable devices can be used for different purposes. Tracking physical activities through the use of wearables has become one of the most popular methods to assess activity intensity and energy expenditure. Furthermore, these devices also find application in fall prevention, stress detection, weight monitoring, as well as patient management. Allowing reliable and noninvasive diagnostics, while being appealing to patients thanks to the small form-factor enabled by the modern system-on-chip technology, these devices represent a promising solution for long-term monitoring. The ability to be worn along with the inconspicuous nature of these devices enables patients to avoid social stigma of wearing cumbersome apparatuses, such as EEG head caps mentioned in Section 1.2.

Wearable technologies offer a possibility of assessing cardiac and brain functions on a daily basis. This is usually done through the use of a Wireless Body Sensor Network

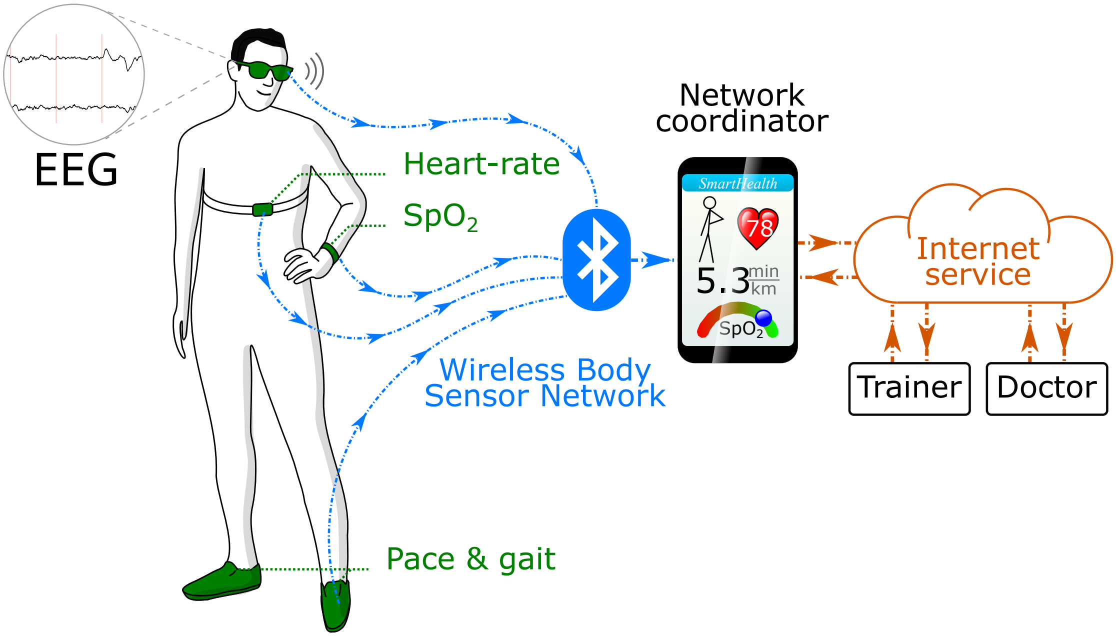

Figure 1.3: WBSN composed of a smartphone as a network coordinator and four different wearable devices: smart-glasses, cardiac monitoring belt, smart-watch, and smart-shoes. [Taken and modified with permission from (Surrel, 2019).]

(WBSN) which represents a fusion of different wearable devices. A smartphone is typically used to collect information from these sensors and transmit it wirelessly to a remote server for storage and further analysis. An example of a WBSN composed of four different wearable devices is shown in Fig. 1.3. Sending medical data to physicians opens up the possibility of evaluating cardiac and brain functions and, subsequently, provides care to patients in the ambulatory settings rather than admitting them to hospital for assessment of their health status.

Sending raw signals acquired through wearables over the energy-hungry wireless link has a detrimental effect on the energy consumption of these devices, and consequently, battery life. One of the possibility to reduce energy consumption lies in processing data directly on the device. Depending on the specific application, only valuable clinical data should be sent to a remote server for patient health status assessment. For instance, previously mentioned sport-tracking monitors acquire the full ECG signal, but they only report the value of HR, resulting in extended battery life of these devices.

Apart from performing the entire processing on the device, another way to optimize the energy consumption of wearable devices is by acquiring a lower amount of data. Even though the medical standard for ECG signal acquisition requires 12 different leads, specific heart irregularities such as AF and MI can still be detected based on the ECG signal morphology acquired from only one lead. On the other side, the main drawbacks of EEG caps mentioned in Section 1.2 can be overcome by reducing the number of EEG channels needed for detection of epileptic seizures. While significantly lowering the overall energy consumption of wearable devices, the reduction in the number of signals' channels might have an impact on the device performance, resulting in a high number of false positive alarms. Nevertheless, some adaptive algorithms running on wearable devices allow the user to report false positive alarms and re-tune the parameters of the algorithm. More specifically, each time a false positive alarm occurs, the user can manually enter it on the device which will re-train the algorithm on the device, taking into consideration this false alarm. Furthermore, in order to achieve a high performance accuracy, the parameters used in algorithms running on wearable devices should be tailored to each patient, which will be shown in this thesis.

1.4 Contributions

The main contributions to this thesis are related to the monitoring of patients suffering from cardiovascular and neurological diseases using wearable devices. The main CVDs considered in this thesis are AF and MI. The proposed method for AF classification from a short single lead ECG recording and the proposed technique for early detection and prevention of MI on wearable devices are presented in Chapter 2. For neurological diseases, the main focus is set on epilepsy. More precisely, in the first part of Chapter 3, I propose an algorithm for the detection of epileptic seizures that uses four EEG electrodes that can be embedded and hidden in the temples of eyeglasses. In the last part of Chapter 3, I present an interpretable approach to false alarm reduction for long-term epileptic seizure detection.

1.4.1 Contributions to Cardiovascular Diseases

The main contributions to this thesis related to the monitoring of patients suffering from CVDs, specifically AF and MI, are:

- Hierarchical heart-rhythm classification method for distinguishing AF from normal sinus and other heart rhythms.
- Classification performance evaluation of the proposed hierarchical heart-rhythm classification method on the 2017 PhysioNet/CinC Challenge (Clifford et al., 2017).
- Real-time early detection and prevention of MI using an event-driven classifica-

tion technique that uses a hierarchical classifier with multiple levels.

- Analysis of computational complexity and energy efficiency of the proposed hierarchical classifier, as well as the design flow that allows users to synthesize high-accuracy event-driven hierarchical classifiers that meet user's battery life requirements.
- Classification performance evaluation of the proposed event-driven classification technique on the MI database (Physiobank - PTB Diagnostic ECG database (Goldberger et al., 2000)).
- Porting the proposed classification technique on a real-life wearable device, including a detailed evaluation of energy consumption and battery life for the case of MI.

1.4.2 Contributions to Neurological Diseases

The main contributions to this thesis related to the monitoring of patients suffering from neurological diseases, particularly epilepsy, are:

- Real-time method for epileptic seizure detection that uses EEG signals acquired from four electrodes and can run on a wearable device.
- Classification performance evaluation of the proposed method for epileptic seizure detection on CHB-MIT Scalp EEG database (Goldberger et al., 2000; Shoeb, 2009).
- Porting the proposed method for epileptic seizure detection on an inconspicuous pair of eyeglasses in which the used EEG electrodes are integrated in the temples, and estimating the battery life and energy consumption of this device.
- Interpretable approach to false alarm reduction for long-term epileptic seizure detection based on similarly occurring morphological EEG signal patterns.
- Classification performance evaluation and detection latency estimation of the proposed approach to false alarm reduction on CHB-MIT Scalp EEG database (Goldberger et al., 2000; Shoeb, 2009) and the European Epilepsy Database (surface recordings) (Ihle et al., 2012).
- Identifying unlabelled seizures in both, CHB-MIT database (Goldberger et al., 2000; Shoeb, 2009) and the European Epilepsy Database (surface recordings) (Ihle et al., 2012).

2 Monitoring of Cardiovascular Diseases

THIS chapter provides an introduction to the heart anatomy and physiology along with the electrical system of the heart. Furthermore, the basic principles of Electrocardiogram (ECG) along with the ECG signal morphology of the normal sinus rhythm are discussed. Then, a heart-rhythm classification method for differentiating Atrial Fibrillation (AF) from normal sinus rhythm and other cardiac arrhythmias along with the dataset used for its evaluation is described. Finally, the last part of this chapter focuses on early detection and prevention of Myocardial Infarction (MI) presenting a novel real-time event-driven classification technique for wearable systems.

2.1 Human Heart Anatomy and Physiology

The human heart is a muscle that pumps blood throughout the body via the cardiovascular system. In order to do its work, it requires a constant supply of oxygen. Oxygen is supplied to the heart by the coronary arteries that wrap around the outside of the heart. The inside of the heart is divided into four heart compartments: two upper chambers called the atria (right and left) and two lower chambers called the ventricles (right and left). The structure of the heart along with the pathway of blood flow through the heart is shown in Fig. 2.1.

The arrows in Fig. 2.1 indicate the blood flow. More precisely, oxygen-poor blood from the body returns to the right atrium of the heart through two veins: the superior vena cava (SVC) and the inferior vena cava (IVC). Blood from the upper part of the body returns through the SVC, whereas blood from the lower body returns through the IVC. As soon as the right atrium gets filled with blood, it contracts pumping blood into the right ventricle through the open tricuspid valve. Once the right ventricle is filled, the tricuspid valve closes preventing blood from flowing backward into the right atrium. Then, the right ventricle contracts, the pulmonary valve opens, and blood is

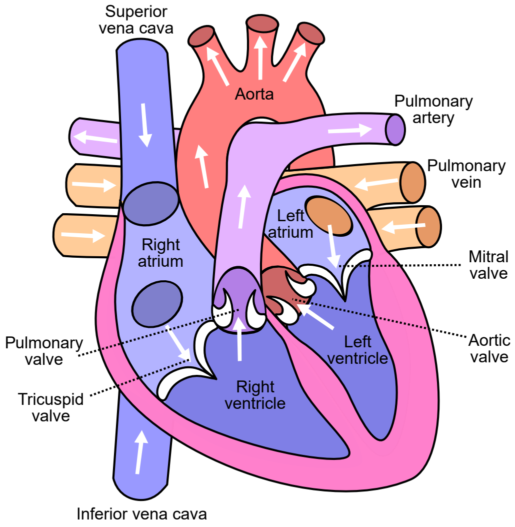

Figure 2.1: Structure of the heart. Blood flow through the chambers and heart valves. [ⓒⓘⓞOriginal by Wapcaplet, updated by Yaddah.]

pumped into the pulmonary artery reaching the lungs where it is oxygenated. The pulmonary valve shuts to prevent blood from flowing back into the ventricle. After picking up oxygen, oxygen-enriched blood from the lungs returns to the left atrium of the heart via the left pulmonary vein. When the left atrium is filled with blood it contracts, the mitral valve opens and blood is pumped into the left ventricle of our heart. This occurs at the same time as the right atrium pumps blood into the right ventricle on the other side of the heart. Once the left ventricle is full, the mitral valve shuts, the aortic valve opens, the left ventricle contracts and oxygen-enriched blood is pumped into the aorta to reach all parts of the body. This happens at the same time as the right ventricle pumps blood into the pulmonary artery on the other side of the heart. The aortic valve quickly closes to prevent blood from flowing back to the heart. Meanwhile, the atrium is filled with blood and the cycle repeats itself.

During a normal heartbeat called a cardiac cycle, the contraction of both, the atria and ventricles is controlled by the intrisic cardiac conduction system, shown in Fig. 2.2. The starting point of this system is the sinuatrial node (SA node) which is a mass of cells located in the right atrium near the opening of the SVC. The SA node is often referred to as the primary pacemaker of the heart as it determines the rate at which the heart beats (Goldberger et al., 2013). Each heartbeat is initiated by an electrical stimulus generated automatically in the SA node that spreads throughout both atria and stimulates them to contract. The electrical activity arrives to the atrioventricular node (AV node) that serves as electrical gateway to the ventricles. The AV node delays the passage of electrical impulses to the ventricles, allowing blood to pass from the

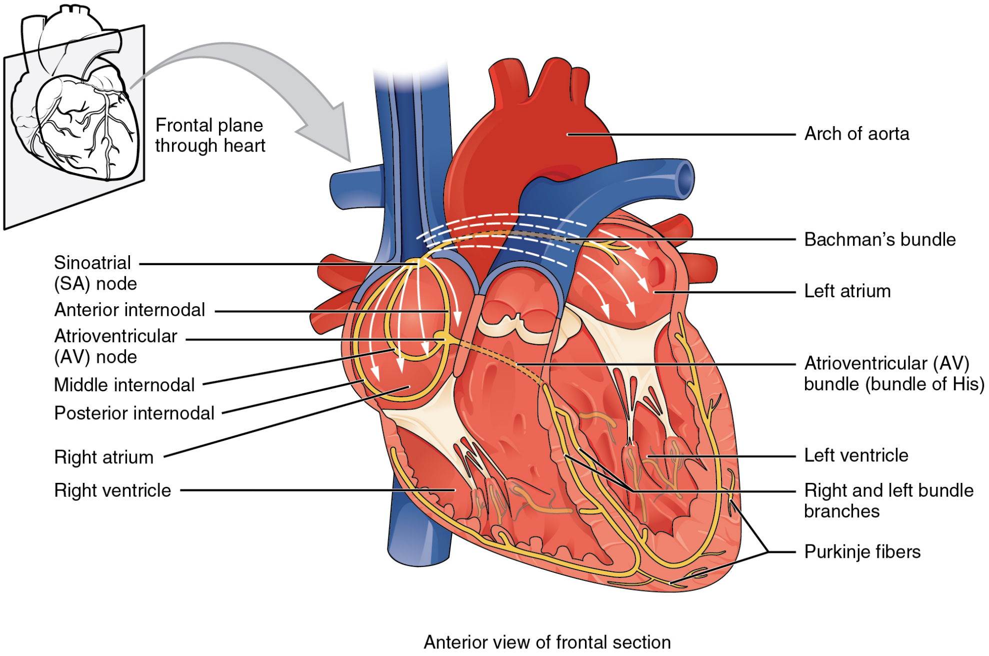
Frontal plane
through heart
Arch of aorta
Bachman's bundle
Left atrium
Atrioventricular (AV)
bundle (bundle of His)
Left ventricle
Right and left bundle
branches
Purkinje fibers
Sinoatrial
(SA) node
Anterior internodal
Atrioventricular
(AV) node
Middle internodal
Posterior internodal
Right atrium
Right ventricle
Anterior view of frontal section

Figure 2.2: The intrinsic conduction system of the heart. [©OpenStax, Anatomy & Physiology.]

atria down into the ventricles and to fill them with blood. After passing through the AV node, the impulse is rapidly transmitted via a pathway called the bundle of His, and then into the ventricles. The bundle of His divides into right and left pathways to provide simultaneous electrical stimulation to both ventricles. Finally, the signals are then passed onto Purkinje fibers causing the contraction of the ventricles. As the ventricles contract, the blood is ejected, either to the lungs through the pulmonary artery or to the body through the aorta. As soon as the SA node fires another impulse, the entire cycle begins again.

2.2 Electrocardiogram - ECG

The two main events of the cardiac cycle include (Goldberger et al., 2013):

- Depolarization - the spread of electrical signals throughout the atria and ventricles
- Repolarization - the return of heart muscle cells to their resting state following depolarization

Namely, at their resting state, heart muscle cells are polarized, i.e., they carry electrical

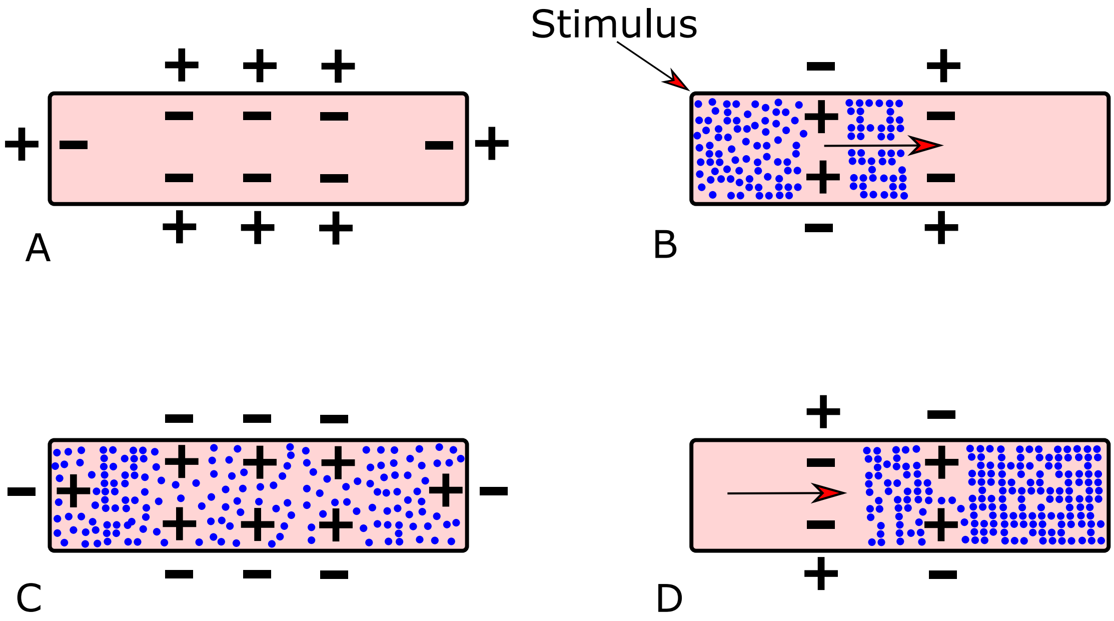

Figure 2.3: Depolarization and repolarization phase of heart muscle cells. **A**, a heart cell at rest. **B**, The beginning of the depolarization phase. **C**, The fully depolarized cell. **D**, The beginning of the repolarization phase. The directions of depolarization and repolarization are represented by arrows.

charges on their surface. This polarization is determined by different concentrations of ions inside and outside the cell, as well as by the permeability of the cell membrane to different types of ions. At rest, the inside of the cell is more negative than the outside, as shown in Fig. 2.3 A. When the heart cell gets stimulated, it depolarizes making the area where the stimulation happened more positive on the inside, and more negative on the outside (Goldberger et al., 2013). Hence, an electrical current that propagates along the cell is generated, as shown in Fig. 2.3 B. This leads to depolarization of the entire cell, Fig. 2.3 C. Depolarization is followed by repolarization in which the cell begins to return to its resting state, by making a small area on the outside of the cell positive again, as shown in Fig. 2.3 D. The repolarization spreads across the entire cell until the cell goes back to its resting state.

The electrical activity of the heart can be recorded in the form of an ECG, shown in Fig. 2.4. The ECG tracing consists of three main forms: the P wave, the QRS complex, and the T wave, and can further be decomposed into: the PR interval, the PR segment, the ST segment, and the QT interval. Each of these forms corresponds to certain events of the cardiac cycle. More precisely, the P wave and the QRS represent atrial and ventricular depolarization, respectively. The ventricular repolarization is represented by the T wave. The atrial repolarization occurs during ventricular

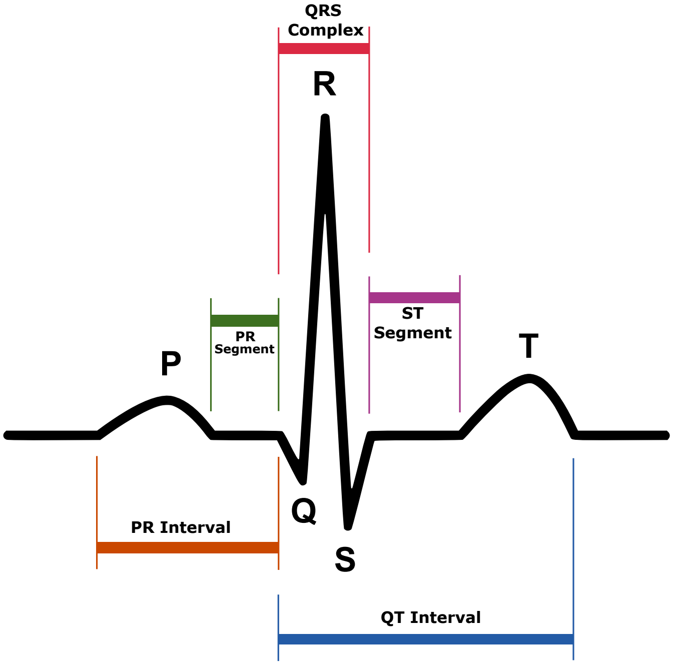

Figure 2.4: ECG signal morphology.

depolarization. However, since the ventricles tend to contract stronger than the atria, the wave of atrial repolarization is small in amplitude, and hence, it is masked by the QRS complex. The PR interval, represents the time from the onset of atrial depolarization to the onset of ventricular depolarization, whereas the QT interval represents the time of ventricular depolarization and subsequent repolarization. PR- and ST-segment reflect the time delay of the electrical impulse in the AV node and the time between ventricular depolarization and repolarization, respectively (Stouffer, 2009). The R-R interval shown in Fig. 2.5 represents the time between consecutive QRS complexes and it is inversely proportional to the heart rate, i.e.,

$$\text{RR (in sec)} = \frac{60}{\text{HR (in beats/min)}}. \tag{2.1}$$

The ECG is the essential clinical test for interpretation of the cardiac rhythm and conduction system abnormalities (Stouffer, 2009). Abnormal conduction of electrical impulses within the heart, as well as some pathological heart conditions produce characteristic deviations of different ECG segments. One of these pathological heart conditions is AF.

AF is one of the most common types of cardiac arrhythmia. In 2010, 20.9 and 12.6

million men and women were affected worldwide, respectively, with higher rates in developed countries (Kirchhof et al., 2016). It may manifest in short episodes rather than a sustained condition, which increases detection complexity. Despite the progress in detection and treatment of AF, the arrhythmia remains one of the major risk factors for stroke and heart failure (Kirchhof et al., 2016).

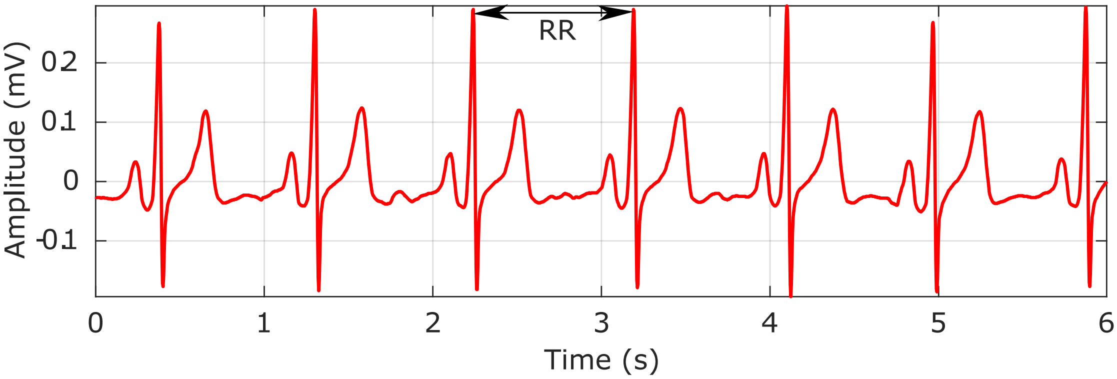

Figure 2.5: RR interval. Taken from record A00848 from the PhysioNet Challenge 2017 database.

Conventionally, AF is diagnosed by analyzing ECG, and a typical pattern is associated to an AF episode: abnormal atrial activity and irregular ventricular response. Previous studies analyze the two responses either separately or combined to discriminate AF from normal sinus rhythm (NSR). The need to capture the abnormal atrial activity has given rise to a plethora of studies. In (Ladavich and Ghoraani, 2015), the authors construct a statistical model of NSR P-waves to capture the absence of P-waves or the presence of F-waves, which appear as a "sawtooth" pattern hiding a clear P-wave in AF. Another similar study that analyzes the atrial activity is described in (Ródenas et al., 2015) in which AF episodes are detected based on wavelet entropy and the energy on several wavelet scales computed for each ECG beat. On the other side, the effect of AF on ventricular activity consists mainly in analyzing the irregularity of RR intervals. In (Zhou et al., 2014), the authors propose a method for real-time automated detection of AF episodes considering symbolic dynamics and Shannon entropy to describe the dynamic behaviour of RR-interval time-series. Nevertheless, the combined analysis of atrial and ventricular responses can improve the accuracy of AF detection. For instance, a method proposed by (Rincon et al., 2012) combines heart-rate and P-wave analysis to detect AF in real-time on a wearable device. Although the classification of NSR and AF from a surface ECG has been investigated for many years, distinguishing AF from other types of arrhythmias still remains a challenging task, as many non-AF arrhythmias exhibit irregular RR intervals (Clifford et al., 2017; Gayathri et al., 2012).

2.3 2017 PhysioNet/CinC Challenge

As one of the contributions to this thesis, I tackled the problem of discriminating AF from NSR and other types of cardiac arrhythmias in short term ECG recordings. For this purpose, I took part in the 2017 PhysioNet/CinC Challenge in which a total of 8,528 ECG signal recordings lasting from 9–61 seconds were provided as a publicly available training test (Clifford et al., 2017). Four classes of recordings were considered: NSR, AF, other rhythm (OthR), and noisy signals (Noise). The OthR class consists of different cardiac anomalies. Some of these anomalies are shown in Fig. 2.6. The proposed method used for this Challenge is described in Subsection 2.4.

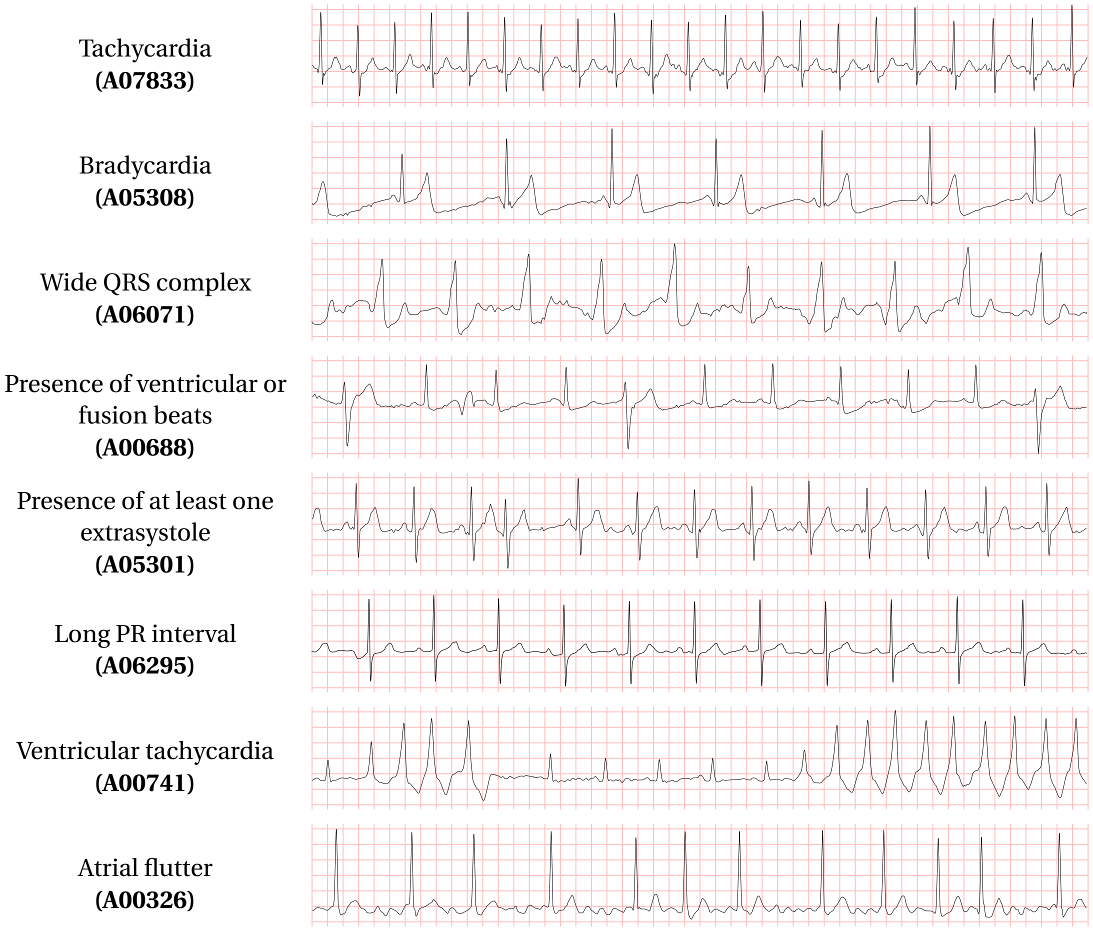
Tachycardia
(A07833)
Bradycardia
(A05308)
Wide QRS complex
(A06071)
Presence of ventricular or fusion beats
(A00688)
Presence of at least one extrasystole
(A05301)
Long PR interval
(A06295)
Ventricular tachycardia
(A00741)
Atrial flutter
(A00326)

Figure 2.6: Anomalies identified as examples of the OthR class in the 2017 PhysioNet/CinC Challenge. [Taken from (Teijeiro et al., 2018) with permission.]

All ECG recordings were sampled at $f_s = 300\text{Hz}$ and were acquired with a commercial single-channel ECG device (Clifford et al., 2017). A hidden set that consisted of 3,658 recordings of similar lengths and class distributions was not provided to the public. This set was used by the Challenge organizing committee as a test set to evaluate the performance of the proposed algorithms. The definitions of parameters used for performance scoring are provided in Table 2.1:

		Predicted classification				
		NSR	AF	OthR	Noise	Total
Reference classification	NSR	N_n	N_a	N_o	N_p	$\sum N$
	AF	A_n	A_a	A_o	A_p	$\sum A$
	OthR	O_n	O_a	O_o	O_p	$\sum O$
	Noise	P_n	P_a	P_o	P_p	$\sum P$
	Total	$\sum n$	$\sum a$	$\sum o$	$\sum p$	

Table 2.1: The definition of parameters for performance scoring of the heart rhythm detection algorithms in the 2017 PhysioNet/CinC Challenge. (Clifford et al., 2017).

For each of the classes, the F_1 measure is defined as follows:

$$\begin{aligned}
\mathsf{F}_{\mathsf{NSR}} &= \frac{2 \cdot N_n}{\sum N + \sum n} \\
\mathsf{F}_{\mathsf{AF}} &= \frac{2 \cdot A_a}{\sum A + \sum a} \\
\mathsf{F}_{\mathsf{OthR}} &= \frac{2 \cdot O_o}{\sum O + \sum o} \\
\mathsf{F}_{\mathsf{Noise}} &= \frac{2 \cdot P_p}{\sum P + \sum p}
\end{aligned} \tag{2.2}$$

The final scoring function $\mathsf{F}_{\mathsf{FINAL}}$ used in this challenge is an average of F_1 values from normal sinus, atrial fibrillation, and other rhythm, defined as follows:

$$\mathsf{F}_{\mathsf{FINAL}} = \frac{\mathsf{F}_{\mathsf{NSR}} + \mathsf{F}_{\mathsf{AF}} + \mathsf{F}_{\mathsf{OthR}}}{3}. \tag{2.3}$$

2.4 Hierarchical Heart-Rhythm Classification Method

The overall flow of the proposed hierarchical method for heart-rhythm classification is shown in Fig. 2.7 and it consists of three main phases: pre-processing (Subsection 2.4.1), feature extraction (Subsection 2.4.2), and hierarchical classifier (Subsection 2.4.3). The hierarchical classifier comprises two different classifiers: a multiclass classifier based on error-correcting output codes (ECOC) and a random forest classifier for binary decision making. Each of these three main phases is thoroughly explained in the following sections.

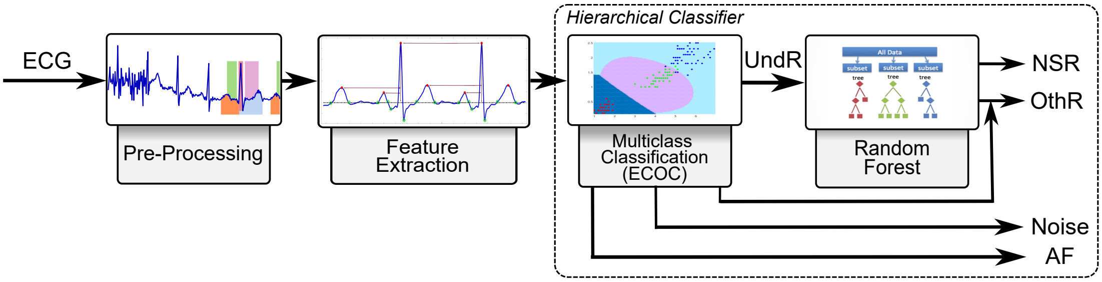

Figure 2.7: Hierarchical cardiac-rhythm classification technique for four classes of signals: NSR, OthR, noisy signals (Noise), and AF. In the case of getting undefined rhythm (UndR) at the output of the ECOC classifier, a random forest classifier is used for binary decision making.

2.4.1 Pre-Processing

As a first step, the ECG signals are filtered to remove the baseline wander and high frequency noise. Firstly, two median filters are used for ECG baseline wander removal based on the work described in (de Chazal et al., 2003). The first median filter of 200ms width is used to remove QRS complexes and P waves. Then, the resulting signal is further processed with a median filter of 600ms width to remove all T waves. The signal at the output of the second median filter contains the ECG baseline wander and is subtracted from the original ECG signal resulting in a baseline-free signal. The use of these two median filters is illustrated in Fig. 2.8. After removing the baseline wander, a 32nd-order zero-phase FIR band-pass filter with cut-off frequencies $f_1 =$ 0.05Hz and $f_2 =$ 40Hz is applied for high-frequency noise and artefact removal. Then, the R-peaks of the ECG signals are detected using Pan-Tompkin's algorithm (Pan and Tompkins, 1985).

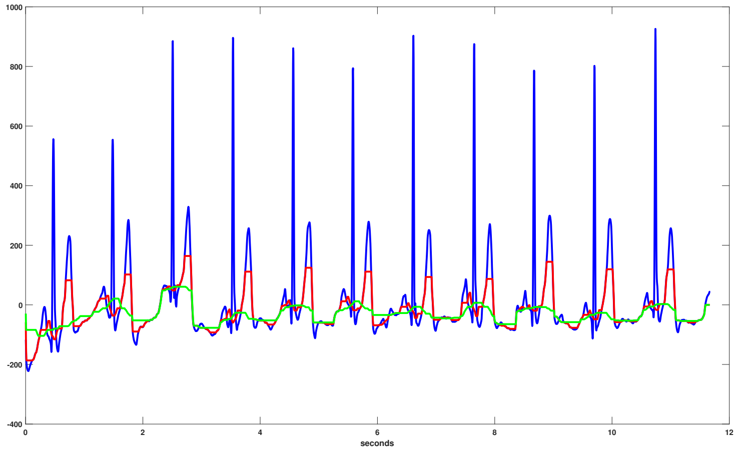

(a) The original ECG signal is shown in blue. Signals at the output of the first and second median filter are shown in red and green, respectively. The signal shown in green represents the ECG baseline wander.

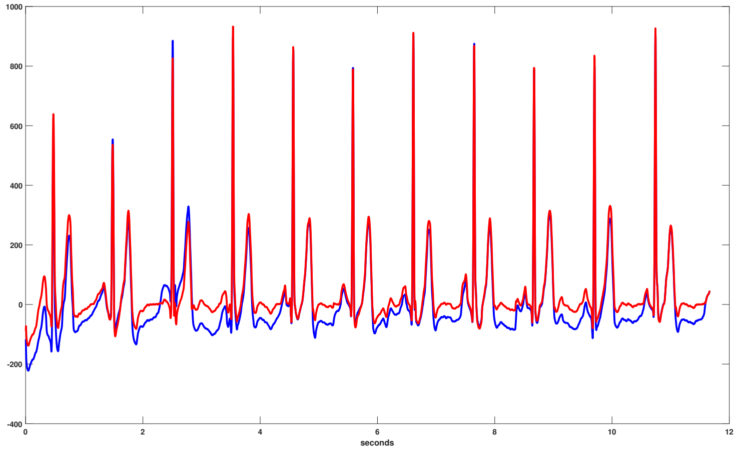

(b) The baseline-free ECG signal shown in red is obtained by subtracting the ECG baseline wander from the original ECG signal shown in blue.

Figure 2.8: The use of two median filter for ECG baseline wander removal. Recording **A00026** from the 2017 PhysioNet/CinC Challenge. (Clifford et al., 2017).

2.4.2 Feature Extraction

In the following subsections, the features used for heart rhythm classification are thoroughly explained. As previosuly mentioned, four different types of signals are considered: NSR, AF, OthR, and noisy signals. NSR is any cardiac rhythm where depolarization of the cardiac muscle begins in the SA node with a heart rate (HR) of 60 – 100 bpm (Clifford et al., 2017). The representation of NSR is shown in Fig. 2.9a. On the other side, as it can be seen in Fig. 2.9b, AF records are characterized by the absence of the P wave (Ladavich and Ghoraani, 2015). Moreover, most AF records also exhibit irregular RR intervals (Zhou et al., 2014). However, many different types of arrhythmias OthR could exhibit irregular RR intervals (Clifford et al., 2017; Gayathri et al., 2012). The last class of signals contains signals that are too noisy to be classified (Clifford et al., 2017).

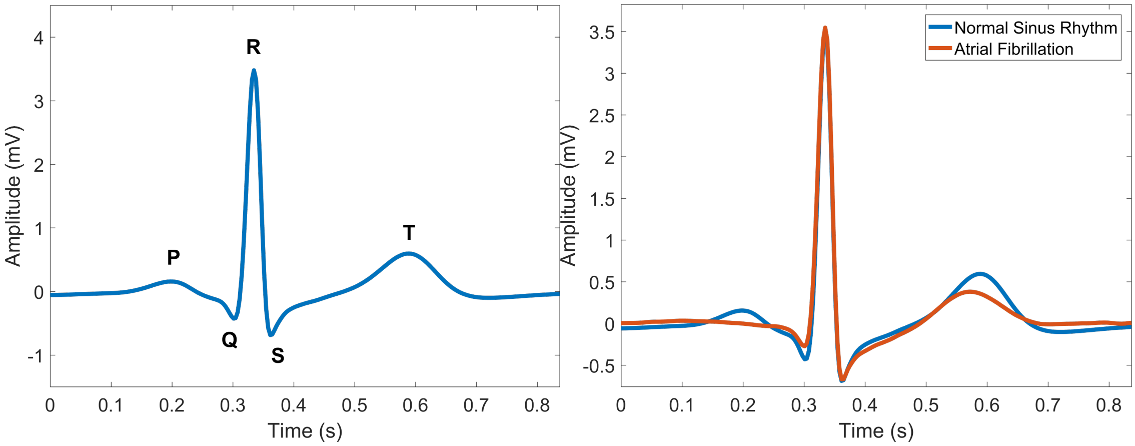

(a) NSR.

(b) NSR versus AF

Figure 2.9: The morphology of an ECG beat of NSR versus an ECG beat of AF with absent P wave.

HR–Based Features: The instantaneous HR is calculated based on Eq. (2.1). HR signal as well as its first, second, and third-order derivatives are used as the main signals for feature extraction. The minimum value, the maximum value, the mean value, the median value, the standard deviation, as well as and the Euclidean norm of these four signals are considered. These features are referred to as basic statistical characteristics (BSCH) of a signal in the remainder of this section. Two additional features are defined to describe bradycardia and tachycardia. The former represents the percentage of HR values that are below 40 bpm, whereas the latter is defined as the percentage of HR values that are above 140 bpm. Additionally, the extreme bradycardia feature captures if the value of HR falls below 40 bpm for any five consecutive beats, whereas the extreme tachycardia feature captures if the HR is above 140 bpm for any 17 consecutive beats. Moreover, three binary features $\mathsf{F}_{\mathsf{limit}_1}$, $\mathsf{F}_{\mathsf{limit}_2}$, and $\mathsf{F}_{\mathsf{limit}_3}$ are used to determine the average value of the instantaneous HR across the entire signal recording. Namely, features $\mathsf{F}_{\mathsf{limit}_1}$ and $\mathsf{F}_{\mathsf{limit}_2}$ capture whether the average HR is above 100 bpm and 130 bpm, respectively, whereas, feature $\mathsf{F}_{\mathsf{limit}_3}$ captures if the average HR is below 40 bpm.

P–Wave and T–Wave Features: As one of the main characteristics of AF records is the absence of the P-wave in the ECG signal, for each heart beat the part of the signal corresponding to the P-wave is extracted, resulting in matrix **P** in which each column represents the P wave of one heart beat. Similarly, matrices $\mathbf{P}^{(1)}$, $\mathbf{P}^{(2)}$, $\mathbf{P}^{(3)}$ represent the first, second, and third-order derivative of each P-wave. As matrix $\mathbf{P}$ contains all P-waves, the following five vectors are constructed: $\mathbf{p_{max}}$, $\mathbf{p_{min}}$, $\mathbf{p_{mean}}$, $\mathbf{p_{median}}$, and $\mathbf{p_{std}}$. These vectors are obtained by calculating the minimum, maximum, average, median and standard deviation values of each P-wave, respectively. BSCH of these vectors are used in the set of features. In addition, vectors $\mathbf{p_{norm}}$, $\mathbf{p^{(1)}_{norm}}$, $\mathbf{p^{(2)}_{norm}}$, $\mathbf{p^{(3)}_{norm}}$ are constructed by calculating the Euclidean norm of each P-wave along with the norms of their first, second, and third-order derivative, and BSCH of each of these vectors are used as features. Analogously, BSCH of vectors obtained from matrices $\mathbf{P}^{(1)}$, $\mathbf{P}^{(2)}$, $\mathbf{P}^{(3)}$ are also included. Furthermore, the pairwise linear correlation coefficient between all P-waves is calculated, resulting in a $p \times p$ matrix $\mathbf{P_{corr}}$, where p represents the number of R peaks of ECG signal. In order to capture the variability in P-waves, signal s_p is defined. This signal is obtained by concatenating all parts of the signal that correspond to P-waves, as well as feature f_p defined as:

$$f_p = \frac{\sum_{i=1}^{p} \mathbf{P_{corr}} - \mathrm{trace}(\mathbf{P_{corr}})}{p^2 - p},$$

where $\mathrm{trace}(\mathbf{P_{corr}})$ represents the sum of the elements of the main diagonal of matrix $\mathbf{P_{corr}}$. The normalized power of s_p in the frequency band $[0, 30]$Hz, as well as the Shannon entropy of s_p are also considered in the final set of features. Furthermore, the first, second, and third-order derivatives of s_p are also calculated. BSCH of these signals are added to the final set of features, along with the percentage of times where the peak of the P-wave is negative. Similarly, by concatenating all signal parts that correspond to the T wave, signal s_t is defined. The normalized power of this signal in frequency bands $[0, 5]$Hz and $[5, 30]$Hz, along with its Shannon entropy is calculated. These two frequency bands have been selected, as clear differences in power were noticed for NSR and OthR classes.

Time- and Frequency–Domain Features: Abnormalities in the generation and/or conduction of electrical impulses throughout the heart may affect the duration of different ECG segments such as the PR interval, the PP interval, the QRS width, and the QT interval. The duration of the normal PR interval in adults is between 0.12 and 0.2 seconds (Goldberger et al., 2013). As previously mentioned, this interval represents the time it takes for an electrical impulse to spread through the atria and pass through the AV junction. When the spread of the electrical impulse through the AV junction is impaired, the PR interval may become prolonged. Furthermore, the atrial and ventricular rate for NSR are the same, whereas in the case of AV conduction delay these rates may differ. Therefore, to capture the delay in the AV junction as well as to determine the atrial rate, the PR and the PP interval are used. The PR interval is calculated from the peak of the P-wave to the Q-wave of the ECG signal. Basic statistical characteristics of the PR intervals along with the ratio between standard deviations of the PR and RR intervals are used as features. The PP interval is defined as the distance between two consecutive P-wave peaks and represents the atrial rate. To compare the atrial and ventricular rate, the ratio between the mean values of the PP and RR intervals, as well as their standard deviations are added to the feature set.

On the other side, the spread of a stimulus through the ventricles is reflected onto the QRS width. Normally, the QRS width is 0.1 sec or less (Goldberger et al., 2013). However, when the spread of a stimulus is slowed, the QRS width gets lengthened. Additionally, the duration of ventricular contractions can be estimated using the QT interval. Therefore, the QRS width and the QT interval are used to capture the spread of electrical impulses throughout the ventricles. The former is defined as the distance between the Q-wave of the ECG signal and the peak of the T-wave, whereas the latter is defined as the time difference between the S-wave and the Q-wave. Basic statistical characteristics of QT intervals and QRS widths are considered in the final set of features.

In order to detect noisy signals, the normalized signal powers at very low frequencies $[0.005, 0.05]$ Hz, the power within $[0.05, 50]$ Hz, as well as the normalized power at higher frequencies $[50, 150]$ Hz are used. These frequency-domain features have been extracted from raw ECG signals.

Additional Features: Additional features are only defined for random forest classifier for binary decision making, which is explained in Subsection 2.4.3. As many different arrhythmias exhibit RR irregularities, we consider the percentage of times that the difference between three consecutive HR values exceeds 5 bpm, as well as 10 bpm. Similarly, the same set of features is extracted for five consecutive HR values. Additionally, the number of zero-crossings of the parts that correspond to the P-wave and T-wave are also taken into consideration.

2.4.3 Hierarchical Classifier

After performing feature extraction, two different classifiers are considered: a multi-class classifier based on error-correcting output codes (Dietterich and Bakiri, 1994), and a random forest classifier for binary decision making (Pal, 2005), as shown in Fig. 2.7.

In order to make sure that the extracted features are on a similar scale, before running any of these classifiers, each feature is normalized by subtracting its mean value and dividing it by its standard deviation.

Multiclass Classification (ECOC): Multiclass classification paradigm based on ECOC is used to classify instances into more than two classes. This paradigm assigns a unique binary string of length n to each class. These binary strings are known as codewords (Dietterich and Bakiri, 1994). Binary representation for each of the classes results in a coding matrix $m \times n$, where m represents several classes in a classification problem. One classifier is trained for each bit position in a coding matrix. At the test time, each of these n classifiers are evaluated to generate an n-bit string b. This string is further compared to each of the m coding words, and the new test example is assigned to the class whose codeword is closest in the sense of Hamming distance to the generated bit string b (Escalera et al., 2009). The list of features used for this classifier is detailed in Table 2.2.

Random Forest: As shown in Fig. 2.7, a random forest classifier for binary decision making is used in case of getting undefined rhythm (UndR) at the output of the ECOC classifier.

Random forest is an ensemble of decision trees that are combined to classify a sample data by aggregating decisions of all individual trees. This aggregation of decisions of all trees in the forest reduces the variance of the prediction, resulting in a low-variance model and a robust outcome (Liaw and Wiener, 2002). Each decision tree in the forest is constructed using a different bootstrap sample of data. In particular, if our training set has M rows in the feature matrix, a bootstrap sample of data of size M is constructed by randomly picking one of the M rows of the dataset with replacement. For each bootstrap sample, an unpruned tree (fully grown) is grown. At each node, a subset of features is randomly selected and the best split within this subset is chosen. To classify a new sample, each decision tree gives a classification decision. The forest chooses the classification decision that has the most votes among the other trees in the forest.

In this work, random forest classifier uses the additional features explained in Section 2.4.2 and a subset of features explained in Subsection 2.4.2. Specifically, the P-wave features obtained from matrices $\mathbf{P}$, $\mathbf{P^{(1)}}$, $\mathbf{P^{(2)}}$, $\mathbf{P^{(3)}}$ are not considered, as these features are mostly used for AF detection. The detailed list of features used for random forest classification is given in Table 2.3.

HR: BSCH of HR	HR$^{(1)}$: BSCH of the first derivative of HR
HR$^{(2)}$: BSCH of the second derivative of HR	HR$^{(3)}$: BSCH of the third derivative of HR
bradycardia_feature: % of HR values below 40 bpm	feature_extreme_bradycardia = 1 if the value of HR falls below 40 bpm for any five consecutive beats, otherwise 0
tachycardia_feature: % of HR values that are above 140 bpm	feature_extreme_tachycardia = 1 if the value of HR is above 140 bpm for any 17 consecutive beats, otherwise 0
F_{limit_1} = 1 if the value of the average HR is above 100, otherwise 0	F_{limit_2} = 1 if the value of the average HR is above 130, otherwise 0
F_{limit_3} = 1 if the value of the average HR is below 46, otherwise 0	$F_{p_{\text{max}}}$: BSCH of vector $\mathbf{p_{max}}$
$F_{p_{\text{min}}}$: BSCH of $\mathbf{p_{min}}$	$F_{p_{\text{mean}}}$: BSCH of $\mathbf{p_{mean}}$
$F_{p_{\text{median}}}$: BSCH of $\mathbf{p_{median}}$	$F_{p_{\text{std}}}$: BSCH of $\mathbf{p_{std}}$
$F^{(1)}_{p_{\text{max}}}$: BSCH of $\mathbf{p^{(1)}_{max}}$	$F^{(1)}_{p_{\text{min}}}$: BSCH of vector $\mathbf{p^{(1)}_{min}}$
$F^{(1)}_{p_{\text{mean}}}$: BSCH of $\mathbf{p^{(1)}_{mean}}$	$F^{(1)}_{p_{\text{median}}}$: BSCH of $\mathbf{p^{(1)}_{median}}$
$F^{(1)}_{p_{\text{std}}}$: BSCH of $\mathbf{p^{(1)}_{std}}$	$F^{(2)}_{p_{\text{max}}}$: BSCH of $\mathbf{p^{(2)}_{max}}$
$F^{(2)}_{p_{\text{min}}}$: BSCH of $\mathbf{p^{(2)}_{min}}$	$F^{(2)}_{p_{\text{mean}}}$: BSCH of $\mathbf{p^{(1)}_{mean}}$
$F^{(2)}_{p_{\text{median}}}$: BSCH of $\mathbf{p^{(2)}_{median}}$	$F^{(2)}_{p_{\text{std}}}$: BSCH of $\mathbf{p^{(1)}_{std}}$
$F^{(3)}_{p_{\text{max}}}$: BSCH of $\mathbf{p^{(3)}_{max}}$	$F^{(3)}_{p_{\text{min}}}$: BSCH of $\mathbf{p^{(3)}_{min}}$
$F^{(3)}_{p_{\text{mean}}}$: BSCH of $\mathbf{p^{(3)}_{mean}}$	$F^{(3)}_{p_{\text{median}}}$: BSCH of $\mathbf{p^{(3)}_{median}}$
$F^{(3)}_{p_{\text{std}}}$: BSCH of $\mathbf{p^{(3)}_{std}}$	$F_{p_{\text{norm}}}$: BSCH of $\mathbf{p_{norm}}$
$F^{(1)}_{p_{\text{norm}}}$: BSCH of $\mathbf{p^{(1)}_{norm}}$	$F^{(2)}_{p_{\text{norm}}}$: BSCH of $\mathbf{p^{(2)}_{norm}}$
$F^{(3)}_{p_{\text{norm}}}$: BSCH of $\mathbf{p^{(3)}_{norm}}$	f_p
P_{s_p}: Normalized power of s_p in [0, 30] Hz	E_{s_p}: Shannon entropy of s_p
$F^{(1)}_{s_p}$: BSCH of the first derivative of s_p	$F^{(2)}_{s_p}$: BSCH of the second derivative of s_p
$F^{(3)}_{s_p}$: BSCH of the third derivative of s_p	NEG_p: % of negative P-waves
$P_{s_{t_1}}$: Normalized power of s_t in [0, 5] Hz	$P_{s_{t_2}}$: Normalized power of s_t in [5, 30] Hz
E_{s_t}: Shannon entropy of signal s_t	PR: BSCH of the PR intervals
STD_{PR}: Ratio between standard deviations of the PR and RR intervals	MEAN_{PP}: Ratio between mean values of the PP and RR intervals
STD_{PP}: Ratio between standard deviations of the PP and RR intervals	QT: BSCH of the QT intervals
QRS: BSCH of QRS widths	P_{low}: Normalized ECG signal power within $[0.005, 0.05]$Hz
P_{ECG}: Normalized ECG signal power within $[0.05, 50]$Hz	P_{high} Normalized ECG signal power within $[50, 150]$Hz

Table 2.2: List of features used for ECOC. BSCH represents the basic statistical signal characteristics defined in Subsection 2.4.2

HR: BSCH of HR	$HR^{(1)}$: BSCH of the first derivative of HR
$HR^{(2)}$: BSCH of the second derivative of HR	$HR^{(3)}$: BSCH of the third derivative of HR
bradycardia_feature: % of HR values below 40 bpm	feature_extreme_bradycardia = 1 if the value of HR falls below 40 bpm for any five consecutive beats, otherwise 0
tachycardia_feature: % of HR values above 140 bpm	feature_extreme_tachycardia = 1 if the value of HR is above 140 bpm for any 17 consecutive beats, otherwise 0
$F_{limit_1} = 1$ if the value of the average HR is above 100, otherwise 0	$F_{limit_2} = 1$ if the value of the average HR is above 130, otherwise 0
$F_{limit_3} = 1$ if the value of the average HR is below 46, otherwise 0	f_p
$HR_{3,5}$: % of times the difference between three consecutive HR values exceeds 5 bpm	$HR_{3,10}$: % of times the difference between three consecutive HR values exceeds 10 bpm
$HR_{5,5}$: % of times the difference between five consecutive HR values exceeds 5 bpm	$HR_{5,10}$: % of times the difference between five consecutive HR values exceeds 10 bpm
N_T: Number of zero-crossings of the T-waves	N_P: Number of zero-crossings of the P-waves
P_{s_p}: Normalized power of s_p in the frequency range [0, 30] Hz	E_{s_p}: Shannon entropy of s_p
$F_{s_p}^{(1)}$: BSCH of the first derivative of s_p	$F_{s_p}^{(2)}$: BSCH of the second derivative of s_p
$F_{s_p}^{(3)}$: BSCH of the third derivative of s_p	NEG_p: % of negative P-waves
$P_{s_{t_1}}$: Normalized power of s_t in [0, 5] Hz	$P_{s_{t_2}}$: Normalized power of s_t in [5, 30] Hz
E_{s_t}: Shannon entropy of s_t	PR: BSCH of the PR intervals
STD_{PR}: Ratio between standard deviations of the PR and RR intervals	$MEAN_{PP}$: Ratio between mean values of the PP and RR intervals
STD_{PP}: Ratio between standard deviations of the PP and RR intervals	QT: BSCH of the QT intervals
QRS: BSCH of QRS widths	P_{low}: Normalized raw ECG signal power within $[0.005, 0.05]$Hz
P_{ECG}: Normalized raw ECG signal power within $[0.05, 50]$Hz	P_{high} Normalized raw ECG signal power within $[50, 150]$Hz

Table 2.3: List of features used for random forest classifier. BSCH represents the basic statistical signal characteristics defined in Subsection 2.4.2

.

2.4.4 Experimental Setup and Results

In this section, the cross-validation scheme for training the classifiers, the final classifiers' parameters, along with the results are explained. As previously mentioned, PhysioNet/Computing in Cardiology Challenge 2017 database is used to validate the proposed classification method for heart rhythm detection (Clifford et al., 2017). This database consists of 5050 NSR records, 2456 records that belong to OthR records, 738 AF records, and 284 noisy records.

Cross-Validation: In order to avoid the overfitting problem, the entire database is split into the training and the test set. The training set contains 80% of randomly selected records of each class. The remaining 20% percent of each class is used in the test set. The training set is further divided into two different sets, set I and set II. Set I contains 70% randomly selected training records, and the remaining 30% is used for set II. The split of training data into set I and set II is repeated five times in order to assess the robustness of the results. The F_1 score given in Eq. (2.2) is used, as a metric for classifier performance evaluation. The results obtained on set II for five different data splits are tabulated in Table 2.4:

F_1(%)	NSR	AF	OthR	Final score
Fold_1	89.89	79.13	70.76	79.93
Fold_2	88.96	76.61	68.82	78.13
Fold_3	89.31	77.56	70.85	79.24
Fold_4	88.83	77.46	70.04	78.78
Fold_5	88.70	75.50	70.71	78.30

Table 2.4: Results of five-fold cross-validation results obtained on set II for NSR, AF, and OthR.

The multiclass classifier is further trained using the entire training test. After running this classifier on the test set, the obtained F_1 scores for NSR, AF, and OthR are $89.73\%, 78.83\%, 73.85\%$, respectively. By examining the misclassified examples, I noticed that 43% of misclassified examples consisted of OthR signals that are classified as NSR, whereas 23% of misclassified samples consisted of NSR that are classified as OthR. This is the main reason for designing a random forest classifier for binary decision making between OthR and NSR ECG signals. Due to the fact that classes OthR and NSR are not balanced, the geometrical mean of sensitivity and specificity ($\mathsf{G}_{\mathsf{mean}}$) is used to inspect the performance of the random forest classifier.

These metrics are defined as follows:

$$\mathsf{sensitivity} = \frac{\mathsf{tp}}{\mathsf{tp}+\mathsf{fn}}, \tag{2.4}$$

$$\mathsf{specificity} = \frac{\mathsf{tn}}{\mathsf{tn}+\mathsf{fp}}, \tag{2.5}$$

$$\mathsf{G}_{\mathsf{mean}} = \sqrt{\mathsf{sensitivity}\cdot\mathsf{specificity}}, \tag{2.6}$$

where tp, tn, fp, fn represent the number of true positive, true negative, false positive, and false negative, respectively. Similarly to F_1 measure, $\mathsf{G}_{\mathsf{mean}}$ also takes into account the class imbalance. The obtained results for 5-fold cross-validation scheme are the following ones: $\mathsf{G}_{\mathsf{mean}} = \{81.91, 82.08, 82.22, 82.58, 82\}\%$. In order to minimize 5-fold cross-validation loss, the hyperparameters of ECOC classifier are optimized, resulting in a coding scheme that uses $n = 25$ bits for a binary representation of each of the four classes. Furthermore, classifiers that are trained for each bit are LogitBoost ensemble of classification trees with surrogate splits and 100 weak learners. Random forest classifiers for binary decision making uses 400 weak learners. The last step consists of training both multiclass and binary classifier on the entire available data (on both training and test set). The results obtained on the hidden test set of challenge are the following ones: $\mathsf{F}_{\mathsf{NSR}} = 90.31\%, \mathsf{F}_{\mathsf{AF}} = 78.95\%, \mathsf{F}_{\mathsf{OthR}} = 70.76\%, \mathsf{F}_{\mathsf{FINAL}} = 80\%$, whereas the winning algorithms in the 2017 PhysioNet/CinC Challenge achieved an $\mathsf{F}_{\mathsf{FINAL}}$ score of 83%.

One of the main problems of the 2017 PhysioNet/CinC Challenge was data labeling. Namely, due to the high degree of disagreement between expert clinicians who labeled the data, both the training and the hidden set were re-labelled (Clifford et al., 2017). Apart from label inconsistency, the proposed heart-rate classification method could be further improved. Firstly, the presented method does not take into account the lead inversion. Many signals in the training set were inverted as the user was not required to hold the acquisition device in any particular position (Clifford et al., 2017). The lack of lead inversion correction has an impact on the training process of both classifiers due to the difficulty of identifying the important segments of the ECG trace. Moreover, no feature selection method was used to select the relevant features for each of the classes.

2.5 Myocardial Infarction

MI, also known as a heart attack, remains one of the leading life-threatening conditions nowadays. MI is a very serious cardiac disease affecting people all around the world. Based on the latest statistics, in the USA alone, every 40 seconds someone gets a heart attack (HeartFacts, 2019). The economic burden of US hospitalizations due to MI in 2010 was already estimated at over 45 billion US dollars (Reed et al., 2017).

MI occurs due to fatty deposits called plaques that gradually form on the inner walls of coronary arteries. Due to smoking, hypertension, diabetes as well as family medical history, these plaques can build up significantly throughout the years. Then, a sudden rupture of these plaques at an unexpected moment triggers a blood clot to form. The blood clot can completely block an artery impeding the normal circulation of the blood. The muscle cells of the part of the heart that was getting supplied by the blocked artery become starved for oxygen and nutrients. Due to this lack of oxygen and nutrients, these cells begin dying.

The histological death of these starved cells begins in as little as 20 minutes after the artery occlusion (Thygesen et al., 2012), (Camm et al., 2009). As soon as one of the coronary arteries becomes blocked, the person must receive treatment in less than 90 minutes. The earliest possible heart attack detection minimizes the number of dead cells. The mortality rate drastically increases by 41–62% if the delay between the hospital arrival and the performance of the treatment is longer than 2 hours (Cannon et al., 2000). The prolongation of this detection period results in irreversible consequences of the affected myocardial cells (heart attack). These consequences can be observed based on the altered ECG beat morphology, as shown in Fig. 2.10. This altered ECG beat morphology is often reflected onto the ST segment abnormality (elevation or depression) and is the same across all ECG beats. Additionally, patients who have suffered a heart attack remain at an increased risk of recurrent heart attacks. The annual death rate of survivors is six times higher than in people who have not had a heart attack (WHO, 2013).

In order to prevent potential recurrent heart attacks, adequate care should be provided to these patients. Thus, real-time patient monitoring is performed in hospitals through common tests for heart attack diagnosis. These tests include ECG and echocardiogram. However, all these tests are usually performed by bulky medical equipment. The lack of portability of this equipment, as well as its high energy consumption, make it unsuitable and uncomfortable for ambulatory monitoring.

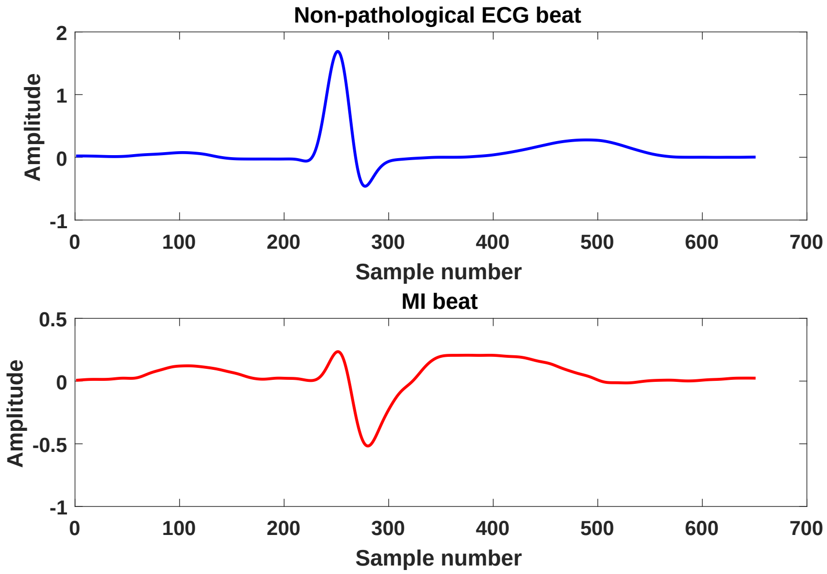

Figure 2.10: An ECG beat from a healthy subject versus an ECG beat from a person with MI. MI beats have an ST elevation, i.e., the ST segment is abnormally high above the baseline.

Wearable devices represent a suitable solution to address the aforementioned constraints of medical equipment for real-time patient monitoring. These low-cost devices are portable and can be used autonomously by patients (Riazul Islam et al., 2015). Moreover, they enable the continuous remote patient monitoring during daily life by collecting patient's data and providing it to healthcare professionals. Hence, they can reduce the possibility of significant worsening of the patient's condition by detecting early cardiac irregularities. This is done by sending patient data acquired from wearable devices using Bluetooth to a mobile phone, which is later on sent to physicians through the cloud. However, sending data using Bluetooth consumes a lot of energy, which drains the battery of wearable devices (Rincón et al., 2011), (Mamaghanian et al., 2011). Furthermore, not only is sending data to the cloud energy-hungry (Fan Zhang et al., 2012), but its latency and reliable communication are also affected by the connection quality (Tang et al., 2017). Nonetheless, many commercial wearable devices have stringent latency requirements. Thus, as constant good-quality network connections are only available at limited locations and a high cost, and that even with good network connectivity the required latency often cannot be acquired (Klas, 2017), streaming data to the cloud is not suitable for real-time patient monitoring. Therefore, in order to overcome the aforementioned problems, the latest trend is to use smart wearable devices, or so called edge computing techniques (Ananthanarayanan et al., 2017), in which the entire processing is performed on the on-board microcontroller of the wearable device.

Nowadays, the algorithms running on smart wearables are mostly based on simple machine learning techniques (Patel et al., 2009), (Apiletti et al., 2009). However, the major challenge of highly-accurate machine learning algorithms is their high computational complexity. Hence, these algorithms cannot be implemented on wearable devices for real-time monitoring. Therefore, these algorithms need to be highly optimized, which promotes the need for a paradigm shift in the classifier design. In this context, the event-driven computing approach offers a promising solution to reduce the computational complexity of embedded machine learning algorithms. Moreover, it can substantially lower the energy consumption of smart wearable devices.

2.6 Previous Work on Detection of Myocardial Infarction

Several studies have been conducted concerning the detection of MI using various classification techniques. For instance, in (Reddy et al., 1992), the authors use QRS measurements obtained from different ECG leads as inputs to the neural network to detect MI. Another similar approach to MI detection based on the use of a fuzzy multi-layer perception network trained on a set of morphological features is presented (Bozzola et al., 1996). These features include the amplitude and duration of the QRS complex, as well as the amplitude of the T wave and Q/R ratio. Then, in (Acharya et al., 2016), the authors report a high accuracy in classifying normal and MI ECG beats using the k-nearest neighbors classifier. However, none of these studies are performed on existing wearable devices, taking into consideration the stringent energy and memory constraints of these devices.

The need to reduce the energy consumption of wearable devices has given rise to a plethora of studies. In (Braojos et al., 2014), a real-time classification scheme for automatic detection of abnormal heartbeats targeting embedded and resource-constrained wearables has been proposed. This scheme also incorporates an advanced digital signal processing block that is activated just when abnormal beats are detected, which considerably decreases the computational requirements and the energy consumption. First, from a medical reliability point of view, the authors do not investigate the confidence level of the obtained results, which is a key parameter in medical applications. Secondly, from an energy-efficiency point of view, their work focuses on a context where pathological heartbeats occur less frequently than normal ones. Therefore, in case of many pathological heartbeats happening one after another, the advanced digital signal processing block will be successively invoked, which will

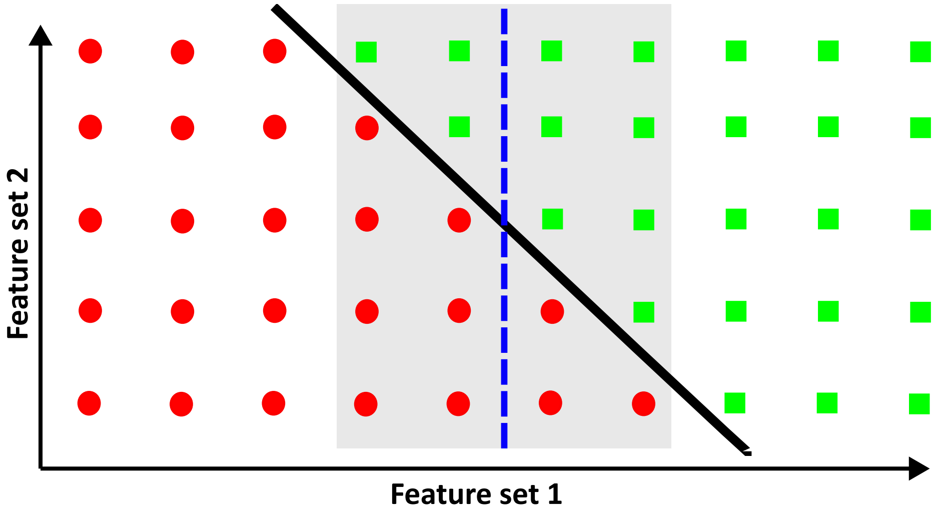

Figure 2.11: Motivational example.

increase the computational complexity and energy consumption.

As one of the contributions to this thesis, a new real-time event-driven classification technique for early detection and prevention of MI through means of ultra-low energy wearable systems is proposed. The proposed classification technique reduces the energy consumption of wearable devices, while maintaining a high classification accuracy. This technique is validated on the case of MI based on the set of features used in (Acharya et al., 2016). The main target of this technique is the use of ultra-low energy wearable devices, thus it is not strictly limited to the problem of early detection and prevention of MI.

The remainder of this chapter is organized as follows. The motivation behind the proposed event-driven technique is described in Section 2.7. Then, the proposed real-time event-driven classifier is explained in Section 2.8. The analysis of the computational complexity, battery life, and energy efficiency of the proposed approach is described in Section 2.9. The experimental setup used for validating the proposed approach in the case of MI is presented in Section 2.10, whereas the experimental results are given in Section 2.11.

2.7 Motivational Example

In this section, the main idea of the proposed real-time event-driven classification technique is illustrated using a small example. Without loss of generality, and for the simplicity of the presentation, two sets of features for the binary classification problem are considered, as shown in Fig. 2.11. We define the computational complexity of an algorithm as the maximum amount of time it takes to run the algorithm for inputs of a given size (Sipser, 2006). Supposing that each elementary operation within the algorithm takes a fixed amount of time to perform, the computational complexity is commonly estimated by counting the number of elementary operations performed by the algorithm (Sipser, 2006).

Let us suppose that the computational complexity of the feature set that is along the vertical axis (feature set 2) is higher than the computational complexity of the one along the horizontal axis (feature set 1). For instance, feature set 1 can contain time-domain features of the dataset, whereas feature set 2 can contain frequency-domain features. Time-domain features have a complexity order of $\mathcal{O}(n)$, where n is the signal's length, whereas the frequency-domain features have a complexity order of $\mathcal{O}(n \log_2 n)$, as the calculation of frequency-domain features requires additional signal transformations, such as, the Fourier transform.

In this example, 25 circle-shaped samples of class 1 and another 25 square-shaped samples of class 2 are considered. For instance, in the case of MI, circle-shaped samples belong to people suffering from MI, whereas square-shaped ones belong to healthy subjects. Let us suppose that $n = 2^{10}$. Depending on the confidence level, three different linear classifiers can be built.

The first classifier is shown by the dashed line in Fig. 2.11. This classifier uses only feature set 1 to separate two classes. As it can be observed in Fig. 2.11, if this classifier is used, some samples within the shaded gray area will be misclassified. The accuracy and the expected computational complexity of this classifier are: $\textbf{Accuracy}_{\text{dashed}} = 88\%$, $\textbf{Complexity}_{\text{dashed}} = n = 2^{10}$. Hence, the expected computational complexity of this classifier is low, whereas its classification accuracy is lower than that of the optimal solution.

Another alternative is to use both feature sets. This is done using the second classifier shown by the solid line in Fig. 2.11. The accuracy and the expected computational complexity of this classifier are $\textbf{Accuracy}_{\text{solid}} = 100\%$, $\textbf{Complexity}_{\text{solid}} = n \log_2 n = 10240$, respectively. This classifier outperforms the first classifier in terms of classification accuracy, but it is ten times more computationally complex.

Finally, the hierarchical classifier combines the benefits of the two previous classifiers. Based on the desired confidence level, either the classifier that uses feature set 1 (i.e., the dashed line, the first classifier) or the one that uses both sets of features (i.e., the solid line, the second one) is used. The desired confidence level represents the degree to which we rely on the decision of the first classifier. The main goal of this scheme is to reduce the classifier complexity in terms of the number of features that will be used for the final classification, while maintaining a high classification accuracy. As shown in Fig. 2.11, the first classifier cannot make confident decisions for samples that happen to be in the shaded gray area. For these samples, the second classifier, i.e., the classifier that uses all available features should be used to target medical applications that truly require a high confidence level. Hence, once the region in which the first classifier does not provide high confidence results is identified, the next step is to check for each testing example if it falls into this shaded area and, if so, to use the second classifier. Otherwise, we use the first classifier, i.e., the classifier with a reduced number of features. For this particular example, let us suppose that the region in which the first classifier does not provide high confidence results is found, shown in Fig. 2.11. If the hierarchical classifier is used, the classification accuracy is $\textbf{Accuracy}_{\text{hierarchical}} = 100\%$, whereas its expected classification complexity is calculated as:

$$E(C) = \tfrac{30}{50} \cdot n + \tfrac{20}{50} \cdot n \cdot \log_2 n.$$

For $n = 2^{10}$, the expected classification complexity is $E_{\text{hierarchical}}(C) = 4710.4$, whereas with the classical approach that uses all available features (shown by the solid line in Fig. 2.11) we obtain $E_{\text{solid}}(C) = \tfrac{50}{50} \cdot n \cdot \log_2 n = 10240$. Hence, for this motivational example and $n = 2^{10}$, the proposed approach reduces the classification complexity by a factor of 2.

In summary, for this motivational example shown, three different classifiers have been presented. The first classifier (the dashed line) has a low computational complexity, but its classification accuracy is much lower than the performance of the second one (the solid line). On the other hand, the second classifier has a high classification accuracy, but it is significantly more complex than the first one. Thus, the proposed hierarchical classifier combines the two previous classifiers, such that we get a classifier that has a high classification accuracy and a low computational complexity.

2.8 Real-Time Event-Driven Classification Technique

In this section, a real-time event-driven classification technique for early detection and prevention of MI based on random forest (Díaz-Uriarte and Alvarez de Andrés, 2006) is proposed. This real-time event-driven technique incorporates $m+1$ different classification levels. The number of features at level i is equal to $i \cdot K$, where the parameter K is used by the designer to make a trade-off between the performance of the system, in terms of classification accuracy and energy efficiency, and the complexity of design space exploration.

In an event-driven computing paradigm, the execution of a particular action depends on the occurrence of predefined trigger events (Årzén, 1999). Therefore, the event-driven schemes perform the most computationally expensive processing only in case a particular trigger event occurs, which reduces the computational complexity and, therefore, enhances the battery life of wearable devices. In our case, based on the required confidence level, we choose the classification level that is used for classifying a sample data. Hence, the event that triggers the use of more computationally complex classifiers is the insufficient level of decision confidence of classifiers at previous levels. The overall flow of the proposed approach is shown in Fig. 2.12. The proposed classification technique consists of two main phases: the offline phase that is explained in Section 2.8.1, and the online phase explained in Section 2.8.2.

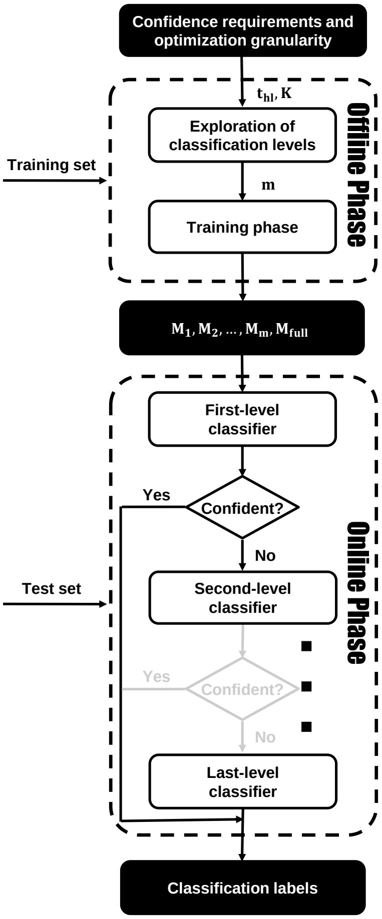
Confidence requirements and optimization granularity
t_{hl}, K
Exploration of classification levels
m
Training phase
Offline Phase
Training set
$M_1, M_2, \ldots, M_m, M_{full}$
First-level classifier
Yes
Confident?
No
Second-level classifier
Yes
Confident?
No
Last-level classifier
Online Phase
Test set
Classification labels

Figure 2.12: Diagram of the proposed event-driven classification technique that consists of $m+1$ classification levels. Each classification level i contains $i \cdot K$ features, where $i = 1, \ldots, m$, whereas the last classification level contains all available features. Parameter K is used by the designer to make a trade-off between the classification accuracy performance of the system, its energy efficiency, and the complexity of design space exploration.

2.8.1 Offline Phase of Our Real-Time Event-Driven Classification Technique

In an event-driven classification scheme very often we do not need to compute all available features to make confident decisions, as often they can be made based on only a few features. Reducing the number of features that we need to compute for making confident decisions, in turn, reduces the energy consumption of our system. Therefore, the basic idea is to use a hierarchical classifier, where all features are computed only when needed.

Consequently, in the proposed technique the classifiers at lower levels consider a limited number of features and, therefore, are computationally efficient, but do not provide as high classification accuracy as those at higher levels. On the other hand, classifiers at higher levels can provide a high classification accuracy, but are computationally complex. In this real-time event-driven classification technique, classifiers at higher levels are invoked only if classifiers at lower levels are unable to classify a sample data with the required level of confidence.

The inputs of the proposed hierarchical classification techniques are:

- input feature matrix, denoted by $\mathbf{X}$, where the overall number of available features is denoted by n,
- class labels for each training example, denoted by $\mathbf{y}$.

The input feature matrix contains features for both classes. Each column of the input matrix corresponds to a feature, whereas each row corresponds to an observation. The main goal is to design a high-accuracy hierarchical classifier satisfying the battery life requirements, in case such classifier can be designed.

First, the features from the input signals are extracted. Then, these features are sorted based on their relevance by using the infinite latent feature selection algorithm to find the most informative ones (Roffo et al., 2017). This algorithm uses a robust probabilistic latent graph-based feature selection algorithm that performs feature ranking by considering all possible subsets of features. Each subset of features is considered as a path connecting set of nodes of a weighted graph, where each node represents one feature and each weight indicates the feature importance. The weighted graph is used to perform the ranking step providing a score of importance for each feature as a function of the importance of its neighbors. However, the proposed real-time event-driven approach is not restricted to this feature selection method.

The number of classification levels is found based on Algorithm 1. Parameter $T_{lifetime}$ refers to the battery life of a wearable system, whereas T_{min} refers to the minimum expected battery life of the wearable device. The condition that uses $T_{lifetime}$ in Algorithm 1 is thoroughly explained in Section 2.9. Each classification level i contains features from the previous classification level, along with additional features that belong to level i. The last classification level contains all available features. In order to make sure that all features are on a similar scale, before training any of the classifiers, each feature is normalized by subtracting its mean value and dividing it by its standard deviation. The mean value ($\mathbf{mean_v}$) and the standard deviation of each feature ($\mathbf{sig_v}$) are stored. Next, we apply the random forest algorithm explained in

Algorithm 1 Exploration of classification levels

```
function TRAINING($t_{hl}, K, T_{min}, \mathbf{X}, \mathbf{y}$)
    $m = 1$;
    $Calculate\ T_{lifetime}(m)\ based\ on\ Eq.$ (2.14)
    while ($T_{lifetime}(m) < T_{min}$) do
        $m = m + 1$
        $Calculate\ T_{lifetime}(m)\ based\ on\ Eq.$ (2.14)
    end while
    $Sort\ features$
    $Shuffle\ the\ data$
    $S_1 \leftarrow 0.8 \cdot length(data)$
    $S_2 \leftarrow 0.2 \cdot length(data)$
    $\mathbf{mean_v}, \mathbf{sig_v}, \overline{S_1} \leftarrow normalization(S_1)$
    for $j = 1$ to $m$ do
        $M_j \leftarrow Train(\overline{S_1}, K, number_{levels} = j)$
    end for
    $M_{full} \leftarrow Train(all\ features)$
    $\overline{S_2} \leftarrow normalization(S_2)\ based\ on$ $\mathbf{mean_v}, \mathbf{sig_v}$
    $Test(\overline{S_2}, t_{hl}, K, M_1, \cdots, M_m, M_{full})$
    $Calculate\ Gmean\ on\ S_2$
end function
```

Section 2.4.3 based on the confidence-related decision making process for training each classification level. In this work, the following approach for aggregating decisions from individual trees has been adopted. Namely, we define the parameter t_h that represents a percentage of mutually agreed trees. This parameter is used for inspecting the confidence level of the obtained results. Comparing the value of this parameter to the value of the decision-making threshold set in the design process t_{hl}, we decide which classifier is invoked. Random forest classifiers at each classification level use 100 weak learners.

The input feature matrix $\mathbf{X}$ and the class labels for every training example $\mathbf{y}$ are used in the offline phase, as shown in Fig. 2.12. The outputs of this phase are the number of classification levels m, as well as the $m+1$ classifiers, namely $M_1, \ldots, M_m, M_{full}$. The last-level classifier M_{full} uses all of the available features.

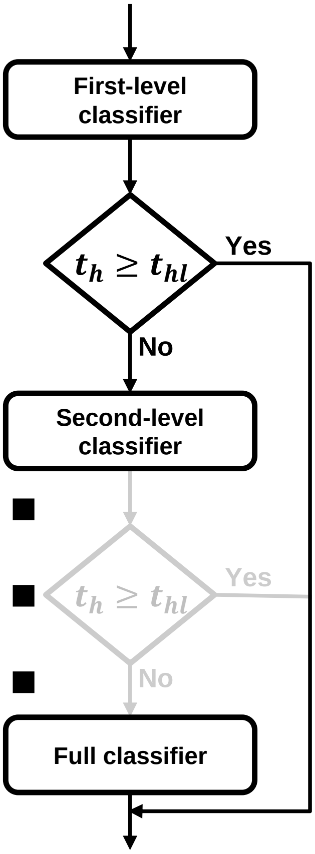
First-level classifier
$t_h \geq t_{hl}$
Yes
No
Second-level classifier
$t_h \geq t_{hl}$
Yes
No
Full classifier

Figure 2.13: Flowchart of the online phase of the proposed event-driven classification technique

2.8.2 Online Phase of Our Real-Time Event-Driven Classification Technique

The overall flow of the online phase of the proposed hierarchical classification technique is shown in Fig. 2.13. Before applying any of the classifiers, we first normalize a new testing example. When classifying it, we first calculate features from the first-level classifier. We inspect a decision of each tree and calculate the parameter t_h in the following way. Assuming that the number of trees in the forest is N_T, we define functions $F(t_i)$ and $G(t_i)$ for each decision tree t_i within the forest, as follows:

$$F(t_i) = \begin{cases} 1, & \text{if decision}(\mathrm{t_i}) = +1 \\ 0, & otherwise \end{cases}$$

$$G(t_i) = \begin{cases} 1, & \text{if decision}(\mathrm{t_i}) = -1 \\ 0, & otherwise. \end{cases}$$

Labels $\mathrm{t_i}$ = +1 and $\mathrm{t_i}$ = -1 are assigned to different classes. Feature vectors that correspond to non-MI ECG beats are labelled as -1, whereas those extracted from MI ECG beats are labelled as 1. The value of t_h is calculated as follows:

$$t_h = \frac{\max(\sum_{i=1}^{N_T} F(t_i), \sum_{i=1}^{N_T} G(t_i))}{N_T}.$$

If the first-level classifier cannot make a confident decision, i.e., if the value of the parameter t_h is below the decision-making threshold t_{hl}, we keep the first k_1 features in the feature set, and we calculate the rest of $k_2 - k_1$ features of the second-level classifier. This process is repeated until one of the classifiers matches the criteria for making a confident decision. As previously mentioned, the last classification level contains all available features. Therefore, in case none of previous m classifiers can make a confident decision, the full classifier is invoked.

2.9 Analysis of the Proposed Real-Time Event-Driven Classification Technique

In this section, the complexity, battery life, and energy efficiency of the proposed approach are analyzed. In Subsection 2.9.1, the expected complexity of the proposed real-time event-driven technique is estimated, whereas its energy consumption is estimated in Subsection 2.9.2.

2.9.1 Complexity of the Proposed Real-Time Event-Driven Classification Technique

For the sake of simplicity, in this discussion we focus on a two-level classifier in which the first-level considers $k_1 < n$ features, while the second-level considers all of n available features, including k_1 features from the first-level classifier. Firstly, the first-level classifier is invoked to classify a new data sample by calculating its k_1 features.

In case the first-level classifier is unable to classify a sample data with the required level of confidence, the second-level classifier is invoked. In this case, we keep k_1 calculated features and we calculate the other $n - k_1$ features. Therefore, the expected computational complexity (the mathematical expectation denoted by $\mathbb{E}(\cdot)$) of this two-level classifier $\mathbb{E}(C_2)$ is computed as follows:

$$\mathbb{E}(C_2) = \sum_{i=1}^{k_1} c_i + (1 - p_1) \cdot \sum_{i=k_1+1}^{n} c_i, \tag{2.7}$$

where p_1 is defined as the probability that the first-level classifier is sufficient for making confident decisions, whereas c_i represents the computational complexity of feature i. By reorganizing addends in Eq. (2.7), we derive the following equation:

$$\mathbb{E}(C_2) = p_1 \cdot \sum_{i=1}^{k_1} c_i + (1 - p_1) \cdot \sum_{i=1}^{n} c_i, \tag{2.8}$$

where $\sum_{i=1}^{k_1} c_i$ represents the complexity of the first-level classifier and $\sum_{i=1}^{n} c_i$ that of the second-level (which uses all available features). The first-level classifier is invoked with a probability of p_1. If the first-level classifier fails to classify a new data sample with the required level of confidence, the second-level classifier is invoked with a probability of $1 - p_1$. Therefore, in Eq. (2.8), the complexity of the first-level classifier is multiplied by p_1, whereas the complexity of the second-level one is multiplied by $1 - p_1$. For $k_1 < n$, the following inequality holds:

$$p_1 \cdot \sum_{i=1}^{k_1} c_i + (1 - p_1) \cdot \sum_{i=1}^{n} c_i < \sum_{i=1}^{n} c_i, \tag{2.9}$$

which indicates that the overall computational complexity of the two-level classifier is always smaller than that of the second-level classifier (the classifier that uses all available features).

Let us now consider the case of a three-level classifier in which the first-level is comprised of k_1 features, the second-level includes $k_2 > k_1$ features (including k_1 features of the first-level classifier), and the third-level has all of n available features (including all of the features of the previous classifiers). First, we invoke the first-level classifier for classifying a new data sample. If the first-level classifier cannot classify a new data sample with the required level of confidence, we invoke the second-level classifier by calculating its remaining $k_2 - k_1$ features. In case neither the first-level nor the second-level classifier can classify a new data sample with the required confidence level, the third-level classifier is invoked. In this case, we keep k_2 features of the previous two classification levels and calculate the other $n - k_2$ features of the third-level classifier. Therefore, the expected computational complexity of the three-level classifier is computed as follows:

$$\mathbb{E}(C_3) = p_1 \cdot \sum_{i=1}^{k_1} c_i + (1 - p_1) \cdot \left(p_2 \cdot \sum_{i=1}^{k_2} c_i + (1 - p_2) \cdot \sum_{i=1}^{n} c_i \right).$$

For $k_2 < n$, the following inequality holds:

$$\mathbb{E}(C_3) < \mathbb{E}(C_2), \tag{2.10}$$

showing that the computational complexity of the third-level classifier is smaller than that of the second-level one. Taking into consideration both Eq. (2.9) and (2.10), for $k_1 < k_2 < n$ we have the following inequality:

$$\mathbb{E}(C_3) < \mathbb{E}(C_2) < \sum_{i=1}^{n} c_i, \tag{2.11}$$

which shows that the computational complexity decreases as the number of classification levels increases.

In the general case, considering that m represents the number of classification levels, k_i the number of features at level i, where $i = 1, \ldots, m$, $k_i = i \cdot K$, c_r the computational complexity of feature r, n the number of all available features, and p_i the probability that the classifier at level k_i is sufficient for making confident decisions, the expected computational complexity of our hierarchical classifier can be estimated as follows:

$$\mathbb{E}(C) = \left(\sum_{i=1}^{m} \prod_{j=1}^{i-1} (1 - p_j) \cdot p_i \cdot \sum_{r=1}^{k_i} c_r \right) + \prod_{j=1}^{m} (1 - p_j) \cdot \sum_{r=1}^{n} c_r, \tag{2.12}$$

where $k_1 < k_2 < \cdots < k_m < n$, and we have:

$$\sum_{i=1}^{m} \prod_{j=1}^{i-1} (1 - p_j) \cdot p_i + \prod_{j=1}^{m} (1 - p_j) = 1,$$

as the sums of computational complexities in Eq. (2.12) are multiplied by the product of probabilities, which must add up to 1.

2.9.2 Energy Consumption of our Real-Time Event-Driven Technique

Following the same analogy as in Subsection 2.9.1, the energy consumed by our hierarchical classifier is estimated as follows:

$$\mathbb{E}(E_C) = \left(\sum_{i=1}^{m} \prod_{j=1}^{i-1} (1 - p_j) \cdot p_i \cdot \sum_{r=1}^{k_i} E_r \right) + \prod_{j=1}^{m} (1 - p_j) \cdot \sum_{r=1}^{n} E_r,$$

where E_r represents the energy spent on the calculation of feature r, and we have:

$$\sum_{i=1}^{m} \prod_{j=1}^{i-1} (1 - p_j) \cdot p_i + \prod_{j=1}^{m} (1 - p_j) = 1.$$

In order to meet the battery life requirements, let us assume that the minimum required life of the wearable device is T_{min} hours. Considering the fact that we want the battery of the wearable device to last for at least T_{min} hours, we have the following set of inequalities:

$$T_{lifetime} \geq T_{min}, \tag{2.13}$$

$$\left[E_S \cdot (1 - d_C) + (E_C + E_P) \cdot d_C\right] \cdot T_{lifetime} = E_B, \tag{2.14}$$

where $T_{lifetime}$, E_S, d_C, E_C, E_P, E_B represent the battery life of the wearable system, the energy of the system consumed in the idle state, the CPU duty cycle, the energy spent by our hierarchical classifier (Eq. (2.12)), the energy spent on the preprocessing, and the battery storage according to its specifications, respectively. The energy spent on the calculation of each feature along with the energy spent in the preprocessing stage can be estimated on the wearable device. By combining inequality (2.13) and Eq. (2.14) we obtain the following inequality:

$$E_C \leq \frac{\left(\frac{E_B}{T_{min}} - E_S \cdot (1 - d_C)\right)}{d_C} - E_P. \tag{2.15}$$

2.10 Experimental Setup

In this section, the proposed technique is validated in terms of classification quality on a set of real-life ECG signals from a control group and from patients suffering from MI. In Subsection 2.10.1, we introduce the classification metrics used to evaluate the approach in terms of classification performance are introduced. Subsection 2.10.2 describes the real-life MI database used for the evaluation of the hierarchical technique along with the main preprocessing steps. The target platform used for deploying the real-time event-driven classification technique is described in Subsection 2.10.3.

2.10.1 Classification Performance Metrics

The simplest diagnostic test used in the medical community combines different metrics to classify patients into two different groups. The majority of medical studies often report two different metrics used to correctly assess the ability of diagnostic tests:

sensitivity and specificity, defined in Section 2.4.4. The classification is based on the presence or the absence of a particular symptom of interest (Altman and Bland, 1994). In order to capture the information obtained from both, sensitivity and specificity, the commonly used metric is their geometric mean ($\mathsf{G}_{\mathsf{mean}}$) (Fleming and Wallace, 1986), given in Eq. 2.6 in Section 2.4.4. The final classification performance is evaluated based on the test set. Each test sample is classified using the first classifier that can make a confident decision.

2.10.2 PTB Diagnostic ECG Database

The proposed technique is evaluated on the ECG signals from the Physionet (PTB Diagnostic ECG database) open access database (Goldberger et al., 2000). Signals from two groups of subjects are used for ECG beat classification: the control group and the group of patients. The control group contains ECG signals from 52 healthy subjects, whereas the group of patients consists of 52 patients who have already had a MI. All ECG signals are sampled at $f_s = 1000Hz$.

In order to perform ECG beat classification, we need to subtract ECG beats for each person in the database. Therefore, we first filter ECG signals to remove the baseline wander and high frequency noise. The baseline wander is removed through morphological filtering (Sun et al., 2002). Furthermore, we apply a zero-phase FIR band-pass filter of order 32 with cut-off frequencies $f_1 = 0.05Hz$ and $f_2 = 40Hz$ for high-frequency noise removal. Pan-Tompkin's algorithm is used for ECG R-peaks detection (Pan and Tompkins, 1985). Similar to the previous study in Acharya et al. (2016), the segmentation of ECG beats is performed by taking $f_s/4$ samples to the left and $f_s/2.5$ samples to the right of ECG R-peaks. Moreover, each individual ECG beat is decomposed using a discrete wavelet transform (DWT) down to level four with Daubechies 6 (db6) as a basis function, which results in four detail and four approximation DWT coefficients. The main features used in this classification technique are extracted from these eight coefficients based on the study in (Acharya et al., 2016). Namely, the normalized signal energy, the Higuchi's fractal dimension (Gómez et al., 2009), along with the following entropies: approximate, fuzzy, permutation, wavelet, Shannon, Renyi, and Tsallis (Acharya et al., 2015). These features all together represent the input feature matrix **X**. The features are sorted based on their relevance using the infinite latent feature selection algorithm (Roffo et al., 2017).

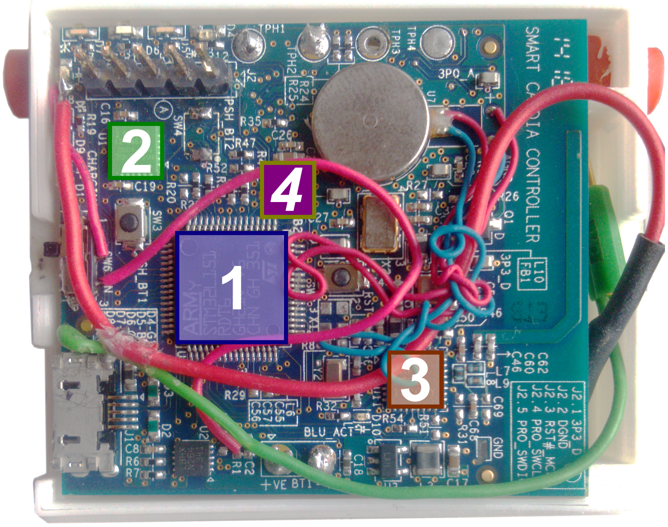

Figure 2.14: The SmartCardia INYU device prototype. Front: 1: STM32L151RDT6 (ARM Cortex-M3 MCU, 384 KB Flash, 48KB RAM), 2: MPU-6000 (6-axis I^2C motion sensor), 3: nRF8001 (Bluetooth low energy v4.0 radio). Back: 4: ADS1191 (Analog front-end for ECG applications).

2.10.3 Target Platform

The SmartCardia INYU wearable sensor (INYU, 2013) is considered as the target device in this work. In this device, a single-lead ECG signal is obtained through an ECG sensor with a 24-bit ADC (ADSECG, 2011) operating at a frequency that ranges from 125 Hz up to 16 KHz, with up to 16-bit resolution. This ADC is designed specifically for ultra-low power ECG applications. Then, this device features an ultra-low power 32-bit microcontroller STM32L151 (STM32, 2013) with an ARM® Cortex®–M3 on which the entire processing is performed with the possibility of operation at a maximum frequency of 32 MHz. The SmartCardia device also has a 48 KB RAM, 384 KB Flash, and a standard 710 mAh battery. The prototype of the SmartCardia INYU device is shown in Fig. 2.14. More detailed information about this device can be found in (Murali et al., 2015).

2.11 Experimental Results

2.11.1 Classification Quality Evaluation

The entire ECG database is split into training and test sets. The data of one patient is either put in the training set or in the test set. Therefore, all features extracted from ECG beats of one subject are assigned to one of these sets. The training set contains 80% of randomly selected subjects, whereas the remaining 20% percent of subjects is used in the test set. Considering the fact that there are 104 subjects in the database, 83 subjects are used in the training set, and 21 subjects in the test set. In order to get robust results, this random split is performed ten times, and the geometrical mean of these ten repetitions is reported. For classification quality evaluation, both the online and offline phases of our classification technique are implemented in MATLAB.

In this implementation, we fix the first level classifier to contain $K = 5$ features. Each succeeding classification level contains features from the previous level and the next five relevant features obtained through feature selection. For instance, for $m = 2$, we have three different classifiers within our classification technique. Namely, the first-level classifier that contains five features, the second-level one that contains ten features including the five features from the first-level classifier, and the full classifier that contains the entire set of available features ($n = 72$). The classifier that uses all available features reaches a geometric mean of 83.26% (Sensitivity = 87.95%, Specificity = 78.82%). The overall geometrical mean of sensitivity and specificity, as well as the expected complexity of the proposed event-driven classification technique, are estimated for different values of decision-making thresholds t_{h_l} and classification levels m. Fig. 2.15 shows the overall geometrical mean of sensitivity and specificity of the proposed event-driven classification technique (vertical axis) versus the number of classification levels (horizontal axis) for different values of decision-making thresholds. As shown in Fig. 2.15, an increase in the number of classification levels leads to an increase in the classification performance. This is due to the fact that by increasing the value of decision-making threshold, we start invoking higher level classifiers that are more accurate. However, we see that for a particular value of decision-making threshold, for $m \geq 4$, there is no major improvement in terms of classification quality regarding the number of classification levels.

Fig. 2.16 shows the expected complexity of the proposed technique versus the value of the decision-making threshold for different number of classification levels m. From this figure, we can see that an increase in the value of decision-making threshold leads to an increase in the expected complexity. This is due to the fact that for higher values of decision-making threshold, we invoke higher level classifiers that use more

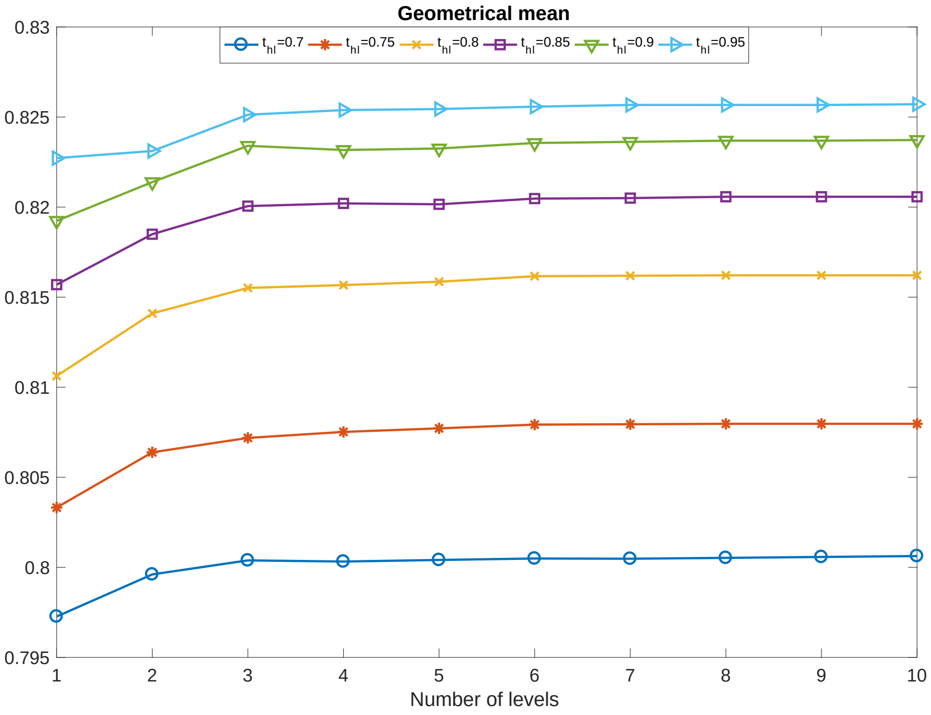

Figure 2.15: Geometrical mean of the proposed real-time event-driven classification technique versus the number of classification levels for different values of decision-making thresholds t_{h_l}.

features, and therefore, are more complex. As seen in Fig. 2.16, for $m \geq 4$, there is no major improvement in terms of computational complexity regarding the value of decision-making threshold.

Similar to Fig. 2.15, based on Fig. 2.17, we see that for a fixed value of decision-making threshold, also after $m = 4$ classification levels, there is no improvement in terms of expected computational complexity either. Therefore, from Fig. 2.17, we can deduce that for our experiment only four classification levels are needed, they are sufficient to fulfill the required classification performance (with minimum complexity possible). The full classifier that reaches an accuracy of 83.26% (Sensitivity = 87.95%, Specificity = 78.82%) uses $n = 72$ features. As shown in Fig. 2.17, in the case of having four classification levels and applying $t_{hl} = 0.7$ as a decision-making threshold, we end up with an expected computational complexity of 7.7 and an accuracy of 80.32% (Sensitivity = 81.02%, Specificity = 79.63%). As the expected computational complexity is related to the number of used features, this negligible loss of 3% in terms of classification quality, reduces the computational complexity by a factor of 9.35.

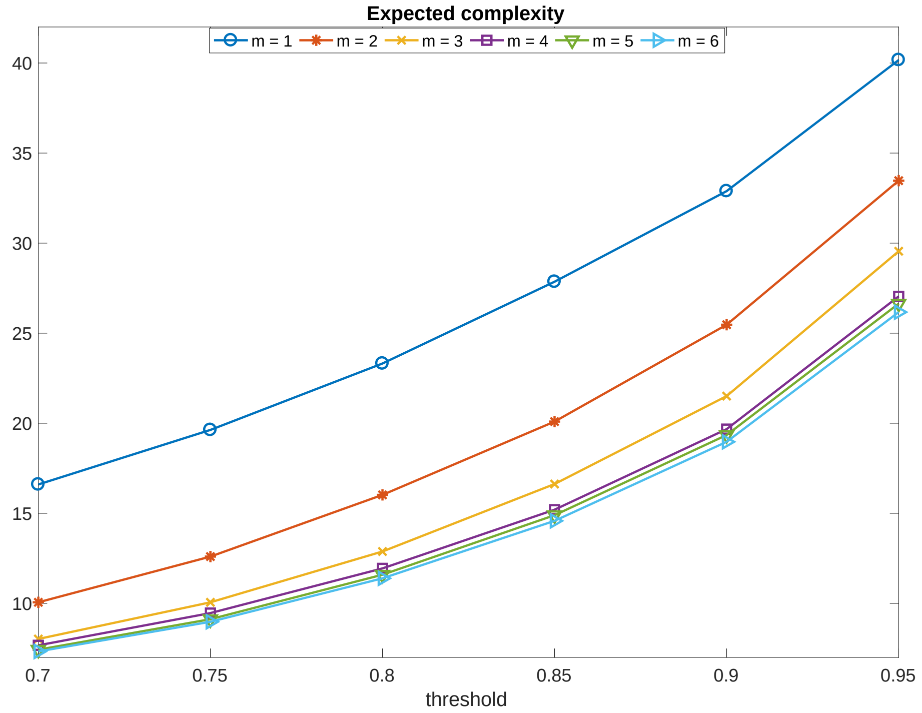

Figure 2.16: Expected complexity ($\mathbb{E}(C)$, in Section 2.9) of the proposed real-time event-driven classification technique versus the value of decision-making threshold for different number of classification levels m.

2.11.2 Energy Consumption and System Battery Life Analysis

The same code and inputs of the experiments performed in Subsection 2.11 are considered, and subsequently ported into C code to assess the classification performance and the energy consumption of the proposed event-driven classification technique against the energy consumption of the full classifier on a commercially available Gecko EFM32 development board (GeckoBoard, 2017). This board includes the same ARM Cortex-M3 core as in the SmartCardia INYU device, and provides the Simplicity Studio software in which a full energy profiler is integrated. The detailed energy consumption of our technique along with different classification levels is shown Fig. 2.18.

Herein, $m = 4$ classification levels are considered and the number of features in the first level is fixed to $K = 5$. The full classifier uses $n = 72$ features. By running the classification technique on the Gecko EFM32 board, we obtain that the execution time for processing of one heartbeat is equal to $t_1 = 24.27s$. On the other hand, the time it

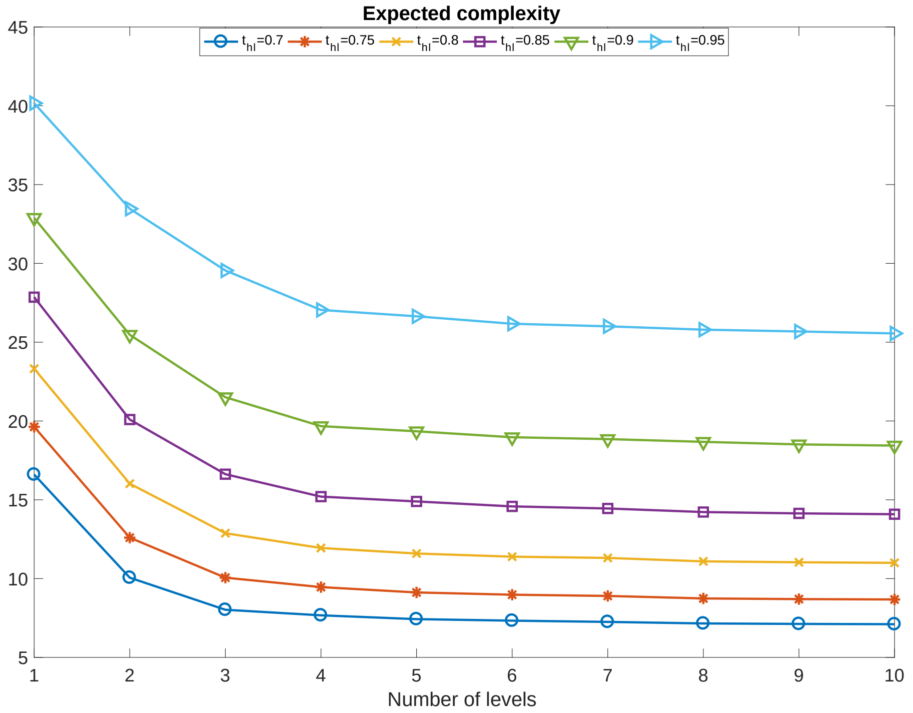

Figure 2.17: Expected complexity ($\mathbb{E}(C)$, in Section 2.9) of our real-time event-driven classification technique versus the number of classification levels for different values of decision-making thresholds t_{h_l}.

takes for the full classifier to process one heartbeat is equal to $t_2 = 69.95s$. Fixing that the processing of one heartbeat is done once every 90 seconds, the CPU duty cycle (d_C, used in Section 2.9) of the full classifier is 77.73%, whereas the CPU duty cycle of our approach is equal to 26.97%. For a standard 710mAh battery, since the processing is done once every 90 seconds, the full classifier runs for 59.83 hours on a single battery charge. The proposed classification technique reaches 155.41 hours, thus allowing for more than 6 days of operation. Therefore, the event-driven classification technique extends the battery life by a factor of 2.60. The energy consumption of different components of the SmartCardia INYU device is shown in Table 2.5.

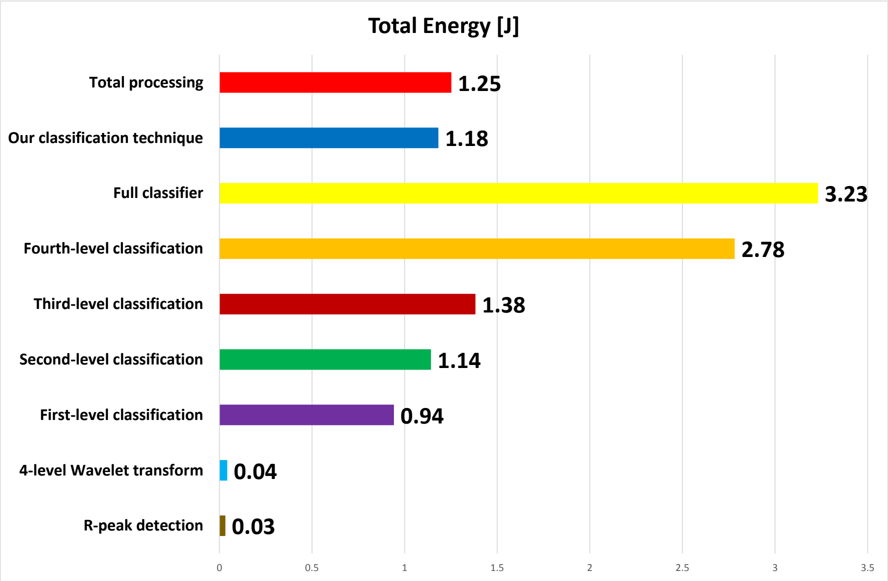

Figure 2.18: Overview of the energy consumption of different classification levels.

Operation	Current (mA)	Duty cycle (%)	Avg. current (mA)
ADS1191 (ADSECG, 2011)	0.427	100	0.427
MPU-6000 (MPU, 2013)	0.005	100	0.005
Signal acquisition subsystem			**0.432**
ECG delineation	14.397	1.71	0.246
MI processing	14.397	26.97 (77.73)	3.882 (11.190)
Idle time	0.018	71.32 (20.56)	0.013 (0.004)
STM32 (STM32, 2013) data processing subsystem			**4.141** (11.440)
nRF8001 (NRF, 2015)	11	0.0007	0.008
Wireless subsystem			**0.008**
Total			**4.581** (11.880)

Table 2.5: Current used for MI detection on the target device. Currents drawn by the signal acquisition subsystem are experimentally obtained by running our classification technique on the Gecko EFM32 development board. The currents outside parentheses are currents drawn by our classification technique, while the currents in paretheses are drawn by the full classifier.

3 Monitoring of Neurological Diseases

This chapter covers the second part of my thesis. Namely, the first part of this chapter explains the electrical activity in the human brain and the generation of the electrical signal that can be measured on the surface of the head. Furthermore, a brief history of Electroencephalogram (EEG) along with its recording and the characteristic EEG rhythms is provided. The rest of the thesis focuses on the detection of epileptic seizures. Fistly, a real-time method based on EEG signals obtained from four EEG electrodes is presented. In the last part of the thesis, a novel interpretable approach to false alarm reduction for long-term epileptic seizure detection is proposed.

3.1 Neuronal Activity

The human brain contains approximately 86 billion neurons (Herculano-Houzel, 2009). Neurons are the cells that along with glia make up our nervous system, and they are composed of four main parts: a cell body, an axon, dendrites, and axon terminals, shown in Fig. 3.1. Each neuron is connected to a lot of other neurons, and it gets information from its dendrites. The dendrites take the information from axon terminals of connected neurons and transmit it to the cell body. The information is further propagated down the axon until it reaches axon terminals where a synaptic contact with another neurons is made. The propagation of information is unidirectional, from the sending neuron (presynaptic neuron) to the receiving one (postsynaptic neuron).

In its resting state, a neuron has a voltage across its membrane that can result in an action potential generated by different ion concentrations inside and outside the cell. The action potential leads to depolarization and repolarization of the neuron, as explained in Section 2.2. The firing of an action potential happens once the membrane potential of a neuron reaches its threshold value, and it highly depends on the connections with the surrounding neurons. More specifically, each neuron is con-

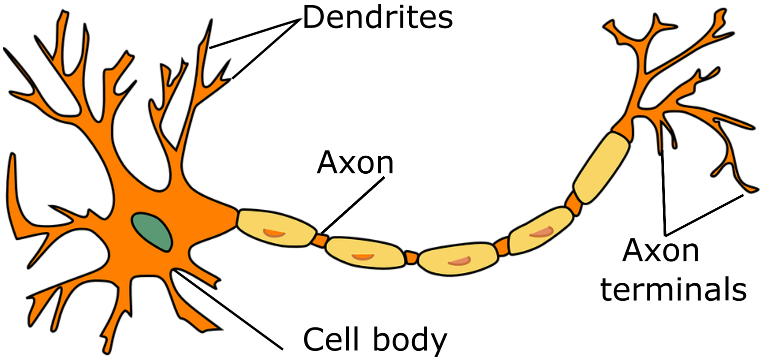

Figure 3.1: Morphology of a neuron.

nected to many other neurons through its dendrites. The communication between neurons is made at junctions called synapses where the information is transmitted in the form of chemical receptors called neurotransmitters. The neurotransmitters of the presynaptic neuron bind to the protein receptors on the postsynaptic cell. Depending on the type of released neurotransmitters, as well as on the type of the receptors on the postsynaptic cell, either positive or negative ions will travel through the postsynaptic membrane. There are two main types of neurotransmitters and receptors, the excitatory and the inhibitory ones. The excitatory ones increase the membrane potential of the postsynaptic cell increasing the probability of firing an action potential, whereas the inhibitory ones have the opposite effect, keeping the neuron from firing. The firing of a single neuron depends on the summation of all excitatory and inhibitory signals coming from the connected surrounding neurons. In case of firing, an action potential is passed down the axon of the postsynaptic cell.

The propagation of an action potential starts at the part of the neuron where the cell body connects to the axon (called axon hillock). Once the threshold value of the membrane potential is reached, the hillock depolarizes, changing the voltage of the adjacent axon segment. Each axon segment triggers the depolarization of its adjacent segment. The insulating cells around the axon make up the myelin sheath allowing a faster signal propagation down the axon. Once the signal reaches the axon terminals, synaptic contacts with connected neurons are made, starting the process all over again in the postsynaptic neurons.

The synaptic excitation of the dendrites of many neurons in the brain gives rise to the currents that can be measured in the extracellular medium (Buzsáki et al., 2012). Even though all of the neurons in the brain contribute to the generation of these currents, pyramidal neurons contribute most with their bodies orthogonal to the brain surface (Jefferys, 1995). The dendrites of these neurons constitute masses of equally oriented fibers that acquire properties of electric current dipoles during postsynaptic potentials (Ivanitsky et al., 2009). Nevertheless, the electric contribution of every individual neuron is extremely small, as the signal has to penetrate many non-neuronal tissues, including the meninges, fluid, bones of the skull, and skin, to reach the electrodes (Bear et al., 2007). Hence, it takes many pyramidal neurons, activated together, to produce an electrical signal on the surface of the head (Bear et al., 2007). The measured signal represents the sum of electrical contributions of all simultaneously activated neurons below the selected pair of electrodes and is called EEG. The EEG signal amplitude reflects the synchronization of underlying neurons. Namely, in case of many neurons firing simultaneously, the resulting EEG signal will be high in amplitude, whereas in case of neuronal firing happening at irregular time moments, the obtained signal amplitude will be low.

3.1.1 History of EEG

The first roots of the EEG date back to 1875 when English physiologist Richard Caton observed electrical impulses from the surfaces of monkey and rabbit brains (Coenen and Zayachkivska, 2013). The first human EEG was successfully recorded in 1924 on a 17-year-old boy during a neurosurgery (İnce et al., 2020) by German psychiatrist Hans Berger, also known as the inventor of EEG. In 1929, Berger succeeded in recording the electrical activity from the surface of the human brain (Berger, 1931). One of his findings was also the existence of different wave patterns present in the brain, such as alpha waves, also known as Berger waves. Berger also studied different EEG changes related to attention and mental effort, as well as EEG alternations associated with brain disorders (Haas, 2003).

3.1.2 EEG Recording

EEG measures electrical activity in the brain generated by the synchronized activity of underlying neurons. Depending on the way EEG signals are acquired, EEG signal recordings can be divided into:

- Invasive EEG recordings
- Scalp EEG recordings

Invasive EEG recordings require the use of electrodes surgically implanted on the surface (electrocorticogram, ECoG) or in deep structures of the brain (stereo-EEG) (Ball et al., 2009). Implanting electrodes in the brain offers a high spatial and temporal signal resolution, as the electrodes are close to the source, and therefore, the signal gets less distorted by the electrical conductivity of the surrounding tissues before reaching the electrodes. Invasive EEG recordings are essential for treating patients with advanced Parkinson's disease (Groiss et al., 2009). Namely, deep brain stimulation can slow the disease propagation in patients with unstable medication reducing tremor and improving their motor skills. Furthermore, invasive EEG recording is widely used for diagnosis in patients suffering from epileptic seizures that are resistant to pharmacological treatment (Ball et al., 2009). Namely, in these patients, invasive EEG is used for presurgical evaluation to accurately localize the seizure-onset zone for surgical removal (Fong et al., 2012).

Even though invasive EEG recordings offer a high spatial and temporal signal resolution, these recordings suffer major drawbacks. Namely, the complications related to electrode implantation include infections and intracranial hematomas (Tanriverdi et al., 2009), permanent neurological deficit (Cossu et al., 2005), raised intracranial pressure, infarction, and bone infection (Wong et al., 2009). Apart from their high degree of invasiveness, another major disadvantage of these procedures is their limited spatial sampling to the area of implantation, which may result in inaccurate localization (Santiuste et al., 2008).

On the other side, scalp EEG is a noninvasive recording of electrical brain activity involving no risk and complications, as no electrode implantation is required. Scalp recordings use a set of electrodes placed along the scalp along with a conductive gel that improves the conductivity between the scalp and the electrode surface. The placement of electrodes is based on the international 10-20 system (Jasper, 1958) that uses 23 EEG electrodes placed at fixed distances with respect to the anatomical landmarks (nasion, inion, and pre-auricular points interior to each ear) in steps of 10 or 20%. This standard method of placing electrodes can be further extended to higher density electrode settings such as 10/10 and 10/5 systems (Jurcak et al., 2007). The use of EEG head caps with embedded electrodes allows the quick and accurate placement of any number of electrodes (up to 256) (Ivanitsky et al., 2009). These head caps are further discussed in Subsection 3.2. Nevertheless, high-density electrode settings are beyond the scope of this thesis. The electrode setting used in this thesis is shown in Fig.3.2.

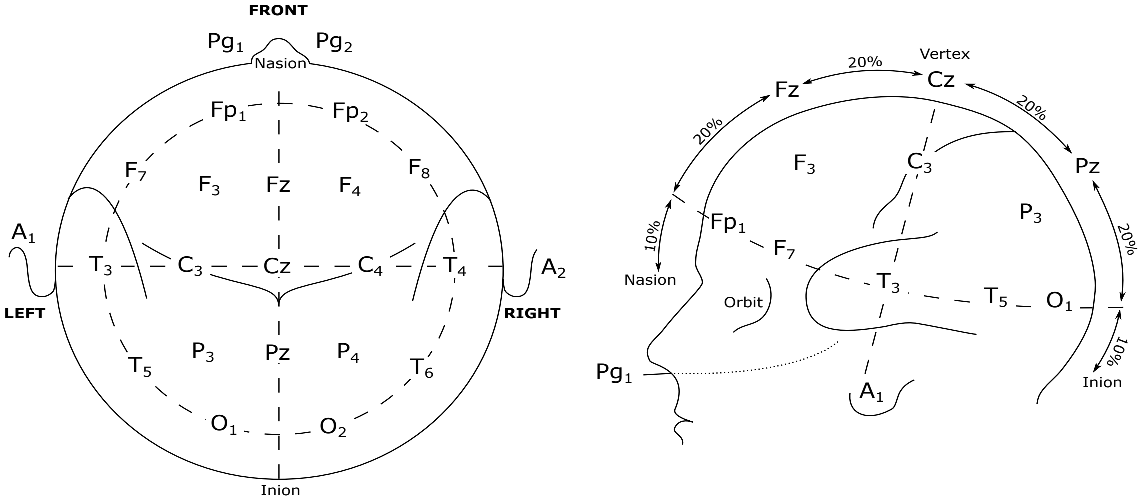

Figure 3.2: The international 10-20 EEG electrode placement used in this thesis. Each electrode is represented by letters and a number. The numbers indicate the side of the head so that odd number are on the left side and even numbers are on the right. Lower numbers are attributed to the electrode that is closer to the midline. The midline is represented the dotted line that connects the nasion and the inion, and it consists of electrodes with a subscript z. The letters are the indicators of the position on the head, where F stands for frontal, C for central, and P for parietal lobe. Electrodes Pg1 and Pg2 represent the location of pharyngeal electrodes, whereas electrodes A1 and A2 are used for contralateral referencing of all EEG electrodes.

EEG signals can be displayed in different montages. The most commonly used type of montage is a bipolar montage in which the difference between two adjacent channels is displayed. Another common type of montage is a common average reference montage. Here, the difference between an electrode of interest and the selected reference point is displayed. Typically, an average of the rest of the head is used as reference. Nevertheless, an average of signals from both earlobes can also be used as a reference point (Ivanitsky et al., 2009).

Scalp recordings suffer a low spatial resolution due to different neuronal and non-neuronal tissues EEG signals have to penetrate before reaching the electrodes placed on the scalp. These tissues act as a spatial low-power filter that spreads electric potentials all around the head (Ivanitsky et al., 2009). Therefore, the scalp EEG fails to precisely localize the seizure-onset zone (Ball et al., 2009). Nevertheless, scalp EEG recordings remain a fundamental tool in studying electrical brain activity mainly due to their noninvasive nature and low price. Furthermore, the temporal resolution of scalp EEG is much higher in comparison to other noninvasive methods used for measuring brain activity, such as positron emission tomography (PET) and functional magnetic resonance imaging (fMRI) (Sejnowski et al., 2014).

3.1.3 EEG Rhythms

Rhythmical properties of EEG come from two main sources. On the one hand, there are neurons in the human body that can provoke oscillations of the membrane potential in the absence of any synaptic input, resulting in bursts of action potentials. (Ivanitsky et al., 2009). These membrane potential oscillations are the result of interactions between different types of voltage-gated ion channels (Ivanitsky et al., 2009). On the other hand, a large assembly of synchronized neuronal groups form networks with oscillatory properties (Ivanitsky et al., 2009).

Oscillatory properties of EEG span from 0.5Hz to 200Hz and are broken down into eight frequency bands where each band correlates with a distinct behavioral state (level of attentiveness, sleeping, or waking) or pathology (seizures or coma) (Bear et al., 2007). These bands are typically referred to as follows:

- Delta rhythm - It is represented by slow waves in the frequency range from 1 to 4Hz, mostly seen in deep sleep or pathological sleep such as coma. These waves tend to be high in amplitude as cortical neurons are not engaged in information processing, and large numbers of them are highly synchronized (Bear et al., 2007).

- Theta rhythm - The range of frequency this rhythm can be seen from 4 to 7Hz. These waves are usually present in young children, but can also be seen during both sleeping and waking states in adults (Bear et al., 2007).

- Alpha rhythm - The most commonly encountered rhythm during wakefulness, especially prominent in occipital recording site during relaxation with eyes closed (Ivanitsky et al., 2009). These waves attenuate with eye-opening or mental exertion. The frequency range of this rhythm spans from 7 to 14Hz.

- Mu rhythm - Similar to alpha rhythms in terms of frequency from 8 to 13Hz, but are more concentrated over the motor and somatosensory areas (Bear et al., 2007).

- Beta rhythm - This rhythm lies in the frequency range from 15-30Hz and is associated with waking states. It is believed that this rhythm underlies cognitive processing (Ivanitsky et al., 2009).

- Gamma rhythm - Fast waves that range from 30-90Hz and are associated with activated cortex. This rhythm is believed to be involved in the sensory processing (Ivanitsky et al., 2009).

Apart from the aforementioned EEG rhythms, there are other EEG rhythms, such as spindles and ripples. Spindles are represented by short waves from 8 to 14Hz that can be seen during sleep, whereas ripples are associated with waking states and can be seen in the form of brief waves from 8 to 200Hz (Bear et al., 2007).

The existence of rhythmical properties of scalp EEG gives rise to the possibility of using EEG signals for detection of various neurological disorders. These disorders include epileptic seizures, sleep disorders, Alzheimer's disease, schizophrenia, stroke, brain tumors and injuries, dementia, development delays, as well as other disorders such as behavioral and attention ones (Sharma et al., 2019). Due to the unpredictable nature of epileptic seizures, patients with epilepsy are at higher risk of accidents compared to the general population (Cornaggia et al., 2006). A prompt response and assistance provided by family members and/or caregivers at the time of a seizure can be beneficial to avoid these accidents as well as epilepsy-related death. During seizures, there is an extreme synchronization of large neuronal populations mostly reflected onto the EEG signal morphology (Jiruska et al., 2013) in time and frequency domain. Furthermore, there are publicly available databases of epileptic patients. Therefore, the rest of this thesis focuses on the detection of epileptic seizures.

3.2 Epilepsy

Today, epilepsy represents one of the major neurological health issues affecting more than 65 million people worldwide (Patricia O. Shafer, RN, 2014) and it is among the most prevalent neurological disorders along with migraine, stroke, and Alzheimer's disease (Hirtz et al., 2007). Despite substantial progress in the efficacy and tolerance of anti-epileptic drugs, one-third of the epileptic patients continue to have seizures (Kwan and Brodie, 2010).

Epilepsy is characterized by intermittent seizures caused by disturbances in the normal electrical activity of the brain (Patricia O. Shafer, RN, 2014). These disturbances affect either the entire cerebral cortex (generalized seizures), or just a particular area of the cortex (partial seizures) (Bear et al., 2007). Both, generalized and partial seizures, involve an extreme level of neuronal synchronization within the affected areas that is typically seen on the EEG signal morphology. These seizures can last from seconds to minutes and can range from an impaired consciousness, automatic movement, up to severe convulsions of the entire body. Impaired consciousness may lead to driving accidents, drowning, as well as other serious injuries (Blumenfeld, 2012). This contributes to a severe reduction in the quality of life and psychosocial functioning. The unpredictable nature of seizures can be life-threatening with a 2–3 times higher mortality rate in these patients than in the general population (Szucs et al., 2006). Furthermore, the most severe seizures, especially when occurring at night, can result in sudden unexpected death in epilepsy (SUDEP) (Ryvlin et al., 2009). Epilepsy-related causes of death account for 40% of mortality in high-risk groups of people with epilepsy (Téllez-Zenteno et al., 2005). In order to reduce morbidity and mortality due to epilepsy, real-time patient monitoring is essential for alerting family members and caregivers to administer prompt emergency medication and assist a person at the time of a seizure.

In the medical community, the standard procedures commonly used for epileptic patient monitoring are performed based on the video-EEG (v-EEG) (Cascino, 2002). v-EEG takes place in hospitals over several days and involves the acquisition of the audio signal using a microphone, the video recording of the patient using a camera, the brain electrical activity using EEG, as well as the electrical activity of the heart using Electrocardiogram (ECG). Considering the unpredictability of seizures, it is not possible to monitor patients on a long-term basis, due to the highly intrusive nature of these procedures.

With the currently flourishing era of embedded computing, wearable technologies are opening up new opportunities for real-time epileptic seizures monitoring. These new ultra-low energy portable devices overcome the limitation of medical equipment for real-time and long-term patient monitoring. In particular, the portability of these devices allows real-time remote patient monitoring daily. Ambulatory real-time patient monitoring allows hospital physicians to access patient information remotely and, hence, prevent further patient state deterioration by early detection of epileptic seizures.

The most popular wearable system for the detection of epileptic seizures consists of EEG head caps with embedded electrodes for measuring the electrical activity of the brain (Blom and Anneveldt, 1982). This system uses the international 10-20 electrode placing system, mentioned in Subsection 3.1.2. In (Ocak, 2009), a new scheme for epileptic seizure detection based on approximate entropy and discrete wavelet transform analysis of 100 EEG channels has been proposed. Furthermore, different approaches that use artificial neural networks for epileptic seizure detection based on EEG signals are reported in the literature (Webber et al., 1996). Nevertheless, all these methods use EEG head caps that are cumbersome and uncomfortable as they require from 23 to 256 wired electrodes to be placed on the patient's scalp. The majority of epileptic patients refuse to wear these caps due to the effect of social stigma they are facing in their daily lives (Hoppe et al., 2015).

In order to alleviate the impact of social stigma on patient's daily life, several studies have been conducted to reduce the number of EEG electrodes needed for epileptic seizure detection. For instance, in (Fürbass et al., 2017), the authors use two different montages with a reduced number of electrodes for automatic multimodal detection of epileptic seizures: eight electrodes in forehead montage, and seven electrodes in posterior montage. However, the proposed solution is still intrusive and, hence, the problem of social stigma persists.

One of the contributions to this thesis is a real-time method for epileptic seizure detection that uses a reduced set of EEG electrodes (Section 3.3), validated on CHB-MIT database (Physionet.org (Goldberger et al., 2000)). Experimental setup along with the evaluation of classification performance of this method is presented in Section 3.4.

3.3 Real-Time Method for Epileptic Seizure Detection

The overall flow of the proposed real-time method for epileptic seizure detection is shown in Fig. 3.3, and it consists of two main phases: feature extraction and classification. Feature extraction is explained in Subsection 3.3.1. Random forest explained in Section 2.4.3 is used for differentiating between seizures and non-seizure events.

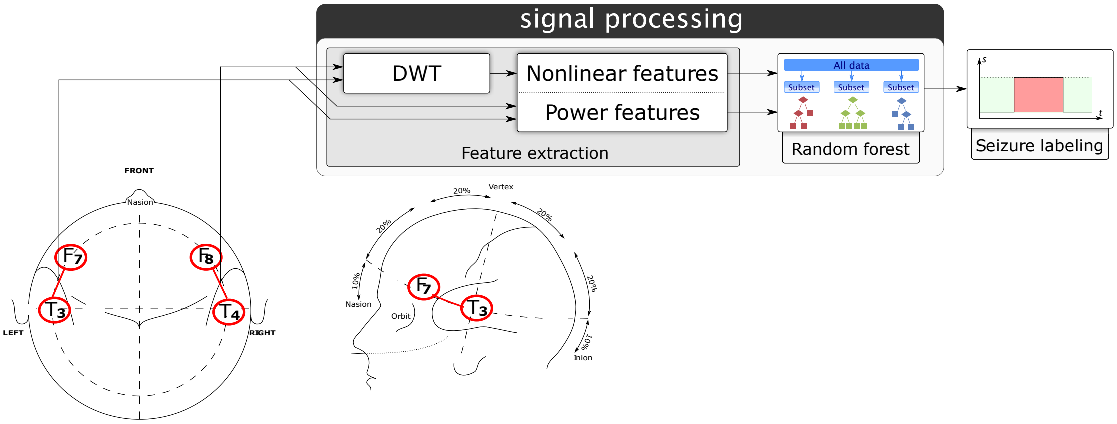
signal processing
DWT
Nonlinear features
Power features
Feature extraction
All data
Subset
Subset
Subset
Random forest
s
t
Seizure labeling
FRONT
Nasion
F7
F8
T3
T4
LEFT
RIGHT
Vertex
20%
20%
20%
20%
10%
10%
Nasion
Orbit
F7
T3
Inion

Figure 3.3: The overall flow of the proposed method for detection of epileptic seizures.

3.3.1 Feature Extraction

EEG signal-morphology based features: In order to capture the complex, non-stationary, and nonlinear nature of EEG signal morphology, various entropy measures along with several power features are extracted. When using entropy measures for epileptic seizure detection, it has been shown that applying a discrete wavelet transform (DWT) as a pre-processing step improves the detection rate by more than 20% (Ocak, 2009). Therefore, EEG signals are decomposed down to level seven using a DWT. In particular, Daubechies 4 (db4) is used as wavelet basis function. The value of sample entropy is calculated from detail wavelet coefficients at level 6 and 7, whereas the rest of the nonlinear features are calculated from detail wavelet coefficients at levels 3, 4, 5, 6, and 7 for different values of input parameters.

- Sample entropy: Given a time-series $X = x(1), \dots, x(N)$ along with the pattern length m and the criterion of similarity r (Xinnian Chen et al., 2005), the following sequences are defined $X_m(i)$:

  $$X_m(i) = \{x(i), x(i+1), \dots, x(i+m-1)\}$$
  $$\forall i = [1, N-m+1].$$

  Then, two patterns $X_m(i)$ and $X_m(j)$ are similar if the difference between any pair of corresponding measurements in the patterns is less than r:

  $$|x(i+k) - x(j+k)| < r, \forall k = [0, m).$$

  All sequences of length m, X_m, along with the criterion function $C_{im}(r)$ are defined as follows:

  $$X_m = \{X_m(1), X_m(2), \dots, X_m(N-m+1)\},$$

  $$C_{im}(r) = \frac{n_{im}(r)}{N-m+1},$$

  where $n_{im}(r)$ is the number of patterns in X_m that are similar to $X_m(i)$ excluding self-matches. The sample entropy is defined as:

  $$SampEn(x, m, r) = \ln(\frac{C_m(r)}{C_{m+1}(r)}),$$

  where $C_{im}(r)$ is calculated for each pattern in X_m. and we define $C_m(r)$ as the mean over $C_{im}(r)$. In this work, parameters $m = 2$, and $r = k \cdot \text{std}(signal)$ are used, where $\text{std}(signal)$ represents the standard deviation of a signal, and $k \in \{0.2, 0.35\}$.

- Permutation entropy: Given a time-series $\{x_t\}_{t=1,\ldots,T}$, where T is the length of the time-series, all possible $n!$ permutations are calculated (Bandt and Pompe, 2002). The parameter π corresponds to the permutation type, whereas the parameter n represents the number of instances considered to estimate the permutation entropy (e.g., $(x_i, x_j, i \neq j)$), where $n = 2$, or $(x_i, x_j, x_k\ i \neq j \neq k)$, where $n = 3$. For instance, for $n = 2$, π can take on only two values. For simplicity of explanation, let us denote them by 01 or 10. If $x_t < x_{t+1}$, then $\pi = 01$, and if $x_t > x_{t+1}$, then $\pi = 10$. Hence, in case of $n = 2$, there are just two possible permutations, namely, 01 and 10. The relative frequency for type π is estimated as follows:

  $$p(\pi) = \frac{\text{number of perms that have the type } \pi}{T-n+1}.$$

  The permutation entropy of order $n \geq 2$ is defined as:

  $$PE(n) = -\sum_{\pi} p(\pi)\log(p(\pi)).$$

  In this work, the value of permutation entropy is computed for $n \in \{3,5,7\}$.

- Renyi entropy: This entropy is calculated as follows (Acharya et al., 2015):

  $$RE(q) = \tfrac{1}{1-q}\ln\sum p_i^q,$$

  where $q \neq 1$, and p_i defines the normalized spectral power in i-th band.

- Shannon entropy: This entropy is the special case of Renyi entropy (Acharya et al., 2015) for $q = 1$, namely:

  $$SE = -\lim_{q\to 1} RE(q) = -\sum p_i \ln(p_i).$$

- Tsallis entropy: It is defined as in (Acharya et al., 2015):

  $$TE(q) = \tfrac{1}{q-1}(1-\sum p_i^q).$$

Complementary features - power features: Epileptic seizures affect the distribution of EEG signal power in different frequency bands (Sharma, 2015; EPILEPSY, 2015). The most commonly reported features extracted from EEG signals in the literature (Bell and Cuevas, 2012) rely on the spectral power of EEG signals in the frequency bands mentioned in Subsection 3.1.3. Therefore, the total and the relative EEG signal powers in these bands are calculated to complement the signal-morphology based features. These power features are extracted from raw EEG signals.

3.4 Experimental Setup and Results

In this section, the proposed method for detection of epileptic seizures is applied on Physionet.org CHB-MIT Scalp EEG database (Goldberger et al., 2000; Shoeb, 2009) and the classification performance is evaluated. This database is described in Subsection 3.4.1. Then, the target computing system of the e-Glass wearable platform on which the proposed method is ported is explained in Subsection 3.4.2. Finally, the performance of the proposed real-time detection algorithm and the energy consumption estimation are presented in Subsection 3.4.3.

3.4.1 CHB-MIT Database

This database consists of more than 980 hours of long-term EEG recordings obtained from 24 children aged 1.5-22 with refractory seizures. All EEG signals are sampled at $f_s = 256$Hz. The recording files of each patient contain exactly one of digitized EEG signals, although those belonging to case chb10 are two hours long, and those belonging to cases chb04, chb06, chb07, chb09, and chb23 are four hours long. Ictal and interictal phases are clearly indicated. For ictal events, the onset and offset timestamps of each seizure are specified in the separate text files. In order to be able to evaluate the performance of the proposed method and the impact of the reduced number of electrodes, multiple traces from 23 patients are considered. These traces include the total number of 182 seizures. The only patient that is not taken into consideration is chb24. Namely, the recordings of this patient were added additionally to the database and are not compliant with the standard acquisition protocol (Jasper, 1958).

3.4.2 Target Platform

The used e-Glass wearable system is shown in Fig. 3.4. This system acquires EEG signals from two electrode pairs: F_7T_3, and F_8T_4, shown in Fig. 3.3. The sampling frequency of acquired EEG signals ranges from 125 Hz up to 16 KHz with up to 16-bit resolution. Furthermore, this wearable platform features an ultra-low power 32-bit microcontroller STM32L151 (STM32, 2013) with an ARM® Cortex®–M3, which can operate at a maximum frequency of 32 MHz. e-Glass contains a 570 mAh battery, as well as 48 KB RAM, 384 KB Flash, and several analog peripherals including a 24-bit ADC (ADS, 2012). At the time of a seizure, a warning from e-Glass is sent to the caregivers through communication with a mobile phone. For these purposes, Bluetooth low energy (nRF8001) is used (NRF, 2015).

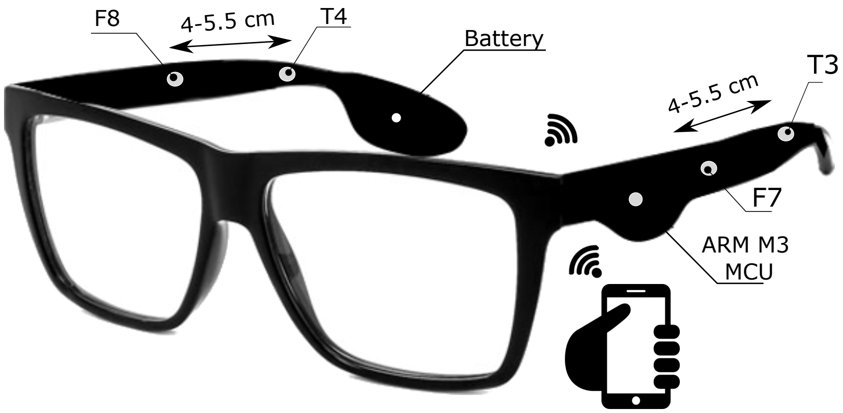

Figure 3.4: e-Glass: a wearable system used for evaluating the performance of the proposed method for real-time epileptic seizure detection.

3.4.3 Performance Evaluation

Classification Performance Metric and Cross-Validation: To evaluate the classification performance of the proposed method, both sensitivity and specificity metrics are considered, as well as their geometric mean ($\mathsf{G}_{\mathsf{mean}}$). These metrics are defined in Section 2.4.4. A sliding window of four seconds with 75% overlap is used for extracting the features mentioned in Subsection 3.3.1. These features are extracted for both, seizure and seizure-free signal parts. Based on the discussion with expert neurologists, seizure-free signal parts are chosen at least 30 minutes after the last and before the incoming seizure. In order to have balanced classes, the same number of seizure and seizure-free windows is used for each patient.

Personalized Versus Generic: The difference in terms of classification performance between the personalized and generic approach is investigated. Namely, the generic approach uses leave-one-out cross-validation scheme. Out of 23 subjects, a single subject is retained for testing the model, and the remaining 22 are used as training data. The personalized approach performs the classification based on the features extracted from different trials of one subject. Hence, this classification is done per subject. While splitting the data into training and test sets each trial is included into either the training set or the test set. First, the number of seizures for each patient is found. As the minimum number of seizures per patient is three, in order to make sure that the test set contains at least one seizure, 30% of seizure data is put in the test set, whereas 70% goes to the training set. For instance, let us assume that patient A had 6 seizures. Then, feature windows that correspond to two seizures are put in the testing set, whereas the remaining four seizure windows are put in the training test. All possible combinations of six seizures are used to select two at a time for test set.

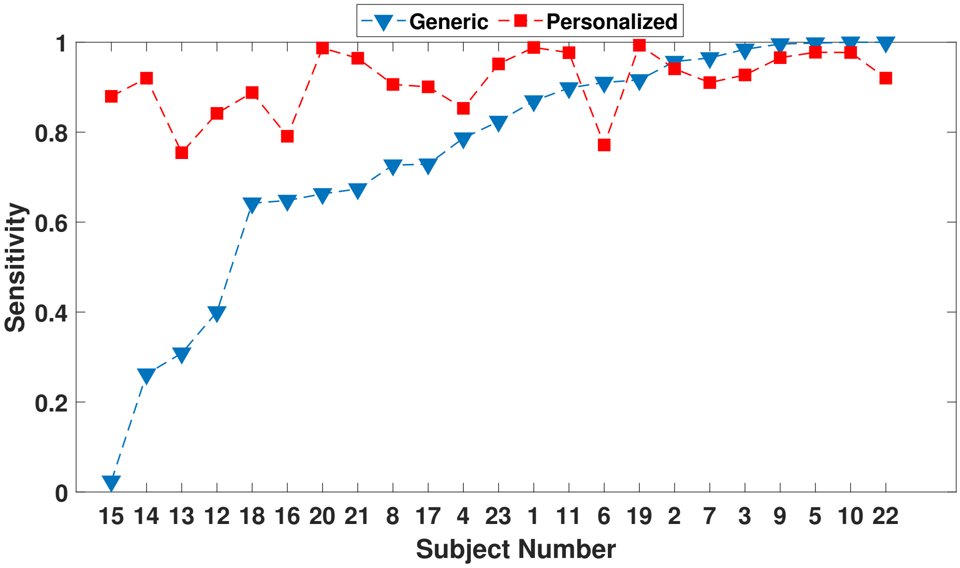

Figure 3.5: Sensitivity (sensitivity) for personalized versus generic approach using four electrodes.

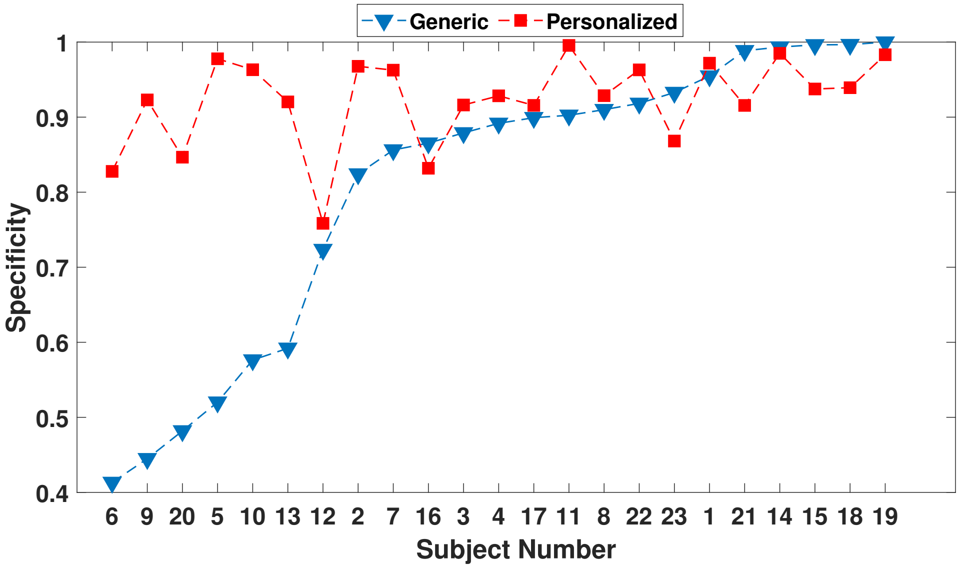

Figure 3.6: Specificity (specificity) for personalized versus generic approach using four electrodes.

For each of these combinations, the rest of seizure-free data is split into training and test sets for all possible 70–30% splits, and the value of $\mathrm{G_{mean}}$ (Eq. 2.6) for each subject in the personalized approach is reported.

Fig. 3.5, 3.6 3.7, show the sensitivity, specificity, and $\mathrm{G_{mean}}$ across all subjects (vertical axis) for four electrodes used: F_7T_3, and F_8T_4 in Fig. 3.3, respectively. The geomet-

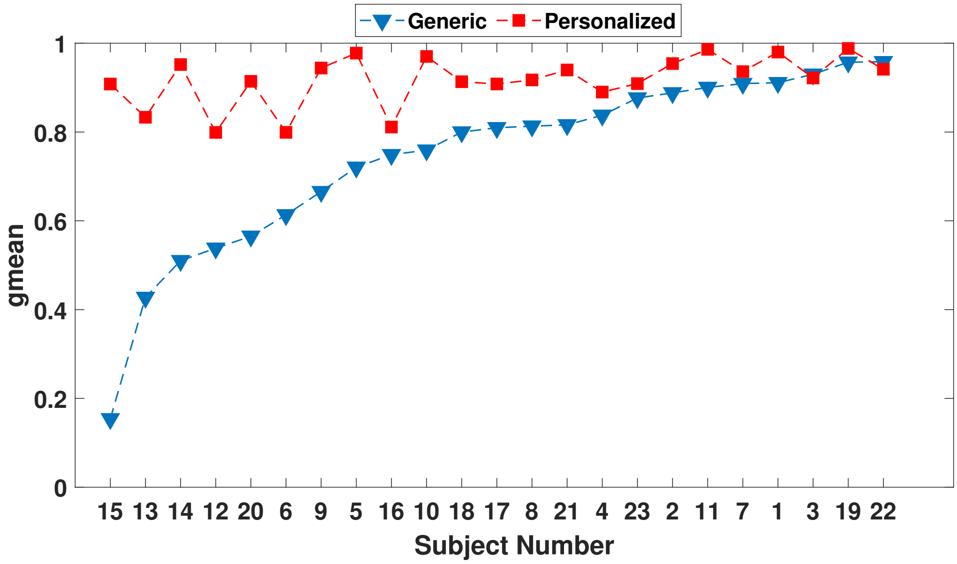

Figure 3.7: Geometric mean (G_{mean}) for personalized versus generic approach using four electrodes.

ric mean across all subject for the generic approach is 70.33% (sensitivity = 63.49%, specificity = 77.91%), whereas this value reaches 91.54% for the case of our personalized approach (sensitivity = 90.98%, specificity = 92.10%). In the best case, for patient 15 our approach improves the detection rate for 75.42%, as shown in Fig. 3.7. As seen from this figure, the personalized classification approach can adapt to significant inter-patient variations in EEG patterns. Thus, it achieves a higher classification performance.

EEG Caps Versus e-Glass: Fig. 3.8, 3.9, 3.10 show the values of classification metrics for personalized approach using EEG caps (all available electrodes) versus the values of those obtained from e-Glass (four selected electrodes: F_7T_3, and F_8T_4). The geometrical mean across all subjects is 95.71% (sensitivity = 96.33%, specificity = 95.10%). and 91.54% (sensitivity = 90.98%, specificity = 92.10%) for all electrodes and for the selected subset of electrodes, respectively. As it can be observed from Fig. 3.10, using only a few electrodes it is possible to ensure a high degree of wearability without any major loss in classification performance. Even though there is a slight difference for subject number 7 in Fig. 3.10, this difference is within the expected statistic range since the number of trials for this subject is limited. Nevertheless, the maximal obtained specificity for all electrodes reaches a value of 95.10%. Considering the fact that we classify four-second windows, one out of each 20 windows will indicate the presence of a seizure. Therefore, each 80 seconds we will get one false-positive alarm. Since seizures differ in frequency from less than once per year to multiple times per day, this false-positive rate is extremely high. In Section 3.5, an interpretable approach

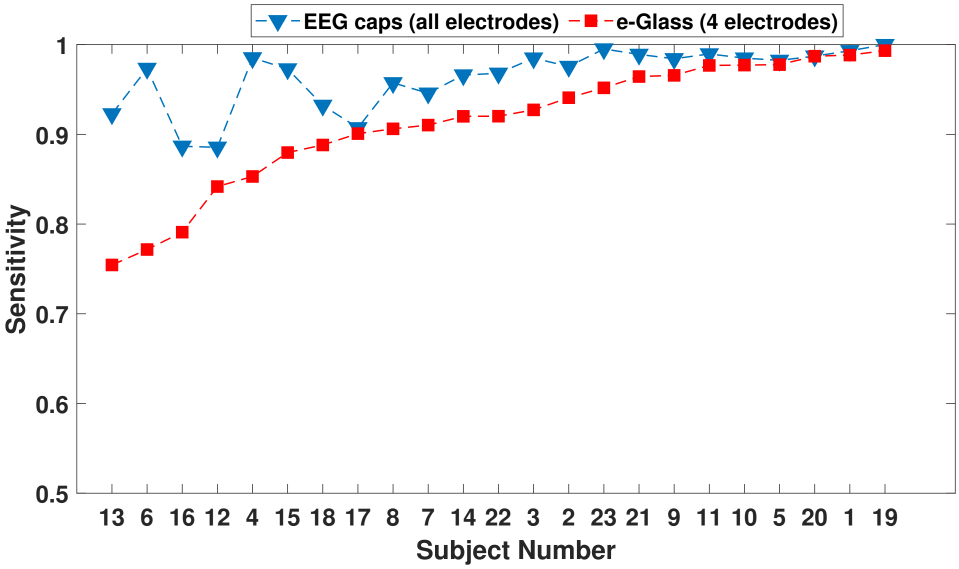

Figure 3.8: Sensitivity (sensitivity) for personalized approach using EEG caps (all electrodes) versus e-Glass (four selected electrodes)

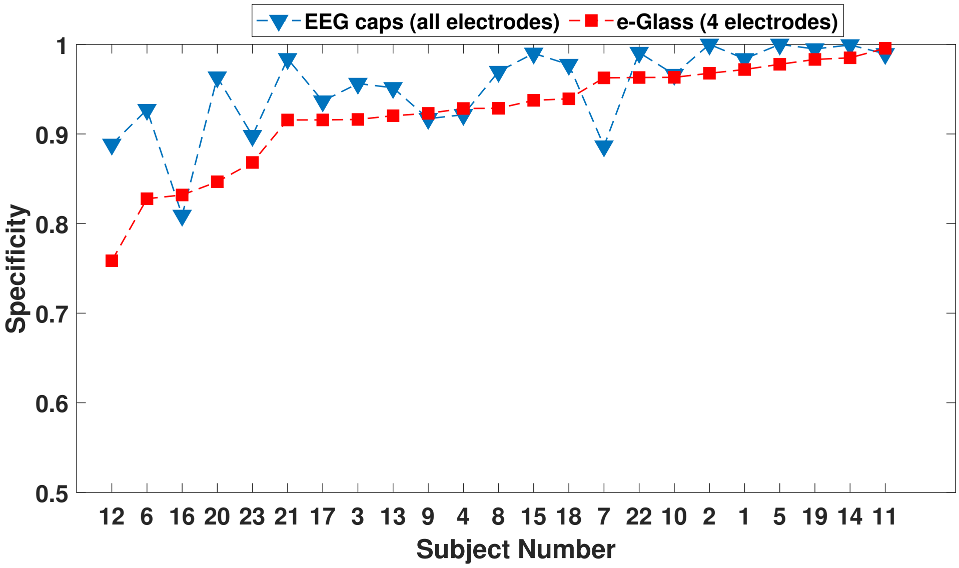

Figure 3.9: Specificity (specificity) for personalized approach using EEG caps (all electrodes) versus e-Glass (four selected electrodes)

to false alarm reduction for long-term epileptic seizure detection is proposed.

Energy Consumption and System Battery Life Analysis: Assuming that the EEG acquisition circuit is active all the time, the proposed method for epileptic seizure detection runs every four seconds on e-Glass system. The processing of a four-second window takes 3.08 seconds, which represents the latency of the system. Therefore, the

CPU duty cycle of e-Glass is 77%. This results in 65.15 hours of operation on a single battery charge. Thus, it allows for 2.71 days of continuous operation.

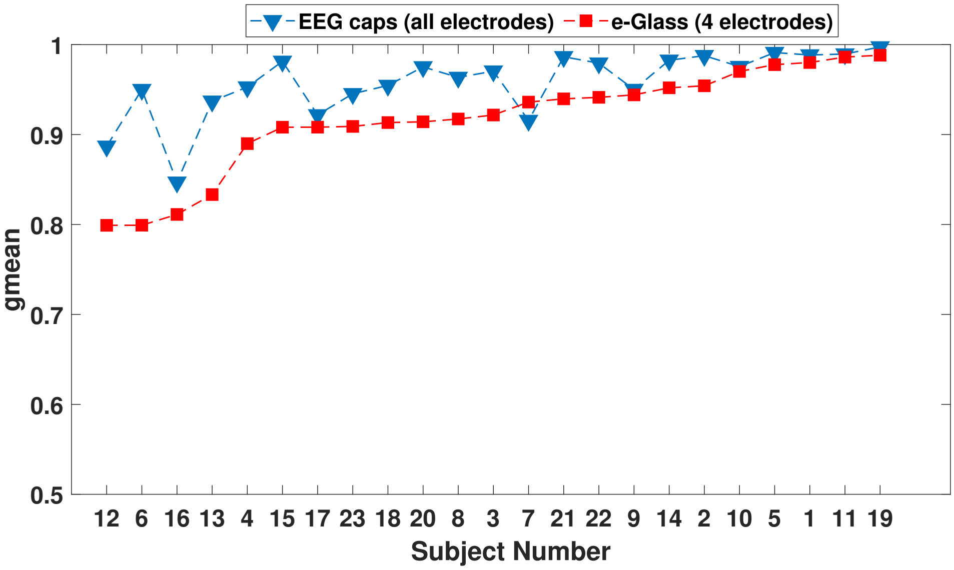

Figure 3.10: Geometric mean (G_{mean}) for personalized approach using EEG caps (all electrodes) versus e-Glass (four selected electrodes)

3.5 False Alarm Reduction for Long-Term Seizure Detection

Many researchers have tried to develop automatic seizure detection algorithms that involve only the analysis of EEG. The main pitfall of these EEG-based algorithms is the reported prevalence of false-positive alarms that hinders their effectiveness in long-term patient monitoring (Xu et al., 2016). Most of these algorithms are based on a set of predefined features extracted from EEG signals that are sent to the input of a trained classifier that distinguishes seizures from non-seizure activities, as shown in Section 3.3. The same approach is employed in (Hopfengärtner et al., 2014), where the authors propose an automatic epileptic seizure detection algorithm based on the frequency domain analysis. In particular, once the selected features have been extracted, the authors use an adaptive threshold technique to identify seizures, reaching a sensitivity of 87.3% and a false-positive rate of 0.22/h. Another study that uses a hybrid epileptic seizure detection algorithm combining the temporal and frequency domain analysis has been conducted in (Fürbass et al., 2015), resulting in a sensitivity of 81% and a false-positive rate of 0.30/h. However, these high false-positive rates place a significant burden on the healthcare infrastructure, and therefore, limit the application of these algorithms within the medical community.

Apart from EEG signals, other biosignals in combination with accelerometer can be used to detect epileptic seizures. One of the examples is the Embrace device (EMPATICA, 2020), a wrist-worn device that uses electrodermal activity along with a three-axial accelerometer to detect generalized tonic-clonic seizures (GTCS). During the clinical trail on 141 patients, the algorithm running on this device managed to detect 98% of seizures with a false alarm rate of 0.94 per 24h. Nevertheless, since the frequency of seizures for some patients ranges from less than once per year to multiple times per day, this false-positive rate is still high for certain patients. Moreover, the use of this device is strictly limited to the detection of GTCS.

The main inspiration behind the method proposed in this section comes from the approach of neurologists who try to find a set of similarly occurring morphological patterns that are likely to be seen within each seizure. Let us call this set a personalized seizure signature. Furthermore, let us hypothesize that all seizures of each subject either have a similar signal morphology or can be split into different seizure groups, where seizures with a similar morphology belong to the same group. Each of these groups can be detected using at least one of the morphological patterns of the seizure signature. The seizure signature consists of different EEG signal patterns tailored to each patient and simultaneously taken from the same seizure. These segments are chosen from the set of available EEG signal channels, by visually inspecting the signal morphology across different EEG channels from two different seizures, taking into account the signal quality. Finding similar signal patterns, also known as motif discovery in the literature, has been one of the most important data mining tasks (Patel et al., 2002; Chiu et al., 2003).

The purpose of this work is to present an interpretable patient-specific EEG-based approach for long-term epileptic seizure detection focused on the reduction of false-positive alarms. The goal is to assess to what extent personalized similarly occurring seizure patterns can be used to detect epileptic seizures. Furthermore, the identification of these patterns can potentially reveal the presence of seizures that were not annotated in the databases, as shown in Subsection 3.6.2.

3.5.1 Datasets

The Physionet.org CHB-MIT Scalp EEG database described in Section 3.4.1 along with the European Epilepsy Database (surface recordings) (Ihle et al., 2012) are used in this study to demonstrate the performance of the proposed approach. The European Epilepsy Database (surface recordings) contains a total of over 4600 hours of continuous recordings obtained from 30 people in the age range from 13 to 67. Seizure onsets and offsets for each patient are provided in separate text files. The European Epilepsy Database contains subclinical seizures for some patients. However, these seizures are not taken into consideration in this work, as more than 94% of these seizures lasted for less than 5 seconds, and the majority of these annotations are missing (Ihle et al., 2012). Therefore, for the European Epilepsy Database, only seizures with onsets and offsets determined by EEG are considered. EEG signals in both databases are sampled at $f_s = 256$Hz.

3.5.2 Personalized Seizure Signature

We define a personalized seizure signature S as follows:

$$S := \{p_1, p_2, ..., p_N\},$$

in which each p_i represents one unique seizure pattern. The number of selected patterns N is patient-dependent. The main motivation behind using multiple seizure patterns p_i lies in having different groups of seizures. Then, seizures that belong to the same group have similar morphological signal segments and can be detected using the same set of EEG signal channels that constitute the selected seizure pattern p_i. Individual seizures can be detected with more than one seizure pattern. Seizure patterns p_i are manually chosen by finding similarly occurring EEG signal segments from two different seizures. In order to capture the abnormal synchronous electrical discharge of the brain cells that occurs at the time of a seizure and is reflected onto various EEG channels, each pattern p_i is patient-specific and is represented by a $2 \times M$ matrix that consists of two different EEG channels, namely:

$$p_i := \begin{bmatrix} p_{i_1}^{(1)} & p_{i_2}^{(1)} & \dots & p_{i_M}^{(1)} \\ \\ p_{i_1}^{(2)} & p_{i_2}^{(2)} & \dots & p_{i_M}^{(2)} \end{bmatrix}$$

Each row of this matrix represents one of the chosen EEG channels. The duration of each pattern is empirically obtained and it ranges from one to ten seconds, i.e.,

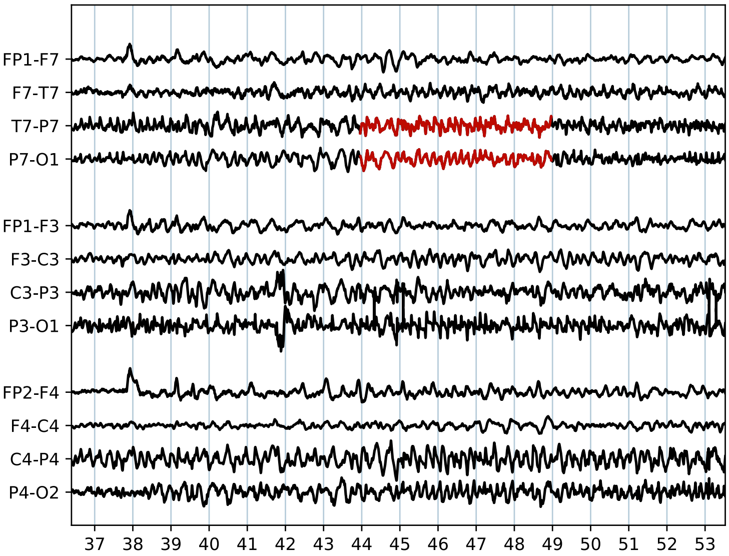

(a) Recording chb02_16.edf, 14 seconds after seizure onset.

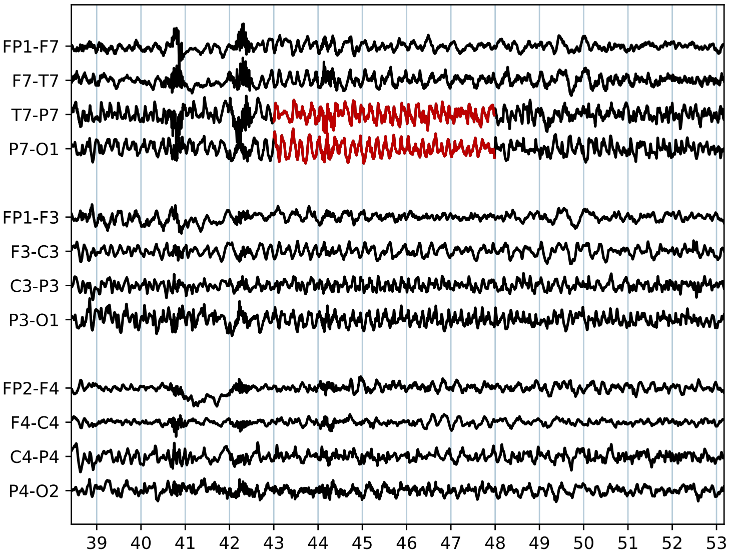

(b) Recording chb02_16+.edf, 13 seconds after seizure onset.

Figure 3.11: Two ictal EEG recordings taken from CHB-MIT Scalp EEG database. After the visual inspection of these two seizures, a five-second long seizure pattern p_1 consisting of channels T7-P7 and P7-O1 in Fig. 3.11a is chosen, as shown in red. Seizure pattern p_1 constitutes the personalized seizure signature S of this patient, i.e., $S = \{p_1\}$. A similar seizure pattern can be found in Fig. 3.11b, shown in red.

$f_s \leq M \leq 10 \cdot f_s$, where f_s represents the EEG sampling frequency. EEG signal channels $p^{(1)}_{i_k}$ and $p^{(2)}_{i_k}$, where $k = \{1, ..., M\}$, are chosen simultaneously from the same seizure. The aforementioned definitions are illustrated using the example shown in Fig. 3.11. This figure illustrates an example of a seizure signature that consists of only one seizure pattern, i.e., $S = \{p_1\}$.

Even though in most cases the personalized signature consists of only one seizure pattern, sometime more than one pattern is needed to ensure the complete removal of false positives. For instance, let us consider seizures of subject chb13 in CHB-MIT database, which is shown in Fig. 3.12. In order to detect all 12 seizures of this subject, we use the seizure signature $S = \{p_1, p_2\}$ comprised of the following two seizure patterns: [FP1F7, FZCZ] and [FP1F7, FP2F4]. The former is extracted from the first seizure allowing the detection of seizures [1, 2, 4, 5, 8, 11, 12], whereas the latter is taken from the third seizure resulting in a detection of seizures [3, 6, 7, 8, 9, 10, 12]. Seizures [8, 12] of this patient can be detected with any of the two aforementioned patterns. Nevertheless, the rest of the seizures seems to belong to two different groups of morphological patterns.

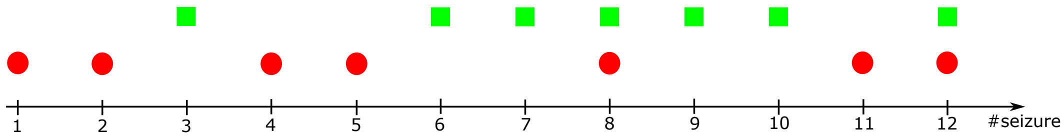

Figure 3.12: Distribution of detected seizures in subject chb13 from CHB-MIT database using a seizure signature that consists of two different patterns. Red circles represent seizures detected using the first pattern, whereas the green circles show those that are detected using the second one.

Let us now examine patient chb06 in CHB-MIT database who experienced 10 seizures. Our approach uses three different seizure patterns i.e. $S = \{p_1, p_2, p_3\}$. Namely, patterns [C3P3, T7FT9] and [F3C3, C3P3] taken from seizure 1, and [F3C3, C3P3] taken from seizure 2. Using these three seizure patterns, our approach detects the following seizures [1, 6, 7, 10], [1, 3, 4, 10], and [2, 4, 5, 8, 9], respectively. Even though patterns p_2 and p_3 consist of the same EEG channels, their signal morphologies are completely different. As it can be seen from this example as well, some seizures can be detected with more than one pattern. We found that the maximum number of patterns within the seizure signature for the considered databases is three.

3.5.3 Real-Time Flow for the Detection of Epileptic Seizures

After a personalized seizure signature $S = \{p_1, p_2, ..., p_N\}$ has been chosen, the similarity between each seizure pattern p_i of length M and a signal segment of the same length is estimated taking into account only the EEG channels present in S. First, both the observed signal segment and each of the seizure patterns, are normalized by removing the mean value of their EEG channels. Then, the similarity is estimated by minimizing the distance between the selected signal segment and each seizure pattern. Dynamic time warping (DTW) (Berndt and Clifford, 1994) is used as the underlying distance metric. The other most commonly used distance metric is Euclidean distance (Mueen et al., 2009). However, in this work DTW is used, allowing similarly occurring morphological segments to be out of phase in the time axis (Keogh and Ratanamahatana, 2005). More precisely, Euclidean distance assumes the temporal alignment of the considered morphological segments and is very sensitive to small distortions in the segment shape. On the other side, DTW takes these distortions into consideration by aligning the signal segments before calculating the distance measure.

Algorithm 2 Distance metric calculation

```
function CALCULATEDISTANCE($S, EEG$)
    $\overline{S} = \{\overline{p_1}, \overline{p_2}, ..., \overline{p_N}\} \leftarrow$ MEANREMOVAL($S$);
    for $i = 1$ to $N$ do
        $M \leftarrow$ LENGTH($p_i$); $p_{i_1} \leftarrow p_{i_{1k}}$; $p_{i_2} \leftarrow p_{i_{2k}}$
        $ch_1 \leftarrow$ FIRSTEEGCHANNEL($p_i$); $ch_2 \leftarrow$ SECONDEEGCHANNEL($p_i$)
        $s_1 \leftarrow EEG(ch_1, t : t+M)$; $s_1 \leftarrow$ MEANREMOVAL($s_1$); $D_{i_1} = \mathrm{DTW}(p_{i_1}, s_1)$
        $s_2 \leftarrow EEG(ch_2, t : t+M)$; $s_2 \leftarrow$ MEANREMOVAL($s_2$); $D_{i_2} = \mathrm{DTW}(p_{i_2}, s_2)$
        $D_i = \log(D_{i_1}) \cdot \log(D_{i_2})$
    end for
end function
```

Let p_i be a seizure pattern of length M consisting of two EEG channels $p_i^{(1)} = p_{i_k}^{(1)}$ and $p_i^{(2)} = p_{i_k}^{(2)}$. We denote the value of DTW between the first EEG segment $p_i^{(1)}$ and a signal segment of length M by $D_i^{(1)}$. Similarly, for the second EEG segment in the observed pattern this value is denoted by $D_i^{(2)}$. For each signal window of length M and each seizure pattern p_i in S, we minimize the following distance metric D_i:

$$D_i = \log(D_i^{(1)}) \cdot \log(D_i^{(2)}), 1 \leq i \leq N.$$

The calculation of this metric is based on Algorithm 2. Note that parameter t in Algorithm 2 represents the starting point of the observed signal segment. In order to detect seizures across the entire duration of available recording, we use a sliding window of length M with a step of 1 second. This is done by making parameter t go from the beginning of the recording to its end. The last step of the flow consists of finding a threshold that allows us to detect as many seizures as possible without false positives. We manually determine the value of each threshold h_i for each value of the distance metric D_i across the entire signal recording. Fig. 3.13 shows an example of D_i. All D_i values below the threshold represent seizure occurrences. In order to detect new seizures, our method inspects only EEG channels present in each seizure pattern of the seizure signature. As soon as the observed signal segment resembles one of the seizure patterns, a new seizure is detected, making our method highly interpretable.

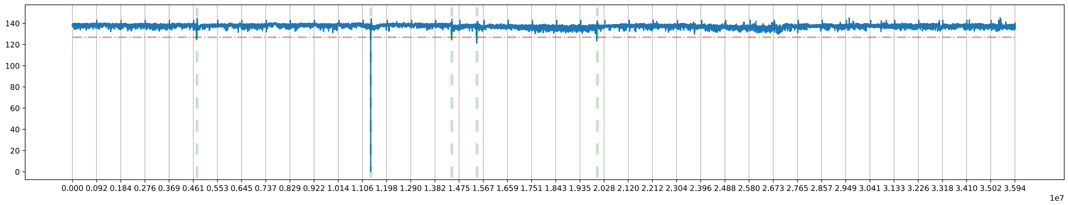

Figure 3.13: The value of D_i obtained during 39 hours of continuous patient monitoring (chb05 from CHB-MIT database). In this example, we use a seizure signature S that consists of only one seizure pattern p_i, i.e., $S = \{p_1\}$, taken from the second seizure. This can clearly be seen from this figure, as the value of D_i reaches its global minimum (solid line) during the second seizure. Each of the vertical dashed lines corresponds to the times of seizure occurrences. The dash-dot horizontal line shows the value of the applied threshold $h_i = 125$ that distinguishes seizures from non-seizure events. As shown in this figure, this patient had five seizures and all of them are detected, with no false positives.

3.5.4 Evaluation Metrics

The standard evaluation metrics commonly used for the evaluation of seizure detection approaches are: sensitivity, false alarm rate, and detection latency (Beniczky and Ryvlin, 2018). To assess the performance of the proposed approach in terms of the maximum number of seizures that can be detected without false-positive alarms, the main evaluation metric considered in this work is sensitivity, defined in Section 2.4.4. Moreover, the detection latency of the approach is reported as time in seconds from the seizure onset to the detection time.

3.6 Results

The overall performance of the proposed approach is shown in Fig. 3.14. Namely, each vertical bar represents the sensitivity obtained across the entire duration of available EEG recordings for each patient. As we can see in Fig. 3.14a, the proposed approach reaches a full sensitivity of 100% for 19 subjects of CHB-MIT databases with no false positives. Furthermore, a personalized seizure signature that consists of only one seizure pattern was used for more than 70% of subjects (17 subjects). A seizure signature composed of two different seizure patterns, i.e., $S = \{p_1, p_2 \mid N = 2\}$, was only needed for five patients, whereas only for two subjects three seizure patterns were used to ensure an acceptable sensitivity. On the other side, the use of personalized

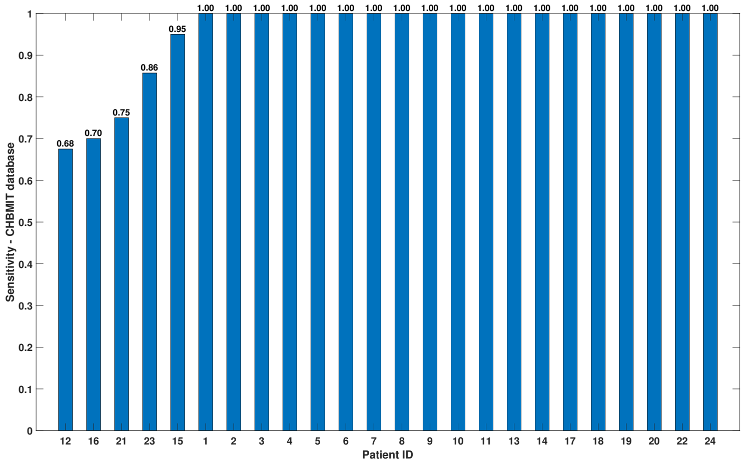

(a) CHB-MIT Database.

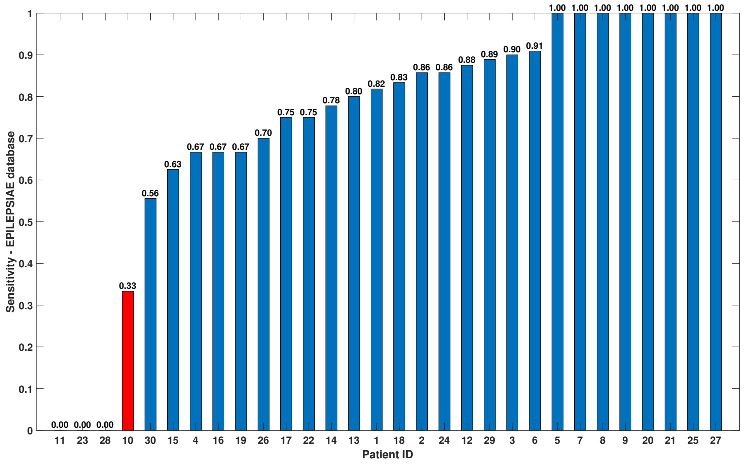

(b) European Epilepsy Database.

Figure 3.14: False-alarm free sensitivity of the proposed approach.

seizure signatures for each patient demonstrates a false alarm-free detection with a sensitivity of no less than 70% per subject achieved for 70% of subjects of European Epilepsy Database. The use of three patterns was only required for two patients of this database. The number of patterns used for each subject is detailed in Appendix A. The proposed method fails to detect seizures for patients 11, 23, 28, whereas for patient 10 the obtained sensitivity is below 50%. The limitations of this approach are thoroughly explained in Subsection 3.6.1.

Detection latency results for both databases used in this study are shown in Fig. 3.15 in a form of a violin plot. Each shape in Fig. 3.15 represents the distribution of the measured detection latency for each patient. Moreover, the white dot inside each of these shapes is the median value, whereas the black bar in the center indicates the interquartile range. Data points shown within each shape represent the measured latency of each seizure. These results reveal that more than 95% of all seizures in CHB-MIT Database are detected with a latency below 40 seconds. The measured latency in case of European Epilepsy Database is higher allowing the detection of more than 70% of overall seizures in less than 40 seconds. The position of the selected seizure signature within each seizure affects the measured detection latency. High detection latency in Fig. 3.15 obtained for few seizures of patients 5, 13, 15, 17, 24 in CHB-MIT Database and 3, 5, 16 in European Epilepsy Database shows that the chosen seizure signature does not appear in the first 40 seconds of the seizure. Therefore, the detection of the seizure signature is delayed.

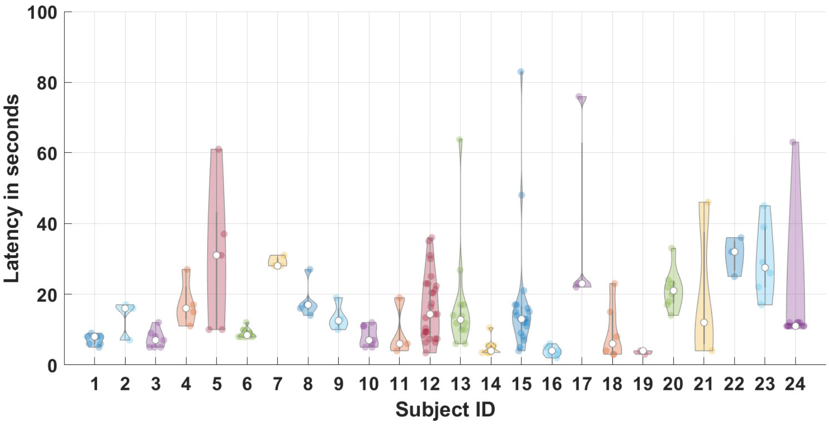

(a) CHB-MIT Database.

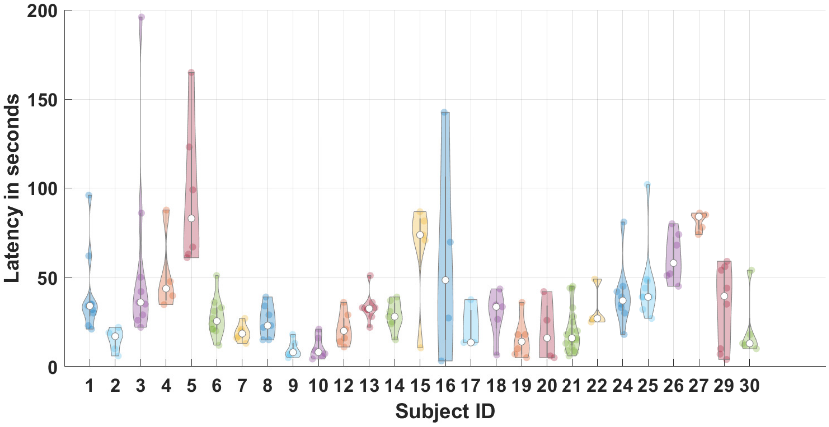

(b) European Epilepsy Database.

Figure 3.15: The measured detection latency of the proposed approach per patient in seconds.

3.6.1 Limitations of the proposed approach

There are a few cases in which the proposed method either does not reach a full sensitivity or it fails to detect epileptic seizures. These cases are listed below:

1. Short seizures - The duration of seizures differs greatly between patients. In order to find seizure patterns within each seizure, the duration of each selected seizure patterns p_i within S should be shorter than the duration of each seizure. Furthermore, short seizures that do not develop entirely exhibit the absence of the chosen seizure patterns, and therefore, cannot be detected using our approach.

2. Artifact - Seizures that are completely covered by artifacts caused by muscular movements are hard to be detected using our approach. In fact, this artifact is seen across all of the available EEG channels, which impedes the identification of the personalized seizure signature S.

3. Seizures that are not visible on scalp EEG - Our approach tries to replicate the work of neurologists by looking for similarly occurring scalp EEG morphological pattern p_i within each seizure. However, for some patients, no epileptic discharges can be seen on scalp EEG. Therefore, to capture these seizures, another neuroimaging techniques are needed.

4. Pattern absence - The absence of selected seizure pattern p_i might be seen in some rare cases. We look for seizure patterns by visually inspecting the EEG signal morphology from two different seizures. However, in case of lack of at least two seizures coming from the group with similar morphological segments, no seizure pattern can be identified.

3.6.2 Unlabelled seizures

One of the interesting findings of this approach is that it allows us to discover the existence of seizures that were not labelled in the databases. As previously mentioned, a threshold h_i for each seizure pattern p_i is manually selected by visually inspecting the morphology of D_i, shown in Fig. 3.13. All D_i values below the value of the selected threshold represent epileptic seizure occurrences. By analyzing D_i values of each patient in both databases, some values of non-seizure events were below the selected threshold. After a careful review of these cases by expert neurologists, two subjects that most likely contain unlabelled seizures were found: subject chb24 from CHB-MIT database and subject 308102 from European Epilepsy Database. In particular, the seizure signature of subject chb24 is extracted from seizure 1 and consists of only one seizure pattern [F4C4, FZCZ] of length 10 seconds, which is shown in black in Fig. 3.16. After the seizure signature has been chosen, the value of D_i is estimated across the entire duration of available signal recording for this subject. The value of D_i is shown in Fig. 3.17. This subject had 16 annotated seizures, which are represented by vertical red lines in this figure. After applying the threshold $h_i = 160$, we can clearly notice four non-seizure events for which the value of D_i falls below the threshold. The value of the threshold is chosen to maximize the sensitivity of the proposed method. Fig. 3.18, 3.19, 3.20, and 3.21 show EEG signal channels of these non-seizure events. It is clear that the chosen signature appears in these four non-seizure events. In case of subject 308102 from European Epilepsy Database, we found one non-seizure event that allows us to detect epileptic seizures of this patient using only one seizure pattern. Therefore, these non-seizure events were treated as seizures in Section 3.6.

Considering the fact that epileptic seizures may occur at any moment in time, long-term patient monitoring requires the constant presence of physicians who would look for seizure occurrences. This is a very time-consuming task due to a large number of hours in signal recordings. EEG signal recordings have been used as the gold standard technique for long-term monitoring of epileptic patients in hospitals. Nevertheless, physicians are forced to look at all of the available EEG signal channels to find changes in the signal morphology rendering long-term patient monitoring extremely tiresome. The proposed approach is a suitable tool to reduce the workload of hospital physicians providing a subset of available EEG channels that should be inspected to find epileptic seizures. Furthermore, apart from lowering the number of necessary EEG channels for inspection, this approach also provides the exact time location of detected seizures. Additionally, the use of personalized signatures may also reveal the presence of unlabelled seizures, which confirms the usefulness of this approach for the analysis of long-term seizure monitoring.

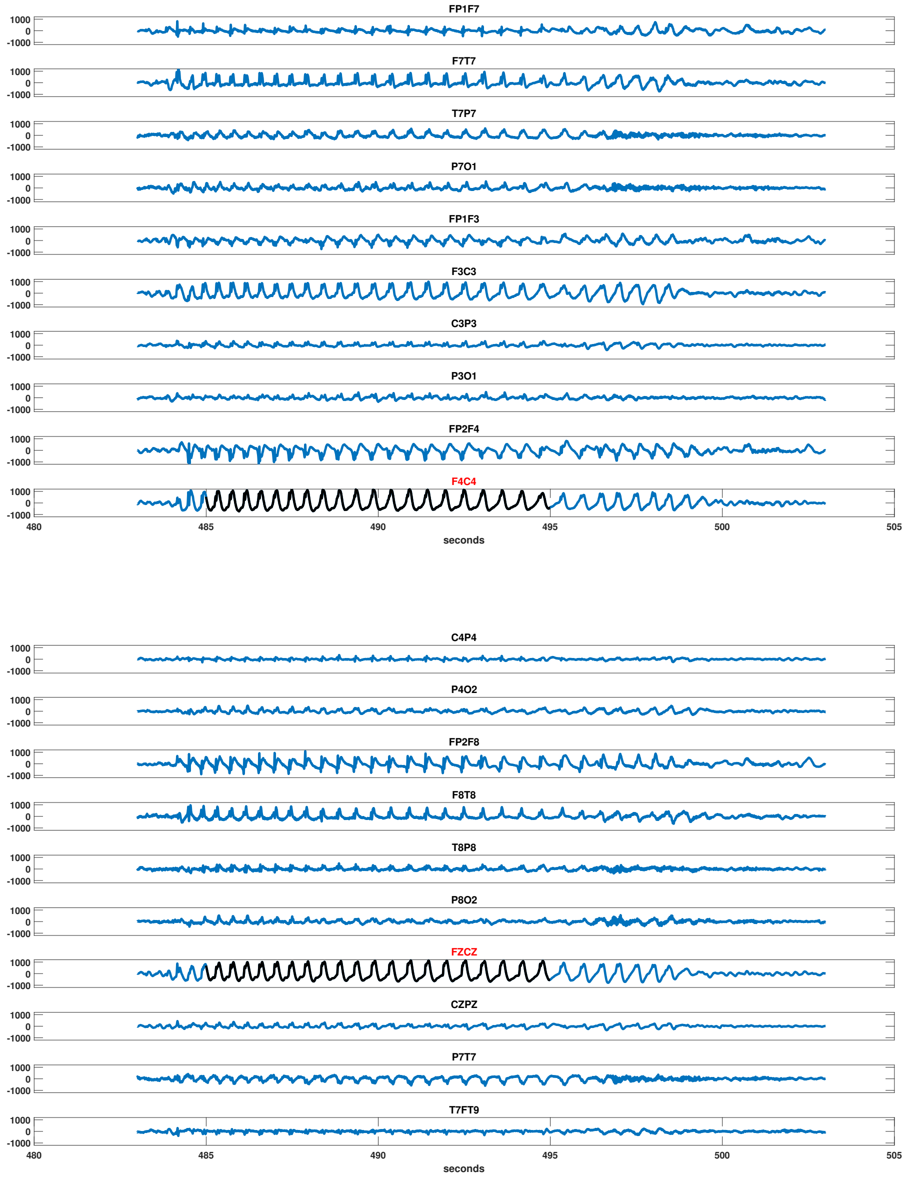

Figure 3.16: The selected seizure signature for subject chb24 from CHB-MIT database extracted from recording chb24_01.edf. The chosen signature consists of only one pattern of length 10 seconds, i.e., $S = \{p_1\}$, taken from the first seizure. The chosen EEG channels are shown in black

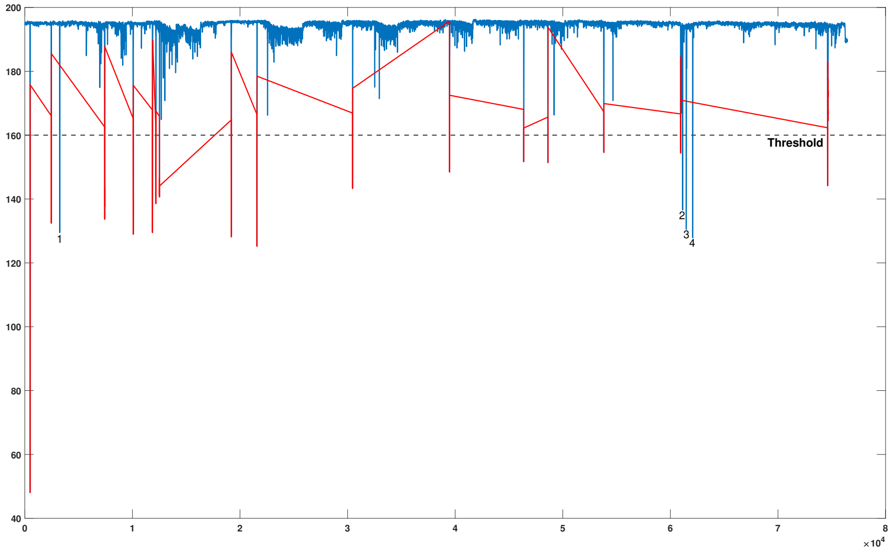

Figure 3.17: The value of D_i obtained during 21 hours of continuous patient monitoring (chb24 from CHB-MIT database). The annotated seizure occurrences are shown in red. Since the seizure signature is extracted from the first seizure, the value of D_i reaches its global minimum during the first seizure. The dash-dot horizontal line indicates the applied threshold $h_i = 160$ for seizure detection. Events annotated by numbers 1, 2, 3, 4 indicate the presence of unlabelled seizures, as their D_i falls below the selected threshold.

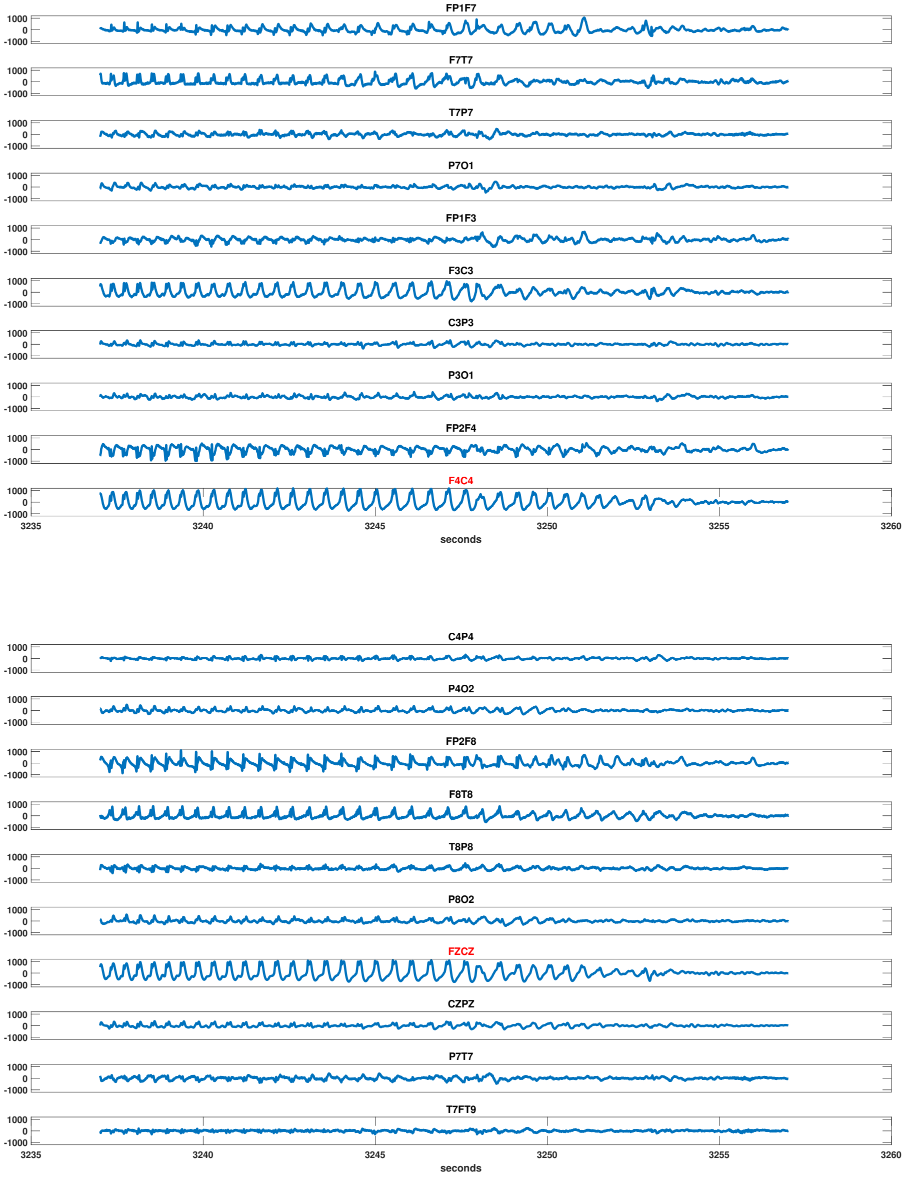

Figure 3.18: Unlabelled seizures 1 in recording chb24_01.edf.

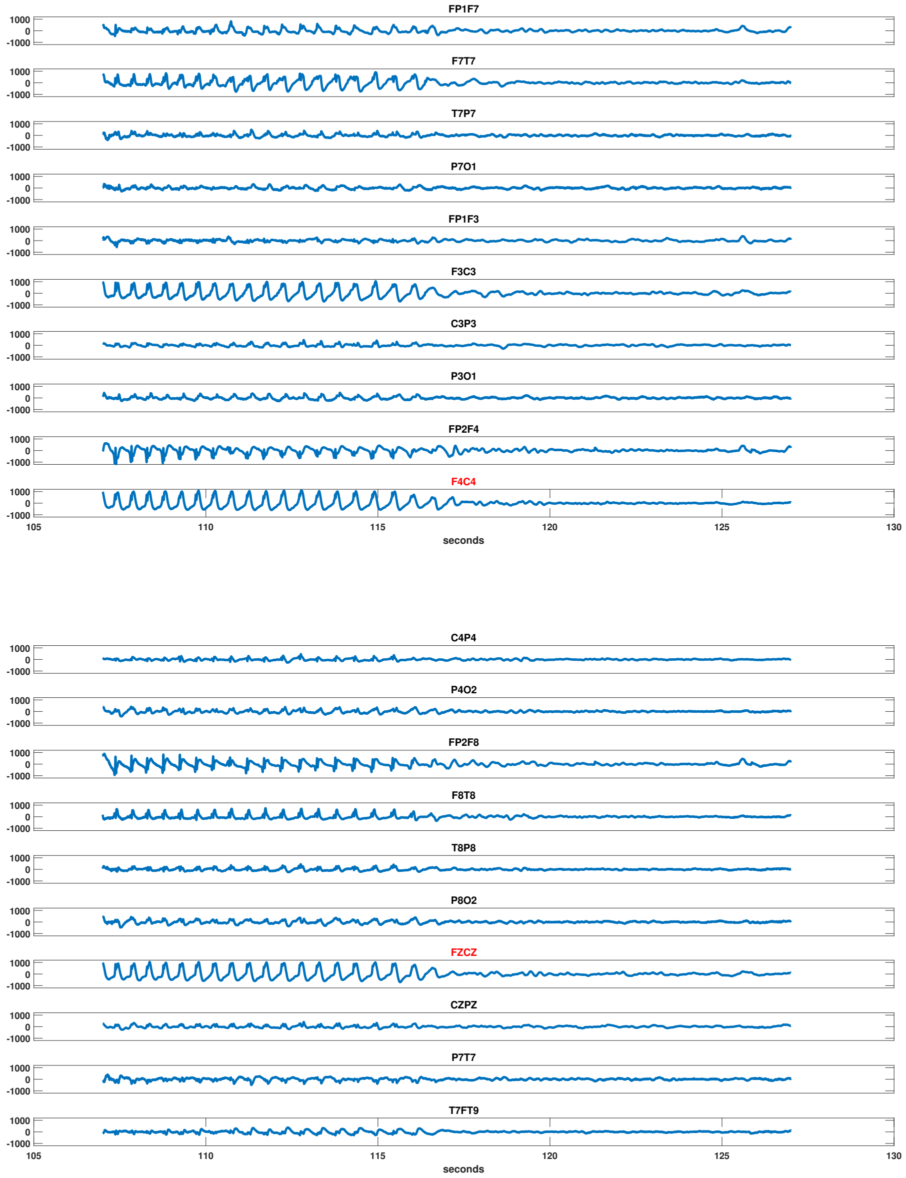

Figure 3.19: Unlabelled seizures 2 in recording chb24_18.edf.

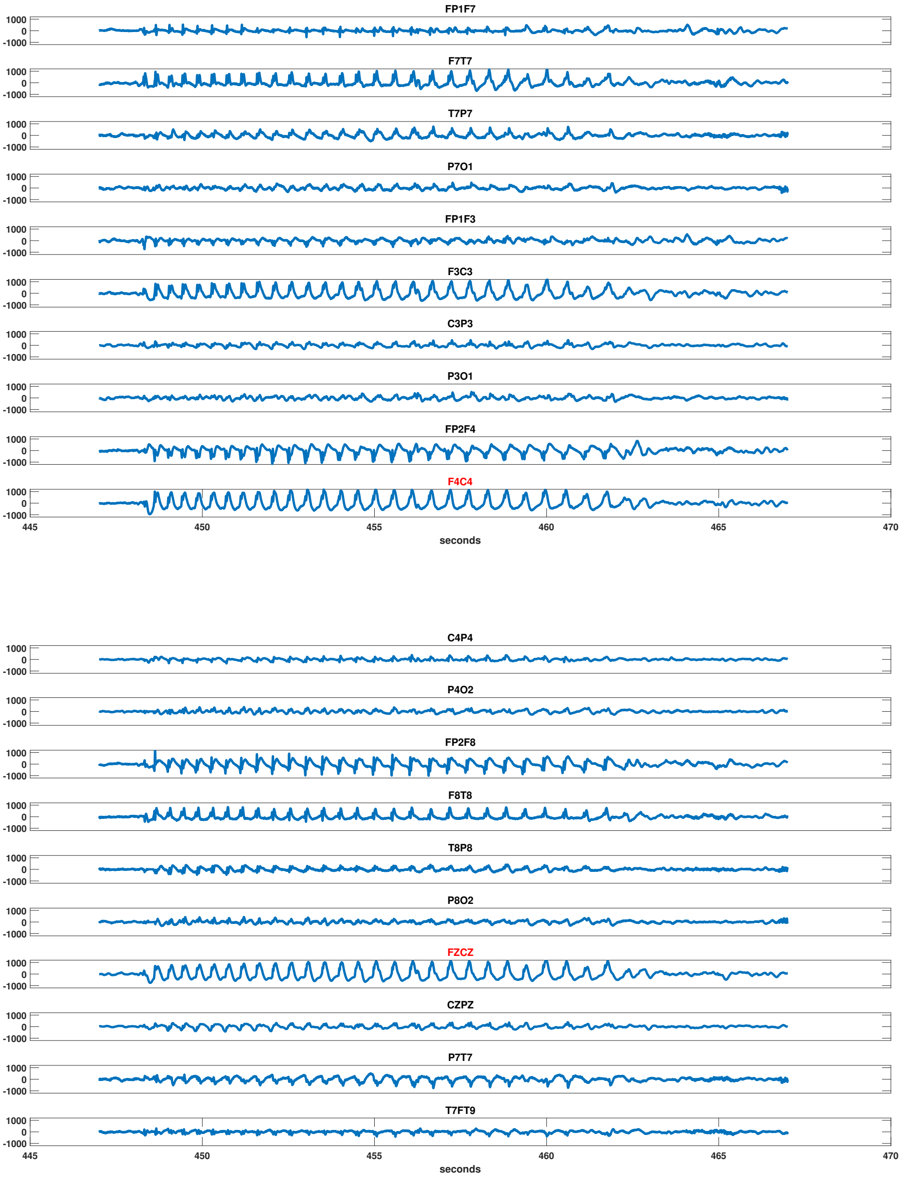

Figure 3.20: Unlabelled seizures 3 in recording chb24_18.edf.

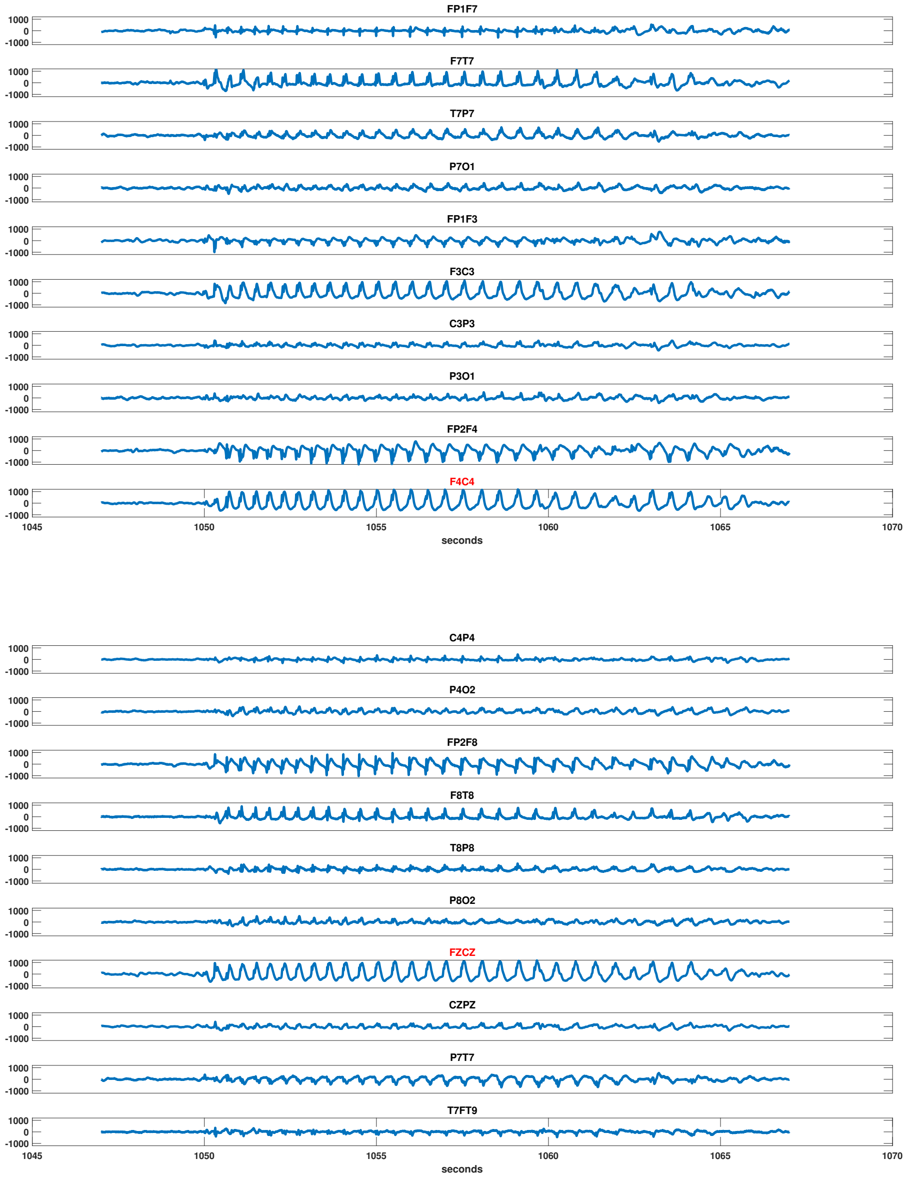

Figure 3.21: Unlabelled seizures 4 in recording chb24_18.edf.

4 Conclusions and Future Work

THIS chapter summarizes the conclusions of my research outlining my main contributions along with the proposed future work. The main focus of my thesis is set on the monitoring of cardiovascular and neurological diseases using ubiquitous wearable technologies. Cardiovascular diseases considered in Chapter 2 include Atrial Fibrillation (AF) and Myocardial Infarction (MI). Both, AF and MI, are commonly detected by inspecting changes in the Electrocardiogram (ECG) morphology, which is used as the main biosignal for detection of these diseases in this thesis.

The part of neurological disorders targets the detection of epileptic seizures through the use of Electroencephalogram (EEG). The first part of Chapter 3 presents a real-time method for epileptic seizure detection using a reduced set of EEG electrodes. The last part of Chapter 3 focuses on reduction of false-positive alarms in long-term epileptic seizure detection.

4.1 Atrial Fibrillation

One of the problems I have addressed in this thesis is detection of AF from a short single lead ECG recording. I have proposed a hierarchical heart-rhythm classification method that has been trained on four different classes of ECG recordings, which include ECG signals coming from normal sinus rhythm (NSR), AF, other types of cardiac rhythms (OthR), and noisy recordings. The proposed method consists of three main steps: pre-processing, feature extraction, and classification step. The pre-processing step is used to remove the baseline wander and high frequency noise. Extracted features capture the oscillations in heart rate (HR), T- and P-wave morphology, as well as the time and frequency domain ECG behaviour. The classification step incorporates two different classifiers: a multiclass classifier based on error-correcting output codes (ECOC) and a random forest classifier for binary decision making. In case that ECOC cannot distringuish between NSR and OthR recordings, random forest is applied. The experimental evaluation demonstrates the robustness of the proposed technique with an F1 score of 80% obtained on the hidden test set of the 2017 PhysioNet/CinC Challenge.

The proposed heart-rhythm classification method assumes that the ECG segment at the input is not inverted. However, as discussed in (Clifford et al., 2017), many ECG signals were inverted. The integration of the lead inversion check has the potential to improve the classification performance of the proposed method. Furthermore, the selected set of features can be further reduced through the use of feature selection algorithms, which could lower the computational complexity of the proposed method. The reduction in computational complexity, in turn, makes the proposed algorithm more suitable to run on wearable devices. Thus, one of the future lines of work is to port the proposed technique on a wearable device and to estimate its energy consumption and battery life.

List of publications:

- **D. Sopic**, E. De Giovanni, A. Aminifar and D. Atienza, Hierarchical cardiac-rhythm classification based on electrocardiogram morphology, 2017 Computing in Cardiology (CinC), pp. 1-4, 2017.

4.2 Myocardial Infarction

A considerable portion of government health-care spending is allocated to the continuous monitoring of patients suffering from MI. Wearable devices present a cost-effective means of monitoring patients' vital signs in ambulatory settings. However, a major challenge is to design such ultra-low energy devices for long-term patient monitoring. In Section 2.5, I have tackled the problem of early detection and prediction of MI using smart wearable systems. The proposed real-time event-driven classification technique uses a hierarchical classifier with multiple levels. Each level is based on the random forest classification scheme that uses a confidence-related decision-making process to select the classifier that will be invoked. The main goal of this technique is to reduce the energy consumption of smart wearable systems while maintaining a high classification accuracy. Hence, the proposed technique is general and can be applied to other pathological conditions that are meant to be detected through the use of smart wearable devices. Moreover, the analysis of computational complexity and energy efficiency of the proposed technique along with the design flow presented in Sections 2.8 and 2.9 allow users to synthesize high-accuracy event-driven hierarchical classifiers that meet their battery life requirements. The event-driven classification technique is evaluated on the MI database (Physiobank - PTB Diagnostic ECG database (Goldberger et al., 2000)) and further ported on a real wearable device. The experimental evaluation demonstrates that this technique outperforms the existing approaches in terms of energy consumption and battery life by a factor of 2.60, with no classification quality loss.

As mentioned in Section 2.8, parameter K represents the number of features used in the first level classifier and is used by the designer to make a trade-off between the classification accuracy performance of the system, its energy efficiency, and the complexity of design space exploration. In case of MI, the number of features used in the first level classifier was fixed to $K = 5$. In the future, I am planning to optimize this parameter through its integration in Algorithm 1. Additionally, the proposed event-driven technique uses a hierarchical classifier with multiple levels, each of which is based on the random forest algorithm. Therefore, one of the future lines of this work is to see the impact of another classification scheme on the obtained performance. Furthermore, since the proposed technique is not bounded to the case of MI, in the future, I am planning to apply this technique to other pathological conditions, such as AF and epilepsy.

List of publications:

- **D. Sopic**, A. Aminifar, A. Aminifar and D. Atienza, Real-time classification technique for early detection and prevention of myocardial infarction on wearable devices, 2017 IEEE Biomedical Circuits and Systems Conference (BioCAS), pp. 1-4, 2017.
- **D. Sopic**, A. Aminifar, A. Aminifar and D. Atienza, Real-Time Event-Driven Classification Technique for Early Detection and Prevention of Myocardial Infarction on Wearable Systems, in IEEE Transactions on Biomedical Circuits and Systems, pp. 982-992, 2018.

4.3 Real-Time Method for Epilepsy Detection

The gold standard technique for epileptic seizure detection uses EEG head caps that require a large number of electrodes to be placed on the patient's scalp. The lack of portability and comfort of these caps limits the possibility for long-term and reliable patient monitoring in an ambulatory setting. Furthermore, due to the stigma associated with EEG caps, the majority of epileptic patients refuse to wear them.

As one of my contributions, I have presented a real-time method for epileptic seizure detection that uses EEG signals acquired from two electrode pairs: $F_7 T_3$, and $F_8 T_4$. The experimental evaluation of this method on CHB-MIT Scalp EEG database (Goldberger et al., 2000; Shoeb, 2009) demonstrates that the personalized approach outperforms the generic one in terms of classification performance reaching a sensitivity of 90.98% and a specificity of 92.10%. The proposed approach is ported on a wearable ultra-low energy device in which the two electrode pairs are integrated in the temples of eyeglasses, allowing for 2.71 days of operation on a single battery charge and ensuring a high degree of wearability. This reduced set of electrodes overcomes the lack of portability of hospital equipment, while reducing the computational complexity, which further leads to a reduction in energy consumption. The used wearable device onto which the proposed approach is ported, represents an inconspicuous system that could enable patients to avoid the aforementioned social stigma of wearing EEG head caps. Moreover, this device can provide an early warning of epileptic seizures and promptly inform patient family members of preventive measures to avoid possible accidents during seizures and epilepsy-related death. Overall, this device can significantly contribute to improvements in the patient's quality of life by reducing the socioeconomic burden of epilepsy.

This method has been further improved and used in different studies. In (Zanetti et al., 2020), the authors propose a seizure detection methodology based on the edge computing paradigm and data fusion to improve the seizure detection robustness in terms of false alarm rate. The proposed data fusion approach combines two epochs of EEG to build a new set of features representing different seizure moments. This second set is taken from a randomly selected EEG epoch, which contributes to the increase of data variability in the training set. Thus, more informative features per target label are obtained on the double feature set, resulting in a more robust model with respect to the number of false positives. Using the same 570 mAh battery, the authors improve the current false alarm rate by 34.7%, achieving over 3 days of operation on a single battery charge.

Another study that uses the proposed method for epilepsy detection is described in (Pascual et al., 2019). In this study, the authors propose a self-learning methodology for epileptic seizure detection. Their methodology uses a novel algorithm for labeling seizures without medical supervision to generate the training data. As some of the features in Section 3.3.1 contained redundant information, the authors first use backward elimination in order to find the most relevant ones, which results in a subset of ten most informative features that offer a trade-off between the classification accuracy and complexity. The obtained subset of features includes: total theta band power, relative theta band power, and total delta band power from electrode F_7T_3, as well as relative theta band power, seventh level permutation entropy for $n = 5$ and $n = 7$, sixth level permutation entropy for $n = 7$, third level Renyi entropy and sixth level sample entropy for $k = 0.2$ and $k = 0.35$ from electrode F_8T_4. The authors demonstrate that the median label deviation from the ground truth is less than 1% of the signal length, which results in negligible loss in the classification performance.

Publication: **D. Sopic**, A. Aminifar and D. Atienza, e-Glass: A Wearable System for Real-Time Detection of Epileptic Seizures, 2018 IEEE International Symposium on Circuits and Systems (ISCAS), pp. 1-5, 2018.

Patent: **D. Sopic**, R. Zanetti, A. Aminifar, A. Aminifar and D. Atienza, A wearable system for real-time detection of epileptic seizures, Patent numbers: WO2019162850 (A1), P3264US00.

4.4 False Alarm Reduction in Epilepsy

As the main pitfall of automatic seizure detection algorithms remains their unacceptably high number of false-positive alarms, in the last part of my thesis, I have presented a patient-specific approach for long-term automatic epilepsy detection focused on avoiding false-positive alarms. This algorithm is based on the similar morphological EEG signal patterns that occur frequently during seizures, which makes it highly interpretable. The duration of these patterns is patient-specific and it goes from one to ten seconds. Seizure signature along with the value of each threshold used to distinguish seizures from non-seizure activities are obtained manually. In the future, the plan is to automate this procedure. The performance of the proposed approach has been evaluated using two public databases: the Physionet.org CHB-MIT Scalp EEG database (Goldberger et al., 2000; Shoeb, 2009) and the European Epilepsy Database (Ihle et al., 2012). The results on the CHB-MIT database demonstrate that it is possible to detect seizures of 87% of subjects reaching a sensitivity of over 85% per subject with no false-positive alarms. Moreover, on the European Epilepsy Database, the results show a false-positive-free sensitivity higher than 70% per subject. Additionally, this approach unveiled the existence of unlabelled seizures in both databases. Considering the irregular nature of epileptic seizures in long-term patient monitoring, this method can help physicians discover seizures by inspecting only the EEG channels of each pattern within the seizure signature along with the obtained time location of seizures.

The proposed approach demonstrates that similarly occurring morphological patterns are likely to be found within ictal parts of EEG signals for the majority of epileptic patients. The use of personalized seizure signatures eliminates false-positive alarms while ensuring a high detection sensitivity. Even though for the majority of cases the personalized signature contains only one seizure pattern, for some patients multiple patterns are required to reach a high false-positive-free sensitivity. Two examples of seizure signatures that consist of multiple seizure signatures are given in Section 3.5.2. Nevertheless, as it can be seen from these examples, some seizures are detected by more than one pattern. Thus, one of the future lines of work would be to try to combine these patterns to reduce the number of necessary patterns.

Another interesting point to investigate in the future is a temporal evolution and adjustment of the personalized seizure signature. As an interesting example, EEG recordings chb01 and chb21 (CHB-MIT database) were obtained from the same female subject one and a half years apart. This patient had seven seizures when she was 11 (chb01) and four more when she was 13 (chb21). However, the personalized seizure signature used for detecting seizures from chb01 recordings differs from the one used for chb21. Specifically, all seizures from chb01 can be detected using a 5-second long pattern [P4O2, P8O2], whereas in the case of chb21 we use a 2-second long pattern [P4O2, FT9FT10], resulting in the detection of three out of four seizures. Therefore, another area of future work concerns a time-domain evolution of personalized seizure signature using the data obtained at different moments in time.

A Appendix

Patient ID	Number of seizures	Recording duration in hours	Seizure duration in hours	Number of patterns
1	7	40.55	0.12	1
2	3	35.27	0.05	1
3	7	38.00	0.11	1
4	4	156.06	0.11	1
5	5	39.00	0.16	1
6	10	66.74	0.04	3
7	3	67.05	0.09	1
8	5	20.00	0.26	1
9	4	67.87	0.08	1
10	7	50.02	0.12	1
11	3	34.79	0.22	1
12	40	23.69	0.41	3
13	12	33.00	0.15	2
14	8	26.00	0.05	1
15	20	40.01	0.55	2
16	10	19	0.02	2
17	3	21.01	0.08	2
18	6	35.63	0.09	2
19	3	29.93	0.07	1
20	8	27.60	0.08	1
21	4	32.83	0.06	1
22	3	31.00	0.06	1
23	7	26.56	0.12	1
24	16	21.30	0.14	1

Table A.1: Personalized signature - CHB-MIT Database

Patient ID	Number of seizures	Recording duration in hours	Seizure duration in hours	Number of patterns
1	11	164.67	0.24	1
2	7	159.44	0.12	1
3	10	161.08	0.50	1
4	6	143.26	0.13	2
5	6	159.67	0.73	2
6	11	159.80	0.25	1
7	6	177.41	0.12	1
8	7	137.98	0.12	2
9	9	93.96	0.12	1
10	18	115.60	0.12	3
11	5	118.11	0.06	x
12	8	135.41	0.13	2
13	10	138.06	0.25	1
14	9	159.73	0.10	1
15	8	158.09	0.20	2
16	6	162.17	0.20	2
17	4	118.73	0.09	2
18	6	92.90	0.09	2
19	9	159.09	0.14	2
20	4	178.21	0.08	2
21	20	161.14	0.40	1
22	4	164.58	0.12	1
23	7	266.37	0.21	x
24	7	159.04	0.16	3
25	9	162.29	0.22	1
26	10	94.45	0.20	2
27	5	167.79	0.17	2
28	6	137.90	0.19	x
29	9	237.52	0.14	2
30	9	159.49	0.24	2

Table A.2: Personalized signature - EPILEPSIA Database

Bibliography

Acharya, U. R., Fujita, H., Sudarshan, V. K., Bhat, S., and Koh, J. E. (2015). Application of entropies for automated diagnosis of epilepsy using eeg signals: A review. *Knowledge-Based Systems*, pages 85–96.

Acharya, U. R., Fujita, H., Sudarshan, V. K., Oh, S. L., Adam, M., Koh, J. E., Tan, J. H., Ghista, D. N., Martis, R. J., Chua, C. K., Poo, C. K., and Tan, R. S. (2016). Automated detection and localization of myocardial infarction using electrocardiogram: a comparative study of different leads. *Knowledge-Based Systems*, pages 146–156.

ADS (2012). Ads1299-4 low-noise, 4-channel, 24-bit analog-to-digital converter for biopotential measurements | ti.com. http://www.ti.com/product/ads1299-4/description.

ADSECG (2011). Ads1191 complete low power integrated analog front end for ecg applications | ti.com. http://www.ti.com/product/ADS1191.

Altman, D. G. and Bland, J. M. (1994). Diagnostic tests. 1: Sensitivity and specificity. *BMJ (Clinical research ed.)*, page 1552.

Ananthanarayanan, G., Bahl, P., Bodik, P., Chintalapudi, K., Philipose, M., Ravindranath, L., and Sinha, S. (2017). Real-time video analytics: The killer app for edge computing. *Computer*, pages 58–67.

Apiletti, D., Baralis, E., Bruno, G., and Cerquitelli, T. (2009). Real-time analysis of physiological data to support medical applications. *IEEE Transactions on Information Technology in Biomedicine*, pages 313–321.

Årzén, K.-E. (1999). A simple event-based pid controller.

Association, A. H. (2017). Cardiovascular disease: a costly burden for america, projections through 2035. https://healthmetrics.heart.org/cardiovascular-disease-a-costly-burden/.

Ball, T., Kern, M., Mutschler, I., Aertsen, A., and Schulze-Bonhage, A. (2009). Signal quality of simultaneously recorded invasive and non-invasive eeg. *NeuroImage*, pages 708–716.

Bandt, C. and Pompe, B. (2002). Permutation entropy: A natural complexity measure for time series. *Physical Review Letters*, page 174102.

Bear, M. F., Connors, B. W., and Paradiso, M. A. (2007). *Neuroscience : exploring the brain.*

Bell, M. A. and Cuevas, K. (2012). Using eeg to study cognitive development: Issues and practices. *Journal of cognition and development : official journal of the Cognitive Development Society*, pages 281–294.

Beniczky, S. and Ryvlin, P. (2018). Standards for testing and clinical validation of seizure detection devices. *Epilepsia*, pages 9–13.

Berger, H. (1931). Über das elektrenkephalogramm des menschen. *Archiv für Psychiatrie und Nervenkrankheiten*, pages 16–60.

Berndt, D. J. and Clifford, J. (1994). Using dynamic time warping to find patterns in time series. *Proceedings of the 3rd International Conference on Knowledge Discovery and Data Mining*, pages 359—370.

Blom, J. and Anneveldt, M. (1982). An electrode cap tested. *Electroencephalography and Clinical Neurophysiology*, pages 591–594.

Blumenfeld, H. (2012). Impaired consciousness in epilepsy. *The Lancet. Neurology*, pages 814–26.

Bozzola, P., Bortolan, G., Combi, C., Pinciroli, F., and BroHet, C. (1996). A hybrid neuro-fuzzy system for ecg classification of myocardial infarction. In *Computers in Cardiology 1996*, pages 241–244. IEEE.

Brandes, A., Smit, M. D., Nguyen, B. O., Rienstra, M., and Gelder, I. C. V. (2018). Risk factor management in atrial fibrillation. *Arrhythmia & Electrophysiology Review*, pages 118–127.

Braojos, R., Beretta, I., Ansaloni, G., and Atienza, D. (2014). Early classification of pathological heartbeats on wireless body sensor nodes. *Sensors*, pages 22532–22551.

Buzsáki, G., Anastassiou, C. A., and Koch, C. (2012). The origin of extracellular fields and currents–eeg, ecog, lfp and spikes. *Nature reviews. Neuroscience*, pages 407–20.

Camm, A. J., Luscher, T. F. T. F., Serruys, P. W., and European Society of Cardiology. (2009). *The ESC textbook of cardiovascular medicine.* Oxford University Press.

Cannon, C. P., Gibson, C. M., Lambrew, C. T., Shoultz, D. A., Levy, D., French, W. J., Gore, J. M., Weaver, W. D., Rogers, W. J., and Tiefenbrunn, A. J. (2000). Relationship of symptom-onset-to-balloon time and door-to-balloon time with mortality in patients undergoing angioplasty for acute myocardial infarction. *JAMA*, page 2941.

Cascino, G. D. (2002). Video-eeg monitoring in adults. *Epilepsia*, pages 80–93.

Chiu, B., Keogh, E., and Lonardi, S. (2003). Probabilistic discovery of time series motifs. pages 493—498. ACM Press.

Clifford, G., Liu, C., Moody, B., Lehman, L.-w., Silva, I., Li, Q., Johnson, A., and Mark, R. (2017). Af classification from a short single lead ecg recording: the physionet computing in cardiology challenge 2017. *IEEE Computing in Cardiology*, pages 1–4.

Coenen, A. and Zayachkivska, O. (2013). Adolf beck: A pioneer in electroencephalography in between richard caton and hans berger. *Advances in cognitive psychology*, pages 216–21.

Cornaggia, C. M., Beghi, M., Moltrasio, L., Beghi, E., and RESt-1 Group (2006). Accidents at work among people with epilepsy. results of a european prospective cohort study. *Seizure*, pages 313–9.

Cossu, M., Cardinale, F., Castana, L., Citterio, A., Francione, S., Tassi, L., Benabid, A. L., and Lo Russo, G. (2005). Stereoelectroencephalography in the presurgical evaluation of focal epilepsy: A retrospective analysis of 215 procedures. *Neurosurgery*, pages 706–718.

de Boer, H. M., Mula, M., and Sander, J. W. (2008). The global burden and stigma of epilepsy. *Epilepsy & behavior : E&B*, pages 540–6.

de Chazal, P., Heneghan, C., Sheridan, E., Reilly, R., Nolan, P., and O'Malley, M. (2003). Automated processing of the single-lead electrocardiogram for the detection of obstructive sleep apnoea. *IEEE Transactions on Biomedical Engineering*, pages 686–696.

Díaz-Uriarte, R. and Alvarez de Andrés, S. (2006). Gene selection and classification of microarray data using random forest. *BMC Bioinformatics*, page 3.

Dietterich, T. G. and Bakiri, G. (1994). Solving multiclass learning problems via error-correcting output codes. *Journal of Artificial Intelligence Research*, pages 263–286.

EMPATICA (2020). Empatica | medical devices, ai and algorithms for remote patient monitoring. https://www.empatica.com/.

EPILEPSY (2015). A closer look at eeg | epilepsy society. https://www.epilepsysociety.org.uk/closer-look-eeg.

Escalera, S., Pujol, O., and Radeva, P. (2009). Separability of ternary codes for sparse designs of error-correcting output codes. *Pattern Recognition Letters*, pages 285–297.

Fan Zhang, Holleman, J., and Otis, B. P. (2012). Design of ultra-low power biopotential amplifiers for biosignal acquisition applications. *IEEE Transactions on Biomedical Circuits and Systems*, pages 344–355.

Fleming, P. J. and Wallace, J. J. (1986). How not to lie with statistics: the correct way to summarize benchmark results. *Communications of the ACM*, pages 218–221.

Fong, J. S., Alexopoulos, A. V., Bingaman, W. E., Gonzalez-Martinez, J., and Prayson, R. A. (2012). Pathologic findings associated with invasive eeg monitoring for medically intractable epilepsy. *American Journal of Clinical Pathology*, pages 506–510.

Fürbass, F., Kampusch, S., Kaniusas, E., Koren, J., Pirker, S., Hopfengärtner, R., Stefan, H., Kluge, T., and Baumgartner, C. (2017). Automatic multimodal detection for long-term seizure documentation in epilepsy. *Clinical Neurophysiology*, pages 1466–1472.

Fürbass, F., Ossenblok, P., Hartmann, M., Perko, H., Skupch, A., Lindinger, G., Elezi, L., Pataraia, E., Colon, A., Baumgartner, C., and Kluge, T. (2015). Prospective multicenter study of an automatic online seizure detection system for epilepsy monitoring units. *Clinical Neurophysiology*, pages 1124–1131.

Gayathri, S., Suchetha, M., and Latha, V. (2012). Ecg arrhythmia detection and classification using relevance vector machine. *Procedia Engineering*, pages 1333–1339.

GeckoBoard (2017). Efm32 leopard gecko | silicon labs. https://www.silabs.com/products/mcu/32-bit/efm32-leopard-gecko.

Goldberger, A. L., Amaral, L. A., Glass, L., Hausdorff, J. M., Ivanov, P. C., Mark, R. G., Mietus, J. E., Moody, G. B., Peng, C. K., and Stanley, H. E. (2000). Physiobank, physiotoolkit, and physionet: components of a new research resource for complex physiologic signals. *Circulation*, pages 215–20.

Goldberger, A. L., Goldberger, Z. D., and Shvilkin, A. (2013). *Goldberger's clinical electrocardiography : a simplified approach*. Elsevier/Saunders.

Gómez, C., Mediavilla, A., Hornero, R., Abásolo, D., Fernández, A., Hovilehto, S., and Al., E. (2009). Use of the higuchi's fractal dimension for the analysis of meg recordings from alzheimer's disease patients. *Medical engineering & physics*, pages 306–13.

Greenlund, K. J., Denny, C. H., Mokdad, A. H., Watkins, N., Croft, J. B., and Mensah, G. A. (2005). Using behavioral risk factor surveillance data for heart disease and stroke prevention programs. *American Journal of Preventive Medicine*, pages 81–87.

Groiss, S. J., Wojtecki, L., Südmeyer, M., and Schnitzler, A. (2009). Deep brain stimulation in parkinson's disease. *Therapeutic advances in neurological disorders*, pages 20–8.

Haas, L. F. (2003). Hans berger (1873-1941), richard caton (1842-1926), and electroencephalography. *Journal of neurology, neurosurgery, and psychiatry*, page 9.

HeartFacts (2019). Heart disease facts & statistics. https://www.cdc.gov/heartdisease/facts.htm.

Herculano-Houzel, S. (2009). The human brain in numbers: a linearly scaled-up primate brain. *Frontiers in human neuroscience*, page 31.

Hirtz, D., Thurman, D. J., Gwinn-Hardy, K., Mohamed, M., Chaudhuri, A. R., and Zalutsky, R. (2007). How common are the "common" neurologic disorders? *Neurology*, pages 326–337.

Hopfengärtner, R., Kasper, B. S., Graf, W., Gollwitzer, S., Kreiselmeyer, G., Stefan, H., and Hamer, H. (2014). Automatic seizure detection in long-term scalp eeg using an adaptive thresholding technique: A validation study for clinical routine. *Clinical Neurophysiology*, pages 1346–1352.

Hoppe, C., Feldmann, M., Blachut, B., Surges, R., Elger, C. E., and Helmstaedter, C. (2015). Novel techniques for automated seizure registration: Patients' wants and needs. *Epilepsy & Behavior*, pages 1–7.

Ihle, M., Feldwisch-Drentrup, H., Teixeira, C. A., Witon, A., Schelter, B., Timmer, J., and Schulze-Bonhage, A. (2012). Epilepsiae – a european epilepsy database. *Computer Methods and Programs in Biomedicine*, pages 127–138.

INYU (2013). Inyu - the inner you - home. http://www.smartcardia.com.

Ivanitsky, A. M., Ivanitsky, G. A., Nikolaev, A. R., and Sysoeva, O. V. (2009). Electroencephalography. Springer Berlin Heidelberg.

Jasper, H. (1958). The ten-twenty electrode system of the international federation. electroencephalography and clinical neurophysiology. pages 371–375.

Jefferys, J. G. (1995). Nonsynaptic modulation of neuronal activity in the brain: electric currents and extracellular ions. *Physiological reviews*, pages 689–723.

Jiruska, P., de Curtis, M., Jefferys, J., Schevon, C., Schiff, S., and Schindler, K. (2013). Synchronization and desynchronization in epilepsy: controversies and hypotheses. *The Journal of physiology*, pages 787–97.

Jurcak, V., Tsuzuki, D., and Dan, I. (2007). 10/20, 10/10, and 10/5 systems revisited: Their validity as relative head-surface-based positioning systems. *NeuroImage*, pages 1600–1611.

Keogh, E. and Ratanamahatana, C. A. (2005). Exact indexing of dynamic time warping. *Knowledge and Information Systems*, pages 358–386.

Khavjou, O., Phelps, D., and Leib, A. (2016). Projections of cardiovascular disease prevalence and costs: 2015–2035. page 32. https://healthmetrics.heart.org/projections-of-cardiovascular-disease/.

Kirchhof, P., Benussi, S., Kotecha, D., Ahlsson, A., Atar, D., Casadei, B., Castella, M., Diener, H.-C., Heidbuchel, H., Hendriks, J., Hindricks, G., Manolis, A. S., Oldgren, J., Popescu, B. A., Schotten, U., Van Putte, B., Vardas, P., Agewall, S., Camm, J., Baron Esquivias, G., Budts, W., Carerj, S., Casselman, F., Coca, A., De Caterina, R., Deftereos, S., Dobrev, D., Ferro, J. M., Filippatos, G., Fitzsimons, D., Gorenek, B., Guenoun, M., Hohnloser, S. H., Kolh, P., Lip, G. Y. H., Manolis, A., McMurray, J., Ponikowski, P., Rosenhek, R., Ruschitzka, F., Savelieva, I., Sharma, S., Suwalski, P., Tamargo, J. L., Taylor, C. J., Van Gelder, I. C., Voors, A. A., Windecker, S., Zamorano, J. L., and Zeppenfeld, K. (2016). 2016 esc guidelines for the management of atrial fibrillation developed in collaboration with eacts. *European Heart Journal*, pages 2893–2962.

Klas, G. (2017). Edge Computing and the Role of Cellular Networks. *Computer*, pages 40–49.

Kwan, P. and Brodie, M. J. (2010). Definition of refractory epilepsy: defining the indefinable? *The Lancet. Neurology*, pages 27–9.

Ladavich, S. and Ghoraani, B. (2015). Rate-independent detection of atrial fibrillation by statistical modeling of atrial activity. *Biomedical Signal Processing and Control*, pages 274–281.

Liaw, A. and Wiener, M. (2002). Classification and regression by randomforest. *R News*, pages 18–22.

Mamaghanian, H., Khaled, N., Atienza, D., and Vandergheynst, P. (2011). Compressed sensing for real-time energy-efficient ecg compression on wireless body sensor nodes. *IEEE Transactions on Biomedical Engineering*, pages 2456–2466.

MPU (2013). Mpu-6000, motion sensor - 6 axis, tdk invensense. https://www.digikey.com/en/product-highlight/i/invensense/mpu6000-6axis-integrated-spi-solution.

Mueen, A., Keogh, E., Zhu, Q., Cash, S., and Westover, B. (2009). Exact discovery of time series motifs. In *Proceedings of the 2009 SIAM International Conference on Data Mining*, pages 473–484.

Murali, S., Rincon, F., and Atienza, D. (2015). A wearable device for physical and emotional health monitoring. In *2015 Computing in Cardiology Conference (CinC)*, pages 121–124. IEEE.

Nguyen, R. and Zenteno, J. F. T. (2009). Injuries in epilepsy: a review of its prevalence, risk factors, type of injuries and prevention. *Neurology International*, pages 466–479.

NRF (2015). nrf8001 / bluetooth low energy / products / home - ultra low power wireless solutions from nordic semiconductor. https://www.nordicsemi.com/eng/Products/Bluetooth-low-energy/nRF8001.

Ocak, H. (2009). Automatic detection of epileptic seizures in eeg using discrete wavelet transform and approximate entropy. *Expert Systems with Applications*, 36:2027–2036.

Pal, M. (2005). Random forest classifier for remote sensing classification. *International Journal of Remote Sensing*, pages 217–222.

Pan, J. and Tompkins, W. J. (1985). A real-time qrs detection algorithm. *IEEE transactions on bio-medical engineering*, pages 230–6.

Pascual, D., Aminifar, A., and Atienza, D. (2019). A self-learning methodology for epileptic seizure detection with minimally-supervised edge labeling. In *2019 Design, Automation & Test in Europe Conference & Exhibition (DATE)*, pages 764–769. IEEE.

Patel, P., Keogh, E., Lin, J., and Lonardi, S. (2002). Mining motifs in massive time series databases. In *2002 IEEE International Conference on Data Mining, 2002. Proceedings.*, pages 370–377. IEEE Comput. Soc.

Patel, S., Lorincz, K., Hughes, R., Huggins, N., Growdon, J., Standaert, D., Akay, M., Dy, J., Welsh, M., and Bonato, P. (2009). Monitoring motor fluctuations in patients with parkinson's disease using wearable sensors. *IEEE Transactions on Information Technology in Biomedicine*, pages 864–873.

Patricia O. Shafer, RN, M. (2014). About Epilepsy: The Basics | Epilepsy Foundation. pages 4–5.

Reddy, M., Edenbrandt, L., Svensson, J., Haisty, W., and Pahlm, O. (1992). Neural network versus electrocardiographer and conventional computer criteria in diagnosing anterior infarct from the ecg. In *Proceedings Computers in Cardiology*, pages 667–670. IEEE Comput. Soc. Press.

Reed, G. W., Rossi, J. E., and Cannon, C. P. (2017). Acute myocardial infarction. *The Lancet*, 389:197–210.

Riazul Islam, S. M., Daehan Kwak, Humaun Kabir, M., Hossain, M., and Kyung-Sup Kwak (2015). The internet of things for health care: A comprehensive survey. *IEEE Access*, pages 678–708.

Rincon, F., Grassi, P. R., Khaled, N., Atienza, D., and Sciuto, D. (2012). Automated real-time atrial fibrillation detection on a wearable wireless sensor platform. In *2012 Annual International Conference of the IEEE Engineering in Medicine and Biology Society*, pages 2472–2475. IEEE.

Rincón, F., Recas, J., Khaled, N., and Atienza, D. (2011). Development and evaluation of multilead wavelet-based ecg delineation algorithms for embedded wireless sensor nodes. *IEEE Transactions on Information Technology in Biomedicine*, pages 854–863.

Ródenas, J., García, M., Alcaraz, R., and Rieta, J. (2015). Wavelet entropy automatically detects episodes of atrial fibrillation from single-lead electrocardiograms. *Entropy*, pages 6179–6199.

Roffo, G., Melzi, S., Castellani, U., and Vinciarelli, A. (2017). Infinite latent feature selection: A probabilistic latent graph-based ranking approach. *In: Proceedings of the IEEE conference on computer vision and pattern recognition*, page 1398–1406.

Ryvlin, P., Tomson, T., and Montavont, A. (2009). Excess mortality and sudden unexpected death in epilepsy. *Presse medicale (Paris, France : 1983)*, pages 905–10.

Santiuste, M., Nowak, R., Russi, A., Tarancon, T., Oliver, B., Ayats, E., Scheler, G., and Graetz, G. (2008). Simultaneous magnetoencephalography and intracranial eeg registration: Technical and clinical aspects. *Journal of Clinical Neurophysiology*, pages 331–339.

Sejnowski, T. J., Churchland, P. S., and Movshon, J. A. (2014). Putting big data to good use in neuroscience. *Nature neuroscience*, pages 1440–1.

Sharma, A. (2015). Epileptic seizure prediction using power analysis in beta band of eeg signals. pages 117–121. IEEE.

Sharma, A., Rai, J. K., and Tewari, R. P. (2019). Identification of various neurological disorders using eeg signals. pages 95–103. Springer, Singapore.

Shoeb, A. H. (2009). Application of machine learning to epileptic seizure onset detection and treatment.

Sipser, M. (2006). *Introduction to the Theory of Computation, Second Edition.*

Sokolski, M., Rydlewska, A., Krakowiak, B., Biegus, J., Zymlinski, R., Banasiak, W., Jankowska, E. A., and Ponikowski, P. (2011). Comparison of invasive and non-invasive measurements of haemodynamic parameters in patients with advanced heart failure. *Journal of cardiovascular medicine (Hagerstown, Md.)*, pages 773–778.

STM32 (2013). Stm32l1 series - stmicroelectronics. http://www.st.com/web/en/catalog/mmc/FM141/SC1169/SS1295?sc=stm32l1.

Stouffer, G. A. (2009). *Practical ECG Interpretation : Clues to Heart Disease in Young Adults*. Wiley-Blackwell.

Sun, Y., Chan, K. L., and Krishnan, S. M. (2002). Ecg signal conditioning by morphological filtering. *Computers in Biology and Medicine*, pages 465–479.

Surrel, G. C. J. (2019). Low power sensing and processing in wearable biomedical devices for personalized health monitoring.

Szucs, A., Lalit, N., Rásonyi, G., Barcs, G., Bóné, B., Halász, P., and Janszky, J. (2006). Sudden death and mortality in epilepsy. *Ideggyogyaszati szemle*, pages 321–8.

Tang, J., Sun, D., Liu, S., and Gaudiot, J.-L. (2017). Enabling deep learning on iot devices. *Computer*, pages 92–96.

Tanriverdi, T., Ajlan, A., Poulin, N., and Olivier, A. (2009). Morbidity in epilepsy surgery: an experience based on 2449 epilepsy surgery procedures from a single institution. *Journal of Neurosurgery*, pages 1111–1123.

Teijeiro, T., García, C. A., Castro, D., and Félix, P. (2018). Abductive reasoning as the basis to reproduce expert criteria in ecg atrial fibrillation identification. *Physiological Measurement*.

Téllez-Zenteno, J. F., Ronquillo, L. H., and Wiebe, S. (2005). Sudden unexpected death in epilepsy: Evidence-based analysis of incidence and risk factors. *Epilepsy Research*, pages 101–115.

Thygesen, K., Alpert, J. S., Jaffe, A. S., Simoons, M. L., Chaitman, B. R., and White, H. D. (2012). Third universal definition of myocardial infarction. *Circulation*.

Webber, W., Lesser, R. P., Richardson, R. T., and Wilson, K. (1996). An approach to seizure detection using an artificial neural network (ann). *Electroencephalography and Clinical Neurophysiology*, pages 250–272.

Wellmer, J., von der Groeben, F., Klarmann, U., Weber, C., Elger, C. E., Urbach, H., Clusmann, H., and von Lehe, M. (2012). Risks and benefits of invasive epilepsy surgery workup with implanted subdural and depth electrodes. *Epilepsia*, pages 1322–1332.

WHO (2013). Who | prevention of recurrences of myocardial infarction and stroke study. *WHO*. http://www.who.int/cardiovascular{_}diseases/priorities/secondary{_}prevention/country/en/index1.html.

WHO (2015). Neurological disorders public health challenges. https://www.who.int/mental_health/publications/neurological_disorders_ph_challenges/en/.

WHO (2016). Neurological disorders. https://www.who.int/news-room/q-a-detail/what-are-neurological-disorders.

WHO (2020). Cardiovascular diseases. https://www.who.int/health-topics/cardiovascular-diseases/.

Wong, C. H., Birkett, J., Byth, K., Dexter, M., Somerville, E., Gill, D., Chaseling, R., Fearnside, M., and Bleasel, A. (2009). Risk factors for complications during intracranial electrode recording in presurgical evaluation of drug resistant partial epilepsy. *Acta Neurochirurgica*, pages 37–50.

Xinnian Chen, X., Solomon, I., and Chon, K. (2005). Comparison of the use of approximate entropy and sample entropy: Applications to neural respiratory signal. In *2005 IEEE Engineering in Medicine and Biology 27th Annual Conference*, pages 4212–4215.

Xu, Y., Nguyen, D., Mohamed, A., Carcel, C., Li, Q., Kutlubaev, M. A., Anderson, C. S., and Hackett, M. L. (2016). Frequency of a false positive diagnosis of epilepsy: A systematic review of observational studies. *Seizure*, pages 167–174.

Zanetti, R., Aminifar, A., and Atienza, D. (2020). Robust epileptic seizure detection on wearable systems with reduced false-alarm rate. In *2020 42nd Annual International Conference of the IEEE Engineering in Medicine & Biology Society (EMBC)*, pages 4248–4251. IEEE.

Zhou, X., Ding, H., Ung, B., Pickwell-MacPherson, E., and Zhang, Y. (2014). Automatic online detection of atrial fibrillation based on symbolic dynamics and shannon entropy. *Biomedical engineering online*, page 18.

İnce, R., Adanır, S. S., and Sevmez, F. (2020). The inventor of electroencephalography (eeg): Hans berger (1873–1941). *Child's Nervous System*, pages 1–2.

DIONISIJE SOPIC

Chemin Vermont 18 ◇ 1006 Lausanne, Switzerland
+41 78 9239283 ◇ `dionisije.sopic@epfl.ch`

EDUCATION

École Polytechnique Fédérale de Lausanne (EPFL) 2015–2020 (ex.)
Ph. D. in Electrical and Electronics Engineering, Department of Information Technologies
École Polytechnique Fédérale de Lausanne (EPFL) 2013–2015
M. Sc. in Electrical and Electronics Engineering, Department of Information Technologies
School of Electrical Engineering, University of Belgrade 2010–2013
B. Sc. in Electrical Engineering, Department of Signals and Systems

HONORS

• EPFL Excellence Fellowship	2013–2015
• Award for the best students of the School of Electrical Engineering, University of Belgrade	2010–2013
• Scholarship of the Republic of Serbia for exceptionally gifted students	2012–2013
• Scholarship of the City of Belgrade for academic excellence	2011–2012

EXPERIENCE

ABB Corporate Research Center 15.09.2014–15.03.2015
Intern *Baden-Dättwil, Switzerland*

- Porting the real-time operating system Xenomai to the target platform Zedboard
- Streamlining the compilation and deployment process of Xenomai
- Exploring MATLAB/Simulink automatic code-generation support for Zedboard

PUBLICATIONS

- D. Sopic, A. Aminifar, D. Atienza Alonso, Real-Time Event-Driven Classification Technique for Early Detection and Prevention of Myocardial Infarction on Wearable Systems, EEE Transactions on Biomedical Circuits and Systems, 2018
- D. Sopic, A. Aminifar, D. Atienza Alonso, e-Glass: A Wearable System for Real-Time Detection of Epileptic Seizures, The International Symposium on Circuits and Systems (ISCAS), Italy, 2018
- D. Sopic, E. De Giovanni, A. Aminifar, D. Atienza Alonso, Hierarchical Cardiac-Rhythm Classification Based on Electrocardiogram Morphology, Computing in Cardiology (CinC), France, 2017
- D. Sopic, A. Aminifar, A. Aminifar, D. Atienza Alonso, Real-Time Classification Technique for Early Detection and Prevention of Myocardial Infarction on Wearable Devices, 13th IEEE Biomedical Circuits and Systems Conference (BioCAS), Italy, 2017
- D. Sopic, S. Murali, F. J. Rincon Vallejos, D. Atienza Alonso, Touch-Based System for Beat-to-Beat Impedance Cardiogram Acquisition and Hemodynamic Parameters Estimation, IEEE/ACM Design Automation and Test in Europe Conference (DATE), Germany, 2016
- E. Kroupi, D. Sopic, T. Ebrahimi, Non-linear EEG features for odor pleasantness recognition, Sixth International Workshop on Quality of Multimedia Experience (QoMEX), Singapore, 2014

PATENTS

- D. Sopic, R. Zanetti, A. Aminifar, D. Atienza Alonso, A wearable system for real-time detection of epileptic seizures, Patent numbers: WO2019162850 (A1), P3264US00

PROJECTS

- Chewbacca project: Algorithms for quantifying chewing behaviour in pets
- Body composition measurement using a wearable bio-signal monitoring system — M. Sc. Thesis
- Non-linear EEG features for odor pleasantness recognition — Semester Project
- Co-adaptive MI BCI training
- An approach to speaker identification - Identification based on LPC-derived features — B. Sc. Thesis
- Control of the three-phase asynchronous motor in Siemens TIA Portal Environment

TECHNICAL KNOWLEDGE

Programming skills
- MATLAB/Simulink
- C/C++
- Java
- Python
- CSS, JavaScript, PHP
- Ladder Programming for Allen Bradley & Siemens PLCs

Tools
- Xilinx Tools – Vivado Design Suite, Petalinux tools
- Siemens Totally Integrated Automation Portal Environment
- LaTeX

Operating Systems
- Windows, Linux, Xenomai, Android

LANGUAGES

Serbian: Native Speaker

English: Fluent
- Advanced level diploma from Oxford Westminster College
- Advanced level diploma from English Language Centre Bristol

French: Fluent
- Certificat d’assiduité de l’école Azurlingua
- Certificat d’assiduité de l’école de Saint–Denis Ecole de Langues et Lycee International de Touraine

Spanish: Fluent

Italian: Fluent

German: Beginner